Molecular Hydrogen in Galaxy Simulations

Molecular Hydrogen in Galaxy Simulations

By Padraic Odesse, B.Sc

A Thesis Submitted to the School of Graduate Studies in the Partial Fulfillment of the Requirements for the Degree Master of Science

McMaster University

Master of Science   (2023)

Hamilton, Ontario (Physics & Astronomy)

TITLE: Molecular Hydrogen in Galaxy Simulations

AUTHOR: Padraic ODESSE (McMaster University)

SUPERVISOR: Dr. James WADSLEY

NUMBER OF PAGES: xiv, 91

Abstract

Contemporary galaxy simulations are currently capable of resolving the dense molecular phase of the interstellar medium. The behaviour of this molecular gas is complicated by the ability for molecular hydrogen to self-shield, protecting the deeper layers of clouds from dissociating radiation that would otherwise break the molecules into constituent parts and heat the gas. An accurate model of molecular hydrogen needs to couple to the local radiation field of the galaxy while also accounting for the effects of self-shielding. I present a self-consistent chemical network to model the formation and destruction of molecular hydrogen and related primordial gas species (H, He, and their ions). The model is designed to couple to a realistic UV radiation field modeled using discrete bands. It is intended for use in the GASOLINE N-body hydrodynamics code for galaxy simulations alongside the TREVR and TREVR2 ray-tracing radiative transfer routines. When combined with these routines, my model offers a correct treatment for shielding that allows for radiation from multiple sources to be shielded independently. I include several tests to ensure the fidelity of this model, including simulated HII regions, photodissociation regions, and the evolution of primordial gas prior to galaxy formation. This model is applicable in the simulation of a realistic interstellar medium in isolated disk galaxies and the evolution of dwarf galaxies. A proper model for molecular hydrogen with radiation in a galaxy enables simulations to produce observable quantities that can be used to evaluate the quality of our simulated galaxies. This model will provide opportunities to explore the connection between molecular hydrogen and models of star formation.

Acknowledgements

I would first like to thank my supervisor, Dr. James Wadsley, for his incredible patience and mentorship over these past two years. I would also like to thank the members of my thesis committee, Dr. Laura Parker and Dr. Alison Sills for their thorough evaluation of my work and constructive comments on my Thesis. This research was performed while funded by an NSERC CGS-M and an Ontario Graduate Scholarship.

I should also like to thank my highschool computer science teacher, Rodney Reimer for teaching me the value of "If it ain't broke, don't fix it." Failure to follow your advice cost me about two weeks of debugging.

There are a number of people that have contributed to my graduate school experience over these past two years whom I wish to acknowledge. Thank you first to Nicole for your everlasting support, and for always brightening up my day. I would also like to thank the members of my D&D group: Nicole, Kate, Erik, Ozzy, and Nick, for giving me something else to care about, enjoying our hobby, and for valuing my creativity. Thank you as well to Alicia; you proved yourself to be a bastion of support as I made the frankly difficult transition to grad school. Finally, I would like to thank Bobby & Catherine for their advice, support, and for welcoming me back home to Sackville whenever the opportunity arose.

To my family, who always has my back. I would like to thank my mother for her care and kindness, for wrangling my anxiety, and providing sage advice. I would also like to thank my father, who also kept my anxiety in check, and provided me with food. I really could not have done this without you. Thank you as well to Glenn for your inspiration and advice, and to Gran for your everlasting kindness. Finally, thank you to Granddad for reminding me that I'll always have a home. You did not get to see the end of this thesis, but I know you would have been proud.

Contents

List of Figures

List of Tables

Declaration of Authorship

I, Padraic ODESSE, declare that this thesis titled, "Molecular Hydrogen in Galaxy Simulations" and the work presented in it are my own.

Chapter 1

Introduction

"In the beginning, the universe was created. This has made a lot of people very angry and been widely regarded as a bad move."

Douglas Adams

A major focus of astrophysics is to understand galaxies and their inner workings. Most of the information that astronomers have gathered about galaxies is obtained by measuring light. The earliest light we can measure in the universe comes from the point at which baryons and photons decoupled, known as the cosmic microwave background (CMB). Observations of the CMB and related cosmological measurements have tightly constrained the components of the universe itself and the overall context for galaxy formation (Planck Collaboration et al. 2016). Galaxies are comprised of gas, dust, and stars, embedded in a halo of dark matter, and assemble hierarchically from the merging of smaller precursors over cosmic time.

Since galaxies evolve over millions to billions of years, we can only observe snapshots of galaxies in various phases of evolution. We cannot isolate any single galaxy and observe its evolution over cosmic time. However, simulations provide us the tools with which to experiment with the physics of galaxies and examine how changes to these physics affect the evolution of galaxies. Galaxy simulations can encompass a vast range of physical and temporal scales, capturing the distribution of galaxies across the universe, all the way down to clusters of stars within a single galaxy (Bertschinger 1998).

One aspect of galaxy simulations that is currently being improved are models for the interstellar medium (ISM), the gas and dust that permeates galaxies. Gas can cool by radiating away energy as light, which enables gas to form a relatively dense ISM in the centre of each galactic halo. This collapse is typically limited by rotation and thus the ISM takes the form of a rotating disk, particularly in larger galaxies. This disk is

unstable to gravitational fragmentation, so the further cooling of gas enables the ISM to fragment and form molecular clouds. These dense clouds of gas can collapse to form stars. Galaxy simulations today can now reach densities high enough to resolve these dense phases of the ISM (Faucher-Giguère 2018; Jeffreson et al. 2021), so proper models for molecular gas are necessary in order to correctly simulate molecular clouds.

The physics of molecular gas (namely molecular hydrogen, H_2) is complicated by the need for radiative transfer. Radiative transfer refers to the process by which radiation from stars permeates through the ISM and delivers energy to the gas. Past simulations that model molecular gas in the ISM relied on approximations to the radiative transfer method to do so (Christensen et al. 2012; Gnedin and Draine 2014; Nickerson et al. 2018). More recent works that incorporate full radiative transfer methods in their simulations have produced improved models of molecular gas (Baczynski et al. 2015; Kim et al. 2023), and recent improvements to the algorithms which compute radiative transfer enable simulations to efficiently model the effects of stellar radiation on the ISM (Wadsley et al. 2023). Therefore, we need to understand physics and chemistry of molecular gas so that we can develop a model for H_2 that is suitable for simulations of galaxies that use radiative transfer. This will result in an improved model of the interstellar medium of galaxies that is appropriate for use in the higher resolution simulations we perform today.

1.1 The Interstellar Medium

The ISM of galaxies has changed significantly as the universe has evolved. Dust grains are comprised of metals created in stars, which are injected into the ISM via stellar winds. In astronomy, metals are any elements heavier than helium. In the nearby universe and in our own Galaxy, the ISM is considerably enriched with metals, and the thermodynamic state of the ISM is dominated by efficient cooling from metals such as CII and OI balancing photoelectric heating, which is the result of ultraviolet radiation dislodging electrons from dust grains, depositing energy into the gas (Wilson and Rood 1994; Wolfire et al. 1995; Wolfire et al. 2003; Tielens 2005; Klessen and Glover 2016). In the early universe, the ISM of galaxies contained very few metals, so its thermodynamic and chemical state was dominated by the hydrogen cooling, which is less effective than metal cooling at temperatures less than 10^4 K (Tielens 2005). This cooling is balanced against heating from Lyman-Werner radiation, which can be absorbed by molecular hydrogen to heat the gas (Glover 2013; Bovino and Galli 2019; Klessen and Glover 2023).

1.1.1 Phases of the interstellar medium

The ISM is not a uniform medium, but rather is comprised of multiple coexisting phases of gas, characterised by their temperature, density, and ionization state (Klessen and Glover 2016). The hot ionized medium (HIM) has a characteristic temperature of $T \sim 10^6$ K, and a characteristic number density of baryons of $n \sim 10^{-2}$ atoms cm^{-3}. This usually corresponds to gas in the circumgalactic medium (CGM), the diffuse gas that surrounds galaxies while still remaining gravitationally bound within their dark-matter halo (Tumlinson et al. 2017).

The warm ionized medium (WIM) has a temperature around $T \sim 8000$ K, and densities ranging from $n \sim 0.2 - 0.5$ cm^{-3}, and predominantly consists of ionized gas, HII. Similarly, the warm neutral medium (WNM) exists at similar temperatures ranging from $T \sim 6000 - 10^4$ K, and densities ranging from $n \sim 0.2 - 0.5$ cm^{-3}. This gas is neutral, mostly comprised of HI, but still remains warm (Klessen and Glover 2016).

The cold neutral medium (CNM) has temperatures ranging from $T \sim 50 - 100$ K, and densities ranging from $n \sim 20 - 50$ cm^{-3}. The cold neutral medium can condense out of the warm neutral medium via the two-phase instability (see Section 1.1.3) (Ostriker et al. 2010). Finally, the molecular phase of the ISM has temperatures in the range $T \sim 10 - 20$ K, and high densities $n > 10^2$ cm^{-3}. This gas is molecular, comprised primarily of H$_2$ with trace HI present, and is able to form when cold neutral gas is shielded from far-ultraviolet radiation (Hollenbach and Tielens 1999).

1.1.2 Heating and cooling of interstellar gas

When constructing a model of a galaxy, we determine the thermodynamic state of the gas by solving heating and cooling functions, which are constructed based on the temperature, density, and chemical composition of the gas (Black 1987; Sutherland and Dopita 1993; Glover and Abel 2008). Figure 1.1 shows the net cooling function for gas at redshift $z = 3$ (Shen 2010).

Cooling rates are highly dependent on the ionization state of the gas. For instance, the cooling rate of ionized gas at $T < 10^4$ K is 10 to 1000 times larger than that of neutral gas (Gnedin and Hollon 2012). This can mean that a dynamic change in the environment of the gas can strongly affect heating and cooling functions (Robinson et al. 2022). In particular, a change in the incident radiation field which gas is exposed to can strongly affect the cooling rate of that gas.
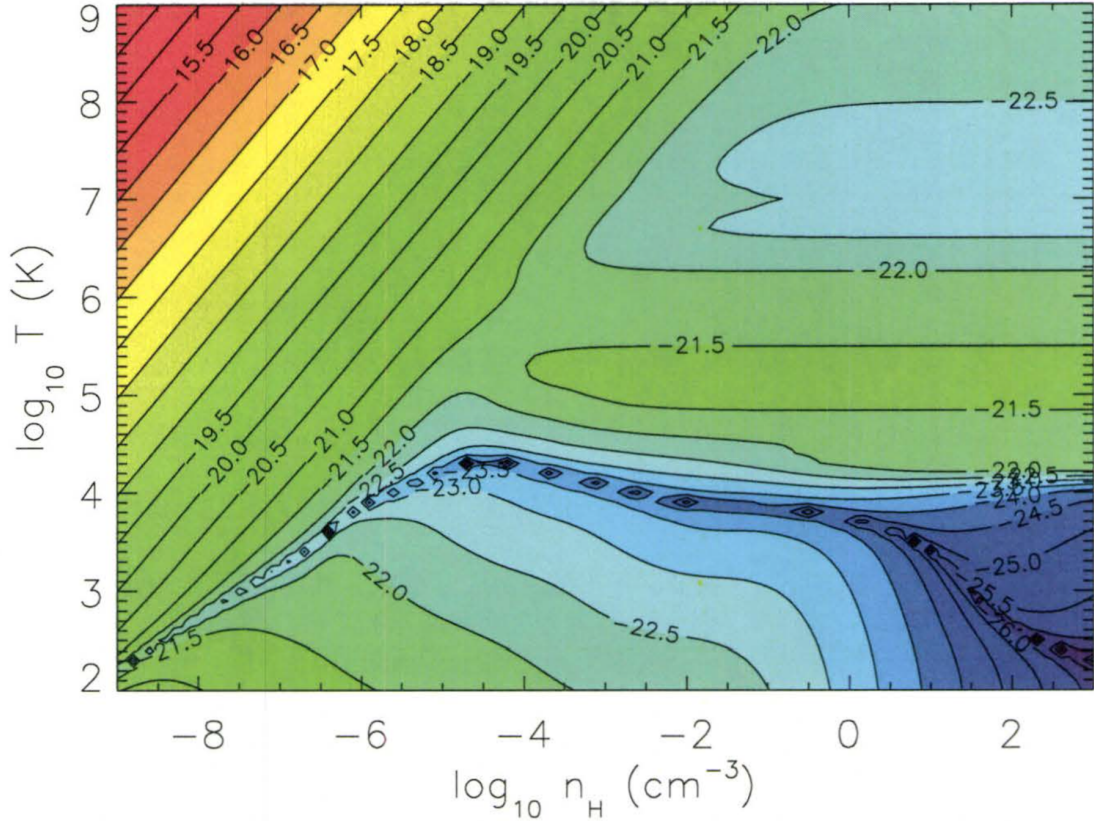
FIGURE 1.1: Figure 3.13 from Shen (2010) shows cooling rates for solar metallicity gas at $z = 3$, exposed to the cosmic UV background, with cooling due to adiabatic expansion. The plot shows normalized net cooling rates $\log(|\Lambda - \Gamma|/n_{\mathrm{H}}^2)$ in erg s^{-1} cm^3 at a grid of densities and temperatures (n, T). The lowest contour in dark blue represents the equilibrium state of the gas, spanning all densities, and temperatures in the range of $10^2 \mathrm{K} < T < 10^4$ K. Regions above this equilibrium curve are cooling, while regions below are heating.

When the gas is in collisional ionization equilibrium (CIE), it is acceptable to parameterize cooling and heating functions using temperature, density, and metallicity (Sutherland and Dopita 1993). Collisional ionization equilibrium is appropriate whenever the gas is optically thin, low density, and in a steady state, in which case the effects of the incident radiation field can be ignored (Bryans et al. 2006). Outside of CIE, cooling and heating functions can depend on any parameter that changes the ionization state of the gas (Robinson et al. 2022). Attempts to approximate changes in the local radiation field based on key ionization rates still lead to errors (Gnedin and Hollon 2012). The correct approach is to model the ionization state of the gas based on the full

4

radiation spectrum. While dedicated spectral modeling codes are capable of capturing this ionization state when constructing models of irradiated interstellar clouds (Le Petit et al. 2006; Ferland et al. 2017), the computational cost of modeling the full ionization state of all elements in the ISM is not always feasible for galaxy models.

1.1.3 The two-phase instability in the ISM
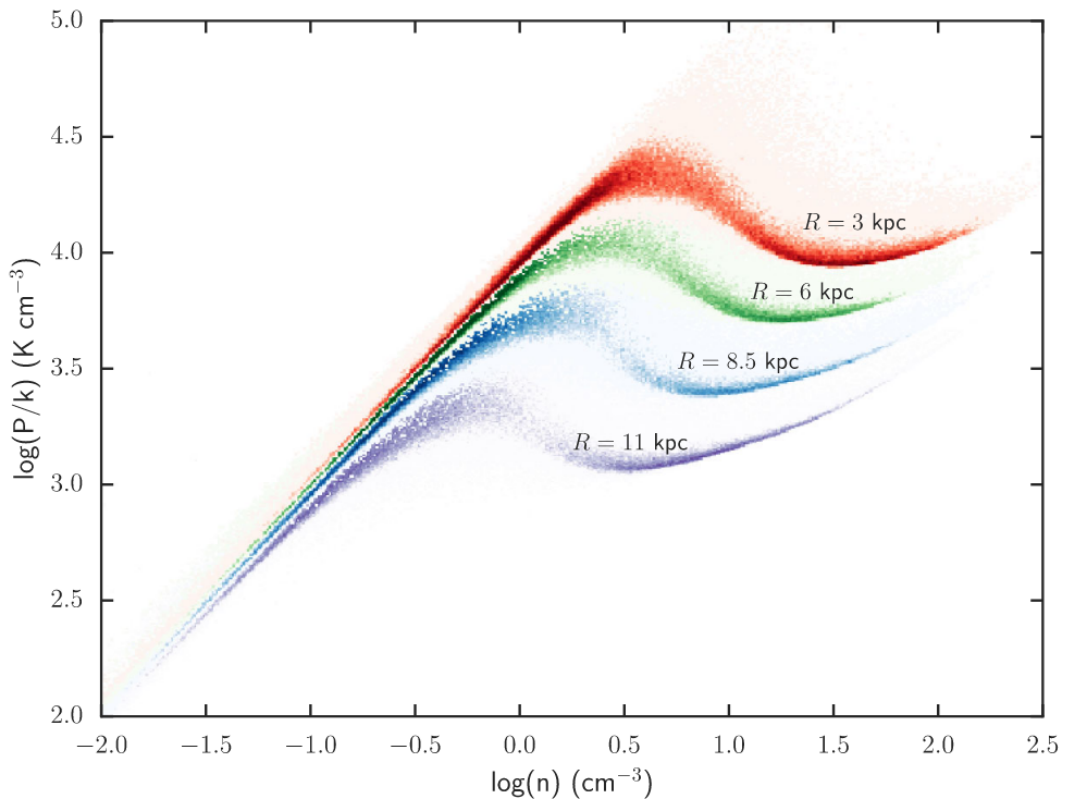
FIGURE 1.2: This reproduction of Figure 1 from Benincasa et al. (2016) compares the pressure-density relation at different radii from their simulated reference galaxy. This shows the two-phase instability of the ISM; at any given radius, there exists a range of pressures for which there are two stable density solutions (where $\frac{dP}{d\rho} > 0$, positive slope). The lower density stable solution corresponds to the warm neutral medium, while the higher density stable solution corresponds to the cold neutral medium. Regions where the slope is negative ($\frac{dP}{d\rho} < 0$) are unstable, so any perturbations to the ISM density will grow, bringing the gas into either the warm or cold phase.

The formation of cold interstellar gas is the rate limiting step for star formation (Benincasa 2014). The amount of cold interstellar gas present in a galaxy is set by the

two-phase instability of the ISM. The phases of the ISM in our own Galaxy are observed to be in a rough pressure equilibrium of $P/k \sim 10^3 - 10^4 \mathrm{K}\ \mathrm{cm}^{-3}$ (Wolfire et al. 1995). This equilibrium is maintained by a balance of photoelectric heating and CII cooling. The shape of an example equilibrium curve for a simulated reference galaxy is shown in Figure 1.2, reproduced from Benincasa et al. (2016). In this figure, if we consider a horizontal line of constant pressure, we can find a range of pressures for which two stable density solutions are possible (where the slope is positive), and one density solution which is unstable (where the slope is negative) (Wolfire et al. 2003). The low-density stable solution is the WNM, and the high-density stable solution is the CNM. Where the slope is negative, $\frac{dP}{d\rho} < 0$, any perturbation in the density $\rho + \delta\rho$ grows. So, any gas that tries to persist between these phases is unstable, and any density perturbation will grow until that gas resides in either stable region. For local galaxy conditions near the Sun, Wolfire et al. (1995) find that photoelectric heating produces a stable two-phase medium for a narrow range of pressures from 990K cm^{-3} < P/k < 3600K cm^{-3}. For pressures that exceed this range, the gas *must* transition to the cold phase (Wolfire et al. 2003). Hence, the ability for cold, dense gas to form in the ISM is proportional to the pressure of the ISM.

The physics of our model can strongly affect how gas transitions from the stable WNM to the CNM, which can then be made unstable to collapse. This instability illustrates that the hot, warm, and cold phases of the ISM are set by hydrodynamics. In order to form a molecular cloud that can collapse into stars, the gas must first reach the CNM by passing through this two-phase instability.

1.1.4   The Kennicutt-Schmidt relation

The Kennicutt-Schmidt (KS) relation is an observed correlation between the surface density of star formation and molecular hydrogen, which suggests that the rate at which a region of a galaxy forms stars is proportional to the surface density of gas in that region (Kennicutt and Evans 2012). Although this was originally found to be a galaxy-wide property (Schmidt 1959), the Kennicutt-Schmidt relation applies on resolved scales as well (Bigiel et al. 2008). This suggests that it is not just the quantity of molecular gas throughout the galaxy that sets the star formation rate, but rather that stars form more readily in regions of molecular gas. The relation itself is given by Equation 2 of Bigiel et al. (2008):

$$\Sigma_{\mathrm{SFR}} \propto (\Sigma_{\mathrm{H_2}})^N \tag{1.1}$$

where the power law relation N can vary depending on the specific galaxy or environment, but has an average value of $N \sim 0.96 \pm 0.07$. There is no single KS relation that can describe every galaxy.

It is important to note that the existence of this correlation does not necessarily imply that molecular gas causes stars to form. The primary trigger for star formation is the density of the gas itself, or equivalently the strength of its self gravity, and does not depend on whether that gas is atomic or molecular (Kennicutt 1989). This suggests that Σ_{H_2} is a better tracer of star formation than Σ_{HI} simply because H_2 traces the coolest and densest gas in the ISM, while HI only traces the neutral gas (which can be warmer, more diffuse, and stable against collapse). We will discuss this point further in Section 1.2.

1.1.5 Regulating star formation: feedback mechanisms

Feedback, with regards to star formation, refers to any process by which stars inject energy back into the ISM, enabling a galaxy to self-regulate its ability to form stars. The paper by Ostriker et al. (2010) provides an excellent overview of feedback, which we summarize very briefly here. In order for a galaxy to maintain vertical dynamical equilibrium, the pressure of the ISM needs to balance the weight of the galaxy disk. As we saw in Section 1.1.3, the ability for cold, dense gas to form in the ISM is proportional to the pressure of the ISM. Additionally, the thermal pressure of the ISM is approximately proportional to the photoelectric heating rate, and by extension the star formation surface density Σ_{SFR}, as young stars contribute the far-ultraviolet radiation that drives photoelectric heating (Ostriker et al. 2010). So, an increased Σ_{SFR} leads to an increase in the thermal pressure of the ISM, which more strongly counteracts the weight of the galaxy. This reduces the amount of dense gas that forms, thereby reducing star formation Σ_{SFR}, and creating a negative feedback loop that enables the galaxy to regulate the rate at which it forms stars. Simulations of galaxies further support this theory (Benincasa et al. 2016; Ostriker and Kim 2022).

This picture of stellar feedback focuses on the contribution from stellar radiation to the self-regulation of galaxies. There are other sources of galactic feedback, such as active galactic nuclei (Di Matteo et al. 2005), and stars can return energy to the ISM through a number of different feedback processes, such as winds (Krumholz et al. 2012) or supernovae (Larson 1974), however the dominant energy output over the lifetime of a star cluster is through radiation. This is shown in Figure 1.3 reproduced from Grond et al. (2019), which illustrates the rate of energy output by a population of stars in the form
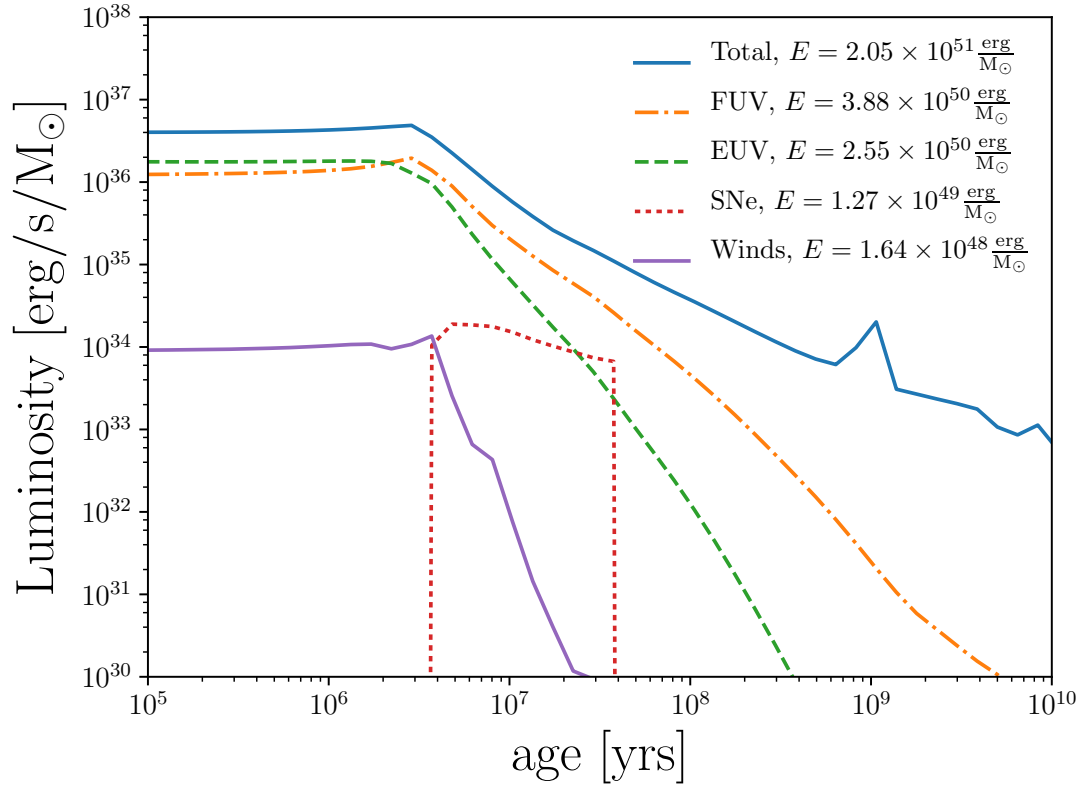
FIGURE 1.3: Reproduction of Figure 1 from Grond et al. (2019). This plot shows the energy output through radiation (FUV and EUV), supernova events (SNe), and winds, from a stellar population with a Chabrier initial mass function (Chabrier 2003) as the population ages. The energy budget is dominated by far-ultraviolet (FUV) radiation throughout the entire lifetime of the population. Capturing radiative feedback is paramount to understanding the energy output by star clusters.

of stellar winds, supernova feedback (SNe) and radiation (FUV and EUV) as a function of the cluster's age. Far-ultraviolet radiation (FUV) is not energetic enough to ionize hydrogen, but contributes significantly to photoelectric heating. Extreme-ultraviolet radiation (EUV) is energetic enough to ionize hydrogen, and can influence the chemical state of the ISM and drive heating by photodissociation.

Stellar radiation alone is not capable of regulating a galaxy (Benincasa et al. 2020). Since radiation can travel long distances, this energy can be deposited far away from regions of star formation. It is therefore important that we understand how radiation couples to the gas. Previous galaxy simulations have found that modeling radiative transfer from local stellar sources improves the Kennicutt-Schmidt relation derived from

simulated galaxies (Benincasa et al. 2020), which suggests that modeling radiative feedback is critical to creating a complete model of a galaxy. These simulations, however, did not include a model for molecular hydrogen, so their Kennicutt-Schmidt relation was computed based only on the dense gas. In order to complete this treatment of radiative transfer, it is necessary to develop a model for the formation of molecular hydrogen.

1.2 Molecular Hydrogen in Galaxies

Molecular hydrogen tends to be found in regions of galaxies with surface densities greater than 10 $M_\odot$ pc^{-2} (Ostriker et al. 2010). Dwarf galaxies have relatively low surface densities ($\Sigma_{\text{gas}} < 10$ $M_\odot$ pc^{-2}) and are predominantly comprised of atomic gas, while starbursting galaxies frequently have high surface densities ($\Sigma_{\text{gas}} \gg 10$ $M_\odot$ pc^{-2}) and large H_2 fractions (Bigiel et al. 2008). Between these two extremes, Milky Way-like galaxies have regions of surface densities both above and below 10 $M_\odot$ pc^{-2}, which correspond to regions of molecular and atomic gas respectively. Molecular gas in Milky Way-like galaxies is typically found in Giant Molecular Clouds (GMCs). These are simply regions of the ISM characterized by a rapid increase in density and change in chemical state from atomic gas to molecular gas (Kennicutt and Evans 2012). GMCs are defined relative to their surroundings, and therefore cannot be treated as isolated systems (Chevance et al. 2023). Much of the chemistry that sets the fraction of H_2 in a galaxy occurs at the transition regions between the cold ISM and these molecular clouds.

1.2.1 Interaction with radiation: Photodissociation regions

The coupling of radiation to the chemistry of the ISM is primarily observed in Hɪɪ regions and photodissociation regions. An Hɪɪ region is a region of ionized gas surrounding a star, where the chemical state of the gas is dominated by ionizing photons ($h\nu > 13.6$ eV) from the central star (Tielens 2005). The size of this region is set by volume of gas needed for the recombination rate within that volume to balance the rate of ionizing photons produced by the star. Beyond this region, the gas transitions from being ionized to neutral, and the only photons that continue further are non-ionizing far-ultraviolet (FUV) photons ($h\nu < 13.6$ eV). These remaining photons set the chemistry of photodissociation regions.

Photodissociation regions (PDRs) are neutral regions of the ISM where the chemistry thermodynamics are dominated by FUV photons (Hollenbach and Tielens 1999). They behave in a similar manner to Hɪɪ regions, whereby photodissociation from FUV photons
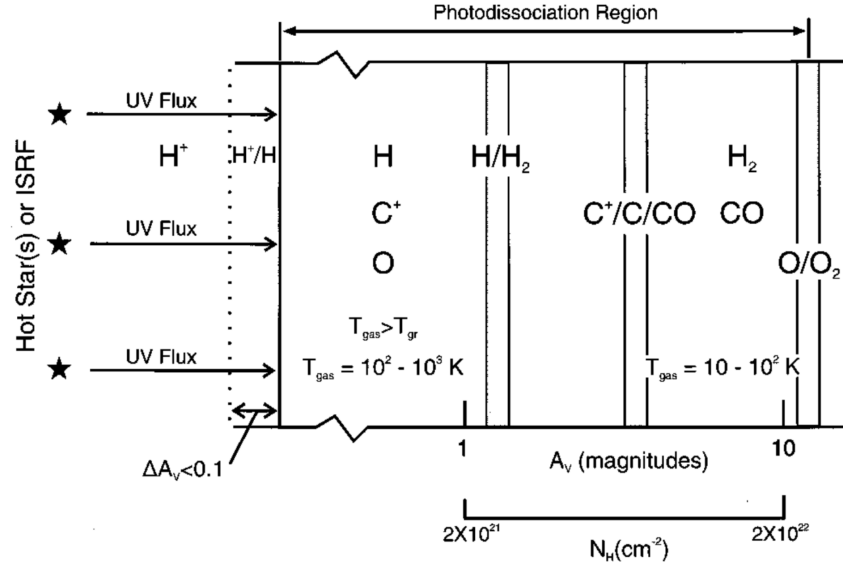
FIGURE 1.4: This reproduction of Figure 3 from Hollenbach and Tielens (1999) illustrates the structure of a photodissociation region (PDR) as a function of depth. The PDR is illuminated from the left by ultraviolet flux, either from the interstellar radiation field, or through an HII region. This first region is predominantly atomic HI, but transitions to being predominantly molecular H_2 around a column density $N_H \sim 10^{21}$ cm^{-2}. Although the cloud past this depth is predominantly molecular, photodissociation of other molecules (CO and O_2) continues to occur.

counters the formation rate of molecules. Figure 1.4 illustrates the structure of a photodissociation region. The chemical state of the neutral ISM is determined by reactions within these PDRs. Since the PDR is predominantly neutral, significant quantities of molecular hydrogen (H_2) can begin to form.

H_2 is capable of self-shielding against far-ultraviolet radiation in the Lyman-Werner band (11.2 eV to 13.6 eV) (Stecher and Williams 1967; Draine and Bertoldi 1996). This is a process by which the outer layers of H_2 in a cloud are capable of quickly removing the Lyman-Werner photons that are most capable of destroying H_2. The mechanisms behind shielding are explained in more detail in Section 2.3. The H_2 molecules in the PDR can absorb Lyman-Werner photons of specific energies which correspond to energy level transitions between excited states, and above a column density of $N_{H_2} > 10^{14}$ cm^{-2}, the FUV absorption lines in the Lyman-Werner band become optically thick, and molecular hydrogen begins to self-shield (Hollenbach and Tielens 1999). Beyond this depth, the cloud is capable of becoming fully molecular. Modeling the photochemistry of PDRs is necessary for constraining the fraction of H_2 in a galaxy.

1.2.2 Molecular hydrogen and star formation

The correlation between H_2 and star formation arises because the temperature at which atomic gas converts to molecular gas is similar to the temperature at which a cloud destabilizes and begins to collapse (Krumholz et al. 2011). The reason that we see stars form in region of molecular gas is that molecular gas and star formation are correlated with a third factor; the ability of a cloud to shield itself from the interstellar radiation field (ISRF) of a galaxy (Glover and Clark 2012). The ISRF is primarily composed of far-ultraviolet and Lyman-Werner photons, since the more energetic ionizing photons are absorbed in the HII regions that surround young star clusters (Habing 1968; Draine 1978).

In the simulations performed by Glover and Clark (2012), dust shielding has a stronger effect on the rate of star formation in clouds than H_2 self-shielding, as dust shielding reduces the amount of FUV radiation that can heat the gas via the photoelectric effect (Glover and Clark 2012). Therefore, if we want to understand the behaviour of star formation in nearby spiral galaxies, our primary concern should be the proper implementation of photoelectric heating. If, however, we want to understand star formation throughout the entire universe, we need to implement H_2 physics as well. In the context of isolated galaxy simulations, H_2 is an improvement to the chemical network, and enables us to better study the regions in which stars form, but should not strongly affect the overall gas dynamics. Much of this thesis will focus on calibrating our models of molecular hydrogen, but our overarching goal is to obtain a full understanding of all the radiative processes that set the state of the ISM.

Glover (2023) summarizes the results of several simulations performed over the past decade that test the contribution of H_2 to star formation in low metallicity environments. They find that at the onset of star formation, clouds with low metallicities $Z \sim 0.01 Z_\odot$ can form stars with a H_2 fraction of less than 1%, and conclude that at metallicities $Z \sim 0.1 Z_\odot$ and below, star formation should occur in clouds that are predominantly atomic. Additionally, cooling by molecular hydrogen is not necessary to form such clouds in the first place (Hu et al. 2016; Hu et al. 2017; Hu et al. 2021; Whitworth et al. 2022). Again, these papers only examined metallicities down to $Z \sim 0.01 Z_\odot$, which does not cover the conditions under which the first stars in the universe (Population III stars) formed from primordial gas. Cooling by the CII ion provides a cooling rate roughly 100 times larger than cooling by H_2 at solar compositions (Glover and Clark 2012), so examining the formation of low metallicity gas clouds down to $Z \sim 0.01 Z_\odot$ is not low enough to enter the regime where H_2 would be an important coolant. H_2

may still enable star formation in regions of the universe where the gas composition is similar to the primordial composition, such as in the first galaxies, and in dwarf galaxies. Therefore, a model for the formation and evolution of H_2 in the ISM is necessary in order to further investigate star formation in these regimes.

1.3   Simulations of Galaxies

Most galaxy simulations today will at least solve both gravity and hydrodynamics. Simulating the hydrodynamics of galaxies enables us to track the evolution of gas and the formation of stars. Generally, the physics that govern the evolution of gas are complicated and non-linear. Processes such as gas turbulence are extremely difficult to solve analytically, requiring numerical methods to solve (e.g. supersonic turbulence in the ISM, Federrath 2013), yet may be essential to governing the dynamics of star formation (Federrath and Klessen 2012). This is another key strength of simulations; they enable us to study complex or chaotic physics. We can then experiment with how these complex physics interact to alter the formation and evolution of galaxies.

1.3.1   Tree solvers for gravity
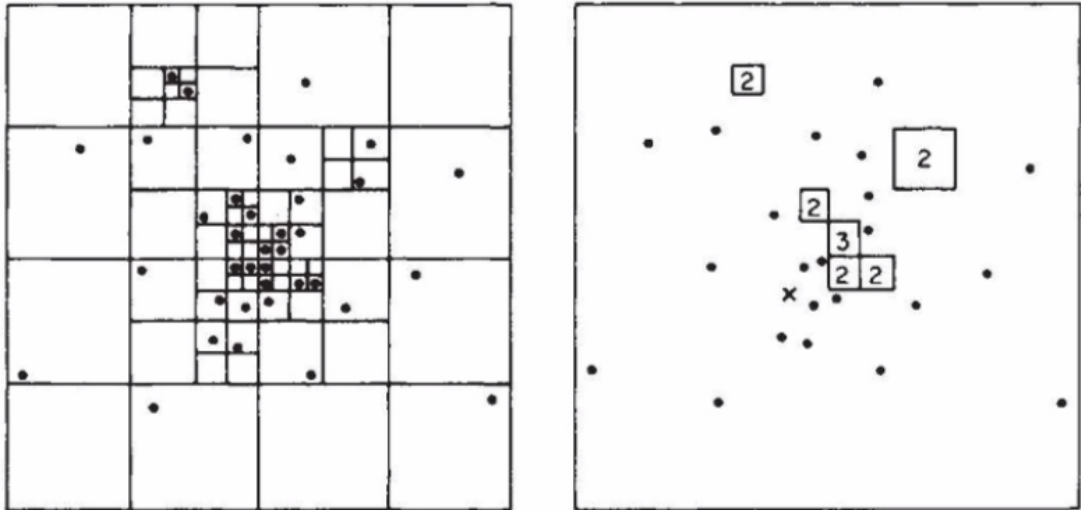
FIGURE 1.5: Figure 1 of Barnes and Hut (1986) illustrates tree hierarchy for gravity. The left panel shows the division of particles in the tree hierarchy. On the right, an example gravity calculation is shown for the particle x. Particles that lie in the tree cells labelled 2 and 3 have their center of masses averaged for the gravity calculation, while remaining contributions are computed on a particle-by-particle basis.

Solving N-body dynamics is a major logistical problem. The N-body problem for gravity scales as $O(N^2)$; if a simulation contains N resolution elements, every element must be compared to every other element in order to solve the contribution of all masses to gravity, so N^2 calculations are required to solve the N-body problem. This would be disastrous for galaxy simulations today, which can have hundreds of millions of resolution elements. Codes will therefore make use of a tree structure to approximate the behaviour of gravity on large scales. The Barnes and Hut (1986) algorithm uses this tree structure to reduce the scaling of the gravity problem to $O(N \log N)$. Figure 1.5 summarizes the behaviour of this algorithm. This tree hierarchy can also be used to reduce the scaling costs of radiative transfer methods as well, which will be discussed briefly in Section 3.2 (Grond et al. 2019; Wadsley et al. 2023).

1.3.2 The sub-grid scale

The physical processes that govern galaxies extend from the stellar scale up to the galactic scale, covering about 10 orders of magnitude. The physics that occur on stellar scales of roughly 1 AU (10^{13} cm) (winds, radiation, supernova, etc.) have a pronounced effect on galaxy evolution at the galactic scale of kiloparsecs (1 kpc $\sim 10^{21}$ cm) (heating of ISM, outflows into the CGM, shocks, etc.). No model has the capacity to capture all these scales spanning over 8 orders of magnitude. Therefore, simulations will always need some treatment for physics below the resolution scale (Naab and Ostriker 2017). The behaviour of unresolved physics are captured through sub-grid models, and we need to understand how physics behaves on these small scales in order to develop an appropriate sub-grid implementation for use on galactic scales.

In particular, the depth of photodissociation regions, where molecular hydrogen chemistry is set, can be less than 0.1 pc (Hollenbach and Tielens 1999). In a galaxy simulation, a PDR may be on the scale of an individual resolution element. Therefore, it is necessary that we understand and model the dynamics of PDRs in detail here first, as in future work, we may need to construct a sub-grid model of PDRs to properly determine the H_2 fraction in our simulated galaxies.

1.4 Aims of this Work

In this thesis, I study molecular hydrogen and its impact on galaxies. The physics of molecular hydrogen and radiation are intertwined, and both need to be developed simultaneously in order to simulate more realistic galaxies. The primary goal of this thesis is to establish what set of physics are needed to improve the coupling of radiation

to the ISM in galaxy-scale simulations. In particular, I develop, implement, and test a model for the formation and evolution of H_2 and its interaction with radiation. This model is developed in the context of the GASOLINE[1] smoothed particle hydrodynamics code alongside the TREVR2 radiative transfer method (Wadsley et al. 2017; Wadsley et al. 2023), but it should generalise to any galaxy simulation using a radiative transfer routine. GASOLINE is generally used for simulations of galaxies, and TREVR2 is a tree-based reverse ray-tracing method for radiative transfer. By working to correctly implement a model for H_2, I am able to identify and understand other processes such as photoelectric heating that need to be captured in order to complete this model of chemistry in the ISM.

In Chapter 2, I discuss the necessary physical and chemical process that must be captured in order to make a complete model of molecular hydrogen. This is followed by Chapter 3, in which I outline the specific choices made to implement the molecular hydrogen model into the GASOLINE chemical network, and highlight some of the methods developed to test that this model works correctly. This includes an idealized one-dimensional setup of an isolated cloud of gas exposed to an external radiation field, which simulates how the model behaves on highly resolved scales. I evaluate the choices of my implementation by presenting several tests of this method, which compare my model against established behaviours. Finally, in Chapter 4, I provide a summary of the work I have accomplished so far, and outline the science goals that I intend to pursue with this model in future works.

---

[1]This font will be used throughout this thesis to denote the names of simulation codes.

Chapter 2

Physics of the Interstellar Medium

"I write about molecules with great diffidence, having not yet rid myself of the tradition that 'atoms are physics, but molecules are chemistry'; but the new conclusion seems to make it likely that the above-mentioned elements H, O, and N will frequently form molecules."

Eddington (1937)

2.1   Chemistry

The baryonic component of matter in the universe is roughly 75% Hydrogen by mass, and 24% Helium. The remaining 1% of this mass is in the form of elements heavier than helium, which are referred to as metals (Ryden 2016). Any chemical network that is acceptable for astrophysical problems must at least track the evolution of Hydrogen and Helium. Heavier elements can contribute significantly to the overall cooling of astrophysical gas, but tracking each element incurs significant computing costs as the number of chemical interactions increases (Grassi et al. 2014; Richings et al. 2014a). Therefore, many networks will track the two ionization states of Hydrogen and the three ionization states of Helium, alongside a metallicity value to parameterise the abundance of heavier elements (Smith et al. 2017).

Molecular hydrogen is the most abundant molecule in the universe, and has generally been absent from the GASOLINE chemical network, with some exceptions (Christensen et al. 2012). This is partly because H_2 is complicated and has minimal impact on the dynamics of galaxies, but also because past simulations were unable to resolve the

15

high-density gas in which H_2 forms. Now that this gas is resolvable, a model for H_2 is necessary so that we can correctly simulate the molecular phase of the ISM. Additionally, detailed modeling of H_2 requires radiative transfer, which up until recently has been cost-prohibitive. In the nearby universe, after metal enrichment has polluted much of the interstellar medium of galaxies, cooling by molecular hydrogen is much smaller than the cooling contributed by metals. If, however, we want to couple far-ultraviolet radiation to the gas of the ISM (namely radiation in the range of 11.2 eV to 13.6 eV), then we need to include molecular hydrogen in our chemical network so that we can self-consistently evolve the chemical and thermodynamic state of the gas.

2.1.1 Equilibrium vs. non-equilibrium chemistry

The methods used to integrate the chemical state of our simulations can be divided into two major categories. Equilibrium solvers solve for the equilibrium state of the gas, and have the advantage of being relatively fast and stable. Such solvers are appropriate when the time needed for chemistry to reach equilibrium is shorter than other timescales in the system. For an example of an equilibrium chemistry solver, see the CLOUDY code (Ferland et al. 2017).

Meanwhile, non-equilibrium solvers solve for chemical state of the gas as a function of time. These are more at risk of being unstable than their equilibrium counterparts, and usually demand smaller timesteps to remain stable for each step of the integration. For instance, the non-equilibrium chemistry solver KROME (Grassi et al. 2014) has shown to be extremely robust, but also demands very large computation times. Non-equilibrium solvers are necessary if your chemical timescale is long compared to dynamical timescales, so that your system may change much faster than the chemistry can reach equilibrium, and non-equilibrium chemical processes become important. For instance, the out-of-equilibrium electron fraction in a cloud of gas that cools faster than the gas can recombine enables a pathway for H_2 formation (Shapiro and Kang 1987).

Ultimately, the choice between an equilibrium and non-equilibrium solver depends on what controls the dynamics and behaviour of the system you are trying to model. Additionally, when designing a chemical network, we need to balance the amount of detail we can afford to solve (ie. how fast we can solve chemistry relative to the rest of the simulation), with the need to solve things correctly and avoid large errors. Gnedin et al. (2009) show that making too many approximations to improve efficiency, such as operator splitting, can lead to incorrect behaviours and large errors.

Generally, the systems I am interested in solving are almost never in equilibrium. The timescale to form H_2 can be longer than local dynamical times, for which a non-equilibrium solver is necessary. Richings et al. (2014b) find that for a cloud of gas with pressure $P/k_B = 10^3$ cm^{-3}K and metallicity $Z = 0.1Z_\odot$, it can take up to ~ 1 Gyr for molecular hydrogen to reach equilibrium. Meanwhile, the free-fall time for typical molecular clouds in the ISM is on the order of 10 Myr (Chevance et al. 2023). Finally, the chemistry solver used in the GASOLINE code is a non-equilibrium solver, so the model I present in this thesis is designed for non-equilibrium chemistry (Wadsley et al. 2017).

2.1.2   The chemical network, simplified

Equations 2.1, 2.2, and 2.3 give the rate of change of HI, HII, and H_2 respectively based on the implementation by Christensen et al. (2012). This model is simpler than the model we eventually chose to adopt for our chemical network, but remains useful for explaining the fundamental chemical processes at play:

$$\dot{Y}_{\mathrm{HI}} = R_{\mathrm{HII}}Y_{\mathrm{HII}}n_{\mathrm{e^-}} - C_{\mathrm{HI}}Y_{\mathrm{HI}}n_{\mathrm{e^-}} - \xi_{\mathrm{HI}}Y_{\mathrm{HI}} - 2\dot{Y}_{\mathrm{H_2}} \tag{2.1}$$

$$\dot{Y}_{\mathrm{HII}} = -R_{\mathrm{HII}}Y_{\mathrm{HII}}n_{\mathrm{e^-}} + C_{\mathrm{HI}}Y_{\mathrm{HI}}n_{\mathrm{e^-}} + \xi_{\mathrm{HI}}Y_{\mathrm{HI}} \tag{2.2}$$

$$\begin{aligned}
\dot{Y}_{\mathrm{H_2}} = {} & R_d n_b Y_{\mathrm{HI}}(Y_{\mathrm{HI}} + 2Y_{\mathrm{H_2}}) \\
& + k_2 n_{\mathrm{H^-}}Y_{\mathrm{HI}} \\
& - Y_{\mathrm{H_2}}\zeta_{\mathrm{H_2}}^{\mathrm{LW}} \\
& - n_b Y_{\mathrm{H_2}}(k_7 Y_{\mathrm{HII}} + k_8 Y_{\mathrm{e^-}} + k_9 Y_{\mathrm{HI}} + k_{10}Y_{\mathrm{H_2}})
\end{aligned} \tag{2.3}$$

where n_b is the number density of baryons, and otherwise n_i denotes the number density of a species i. The reaction rate coefficients k_i are numbered as in Glover and Abel (2008). These describe the expected rate at which a reaction occurs per unit density per second, and are generally a function of temperature. k_2 is the rate of associative detachment for H_2 formation via HI and H$^-$. k_7, k_8, k_9, and k_{10} are the collisional ionization rates for collisions of H_2 with HII, e$^-$, HI, and H_2 respectively. R_{HII} and C_{HI} are rate coefficients for HII recombination and collisional ionization of HI with e$^-$ respectively. R_d is the rate coefficient for the formation of H_2 on dust grains. ξ_{HI} is the photoionization rate of HI, and $\zeta_{\mathrm{H_2}}^{\mathrm{LW}}$ is the rate of photodissociation of H_2 by photons in the Lyman-Werner band, with energies from 11.2 eV to 13.6 eV. Y_i is the fractional abundance of species i, defined as:

$$Y_i = \frac{n_i}{n_b} \tag{2.4}$$

In Equation 2.1, the fraction of neutral hydrogen is governed by four processes. These processes are represented by four terms; from left to right, we have recombination of HII and e⁻, ionization of HI by collisions with e⁻, photoionization of HI, and the net formation rate of H_2 from neutral hydrogen atoms. The fraction of ionized hydrogen, given by Equation 2.2, uses all the same rate coefficients as for neutral hydrogen, with the signs swapped. Simply put, for every neutral hydrogen that is ionized, an ionized hydrogen is created.

The exception to this behaviour comes from the formation and destruction of H_2. In the network presented here, every H_2 destruction process dissociates the H_2 molecule into two HI atoms. The $-2\dot{Y}_{H_2}$ term is included in Equation 2.1 for $\dot{Y}_{HI}$ to account for this behaviour, but is absent from Equation 2.2 because molecular hydrogen cannot directly dissociate to form ionized hydrogen without first passing through the neutral atomic phase.

Note that in practice, to obtain the balance of HII, we do not explicitly solve an equation for $\dot{Y}_{HII}$. Instead, assuming that the total amount of hydrogen across all ionization states (Y_H) remains constant throughout the integration, we can solve for the formation of HII implicitly:

$$Y_{HII} = Y_H - Y_{HI} - 2Y_{H_2} \tag{2.5}$$

2.2 Detailed Chemistry of Molecular Hydrogen

We decided to adopt the more in-depth chemical network presented by Gnedin and Kravtsov (2011), summarized in Tables 2.1, 2.2, and 2.3. This network provides a comprehensive summary of all the hydrogen and helium ionization states, tracks the formation and destruction of molecular hydrogen, and enables gas-phase pathways to form H_2 using H^- and H_2^+. Adopting this network provided updated forms for the chemical balance of HI and H_2.

Species	Reaction	Reactants $\rightarrow$ Products
H_2	Formation on dust grains	$H_I + H_I + gr \rightarrow H_2 + gr$
	Associative detachment (H^-)	$H_I + H^- \rightarrow H_2 + e^-$
	Charge exchange (H_2^+)	$H_I + H_2^+ \rightarrow H_{II} + H_2$
	Photodissociation (LW)	$H_2 + \gamma_{LW} \rightarrow H_I + H_I$
	Photoionization (15.2+ eV)	$H_2 + \gamma_{15.2+} \rightarrow H_2^+ + e^-$
	Cosmic ray ionization	$H_2 + \gamma_{CR} \rightarrow H_I + H_I$
	Collisional dissociation	$H_2 + e^- \rightarrow H_I + H_I + e^-$
	. . .	$H_2 + e^- \rightarrow H_I + H^-$
	. . .	$H_2 + H_2 \rightarrow H_I + H_I + H_2$
	. . .	$H_2 + H_I \rightarrow H_I + H_I + H_I$
	. . .	$H_2 + H_{II} \rightarrow H_I + H_I + H_{II}$
	. . .	$H_2 + He_I \rightarrow H_I + H_I + He_I$
	. . .	$H_2 + He_{II} \rightarrow He_I + H_I + H_{II}$
	Charge exchange (H_{II})	$H_2 + H_{II} \rightarrow H_2^+ + H_I$
	Charge exchange (He_{II})	$H_2 + He_{II} \rightarrow H_2^+ + He_I$

TABLE 2.1: Summary of all H_2 reactions in the chemical network. Note that the process named cosmic ray ionization is listed alongside a dissociation reaction, which is how this process is represented in the code. See Section 2.3.5 for details.

Species	Reaction	Reactants $\rightarrow$ Products
HI	Radiative recombination	HII + e$^-$ $\rightarrow$ HI + γ
	Collisional ionization (e$^-$)	HI + e$^-$ $\rightarrow$ HII + 2e$^-$
	Photoionization	HII + γ $\rightarrow$ HII + e$^-$
	Cosmic ray ionization	HII + γ_{CR} $\rightarrow$ HII + e$^-$
	Formation of H$_2$ on dust grains	HI + HI + gr $\rightarrow$ H$_2$ + gr
	Radiative association (H$^-$)	HI + e$^-$ $\rightarrow$ H$^-$ + γ
	Associative detachment (H$^-$)	HI + H$^-$ $\rightarrow$ H$_2$ + e$^-$
	Radiative association (H$_2^+$)	HI + HII $\rightarrow$ H$_2^+$ + γ
	Charge exchange (H$_2^+$)	HI + H$_2^+$ $\rightarrow$ HII + H$_2$
	Photodissociation (LW)	H$_2$ + γ_{LW} $\rightarrow$ HI + HI
	Charge exchange (HeII)	HI + HeII $\rightarrow$ HII + HeI
	Cosmic ray ionization	H$_2$ + γ_{CR} $\rightarrow$ HI + HI
	Charge exchange (HII and H$^-$)	HII + H$^-$ $\rightarrow$ 2HI
	Collisional ionization (H$_2^+$ and e$^-$)	H$_2^+$ + e$^-$ $\rightarrow$ 2HI
	Collisional ionization (H$^-$ and e$^-$)	H$^-$ + e$^-$ $\rightarrow$ HI + 2e$^-$
	Collisional ionization (H$^-$)	H$^-$ + HI $\rightarrow$ 2HI + e$^-$
	Collisional ionization (H$^-$ and HeII)	H$^-$ + HeII $\rightarrow$ HI + HeII + e$^-$
	Collisional ionization (H$^-$ and HeI)	H$^-$ + HeI $\rightarrow$ HI + HeI + e$^-$
	Collisional dissociation (H$_2$)	H$_2$ + e$^-$ $\rightarrow$ HI + HI + e$^-$
	. . .	H$_2$ + e$^-$ $\rightarrow$ HI + H$^-$
	. . .	H$_2$ + H$_2$ $\rightarrow$ HI + HI + H$_2$
	. . .	H$_2$ + HI $\rightarrow$ HI + HI + HI
	. . .	H$_2$ + HII $\rightarrow$ HI + HI + HII
	. . .	H$_2$ + HeI $\rightarrow$ HI + HI + HeI
	. . .	H$_2$ + HeII $\rightarrow$ HeI + HI + HII
	Charge exchange (H$_2$ and HII)	H$_2$ + HII $\rightarrow$ H$_2^+$ + HI
	Charge exchange (HeI and HII)	HeI + HII $\rightarrow$ HeII + HI

TABLE 2.2: Summary of all HI reactions in the chemical network.

Species	Reaction	Reactants $\rightarrow$ Products
HeI	Radiative recombination	HeII + e⁻ $\rightarrow$ HeI + γ
	Collisional ionization (e⁻)	HeI + e⁻ $\rightarrow$ HeII + 2e⁻
	Photoionization	HeI + γ $\rightarrow$ HeII + e⁻
	Collisional dissociation (H_2 and HeII)	H_2 + HeII $\rightarrow$ HeI + HI + HII
	Charge exchange (H_2 and HeII)	H_2 + HeII $\rightarrow$ H_2^+ + HeI
	Charge exchange (HeII and HI)	HeII + HI $\leftrightarrow$ HeI + HII
	Charge exchange (H⁻ and HeII)	H⁻ + HeII $\leftrightarrow$ HI + HeI
HeII	Radiative recombination	HeIII + e⁻ $\rightarrow$ HeII + γ
	Collisional ionization	HeII + e⁻ $\rightarrow$ HeIII + 2e⁻
	Photoionization	HeII + γ $\rightarrow$ HeIII + e⁻
	All HeI processes	See above

TABLE 2.3: Summary of all HeI, HeII reactions in the chemical network.

The Gnedin and Kravtsov (2011) chemical network gives us an updated form for the chemical balance of HI:

$$
\begin{aligned}
\dot{Y}_{\text{HI}} = \;& R_{\text{HII}} Y_{\text{HII}} n_{\text{e}^-} && \text{Radiative recombination} \\
& - C_{\text{HI}} Y_{\text{HI}} n_{\text{e}^-} && \text{Collisional ionization with e}^- \\
& - \xi_{\text{HI}} Y_{\text{HI}} && \text{Photoionization} \\
& - 2(R_d n_b Y_{\text{HI}} (Y_{\text{HI}} + 2Y_{\text{H}_2})) && \text{Formation of H}_2 \text{ from 2HI on dust grains} \\
& - k_1 n_b Y_{\text{e}^-} Y_{\text{HI}} && \text{Radiative association to form H}^- \\
& - k_2 n_{\text{H}^-} Y_{\text{HI}} && \text{Associative detachment to form H}_2 \\
& - k_3 n_b Y_{\text{HII}} Y_{\text{HI}} && \text{Radiative association to form H}_2^+ \\
& - k_4 n_{\text{H}_2^+} Y_{\text{HI}} && \text{Charge exchange to form H}_2 \\
& + 2(Y_{\text{H}_2} \zeta_{\text{H}_2}^{\text{LW}}) && \text{Photodissociation of H}_2 \text{ to produce 2HI} \\
& + \cdots && \text{Everything else}
\end{aligned}
$$

where the reaction rate coefficients k_i are taken from Glover and Abel (2008). This method adds a number of reactions involving HI for the formation of H_2^+ and H^-, both of which are necessary for the H_2 gas-phase formation pathways (see Section 2.2.2). Remaining terms which are not reproduced here include collisional ionization and charge exchange reactions that are important for completing the chemical network but are numerous to list and are all similar in their expression. These can be found in Table 2.2.

The Gnedin and Kravtsov (2011) chemical network introduce a few additional kinds of reactions that require some definition. Radiative association is the process by which two smaller gas-phase species combine to form a larger molecule, emitting a photon in the process (Bates and Herbst 1988). This process is necessary for forming the ions H^- and H_2^+. Associative detachment is the combination of an anion and a neutral atom to form a neutral molecule, detaching the anion's electron in the process (Hassan et al. 2022). Associative detachment is the primary mechanism for the gas-phase formation of H_2 via the H^- anion. Finally, charge exchange is a process in which two ions or atoms collide, and an electron is transferred from one to the other (Bransden 1972). This is distinct from collisional ionization, where the collision frees an electron. Charge exchange describes the gas-phase formation of H_2 via the H_2^+ cation.

The Gnedin and Kravtsov (2011) chemical network includes a few additional pathways for the formation and destruction of H_2:

$$
\begin{aligned}
\dot{Y}_{\mathrm{H}_2} = {} & R_d n_b Y_{\mathrm{HI}}(Y_{\mathrm{HI}} + 2Y_{\mathrm{H}_2}) && \text{Formation on dust grains} \\
& + k_2 n_{\mathrm{H}^-} Y_{\mathrm{HI}} && \text{Gas phase formation via } \mathrm{H}^- \\
& + k_4 n_{\mathrm{H}_2^+} Y_{\mathrm{HI}} && \text{Gas phase formation via } \mathrm{H}_2^+ \\
& - Y_{\mathrm{H}_2} \zeta_{\mathrm{H}_2}^{\mathrm{LW}} && \text{Photodissociation by LW photons} \\
& - Y_{\mathrm{H}_2} \xi_{\mathrm{H}_2}^{15.2+} && \text{Photoionization of } \mathrm{H}_2 \\
& - n_b Y_{\mathrm{H}_2}(k_i Y_i + \cdots) && \text{Collisional dissociation \& charge exchange}
\end{aligned}
$$

Photodissociation by LW photons and photoionization of H_2 will be discussed in Section 2.3. Again, the collisional ionization and charge exchange terms are numerous to list, but are summarized in Table 2.1. This equation is governed by several physical processes which contribute to the formation and destruction of molecular hydrogen.

2.2.1 Formation on dust grains

In regions of the ISM with dust and metallicity greater than 1% solar ($\sim 0.01 Z_\odot$), dust grains provide the dominant pathway by which H_2 can form (Shaw et al. 2005). HI atoms collide with and stick to dust grains, and then migrate across the grain surface to form H_2 (Wolfire et al. 2008). The rate of formation of H_2 on dust grains is given by Abel et al. (1997):

$$
\dot{Y}_{\mathrm{H}_2,\mathrm{dust}} = R_d n_b Y_{\mathrm{HI}}(Y_{\mathrm{HI}} + 2Y_{\mathrm{H}_2}) \tag{2.6}
$$

where R_d is the rate coefficient for the dust grain formation pathway, n_b is the number density of baryons, Y_{HI} is the abundance of HI and Y_{H_2} the abundance of H_2.

The rate coefficient for the dust grain formation pathway takes a number of different forms. In past H_2 chemical networks (Christensen et al. 2012), we have taken the rate coefficient from to be Equation 3 from Gnedin et al. (2009), which is based on the empirically motivated value from Wolfire et al. (2008):

$$
R_d = 3.5 \times 10^{-17} Z C_\rho \ \mathrm{cm}^3 \ \mathrm{s}^{-1} \tag{2.7}
$$

where Z is the metallicity of the gas relative to the solar metallicity $Z_\odot$, and C_ρ is the sub-grid clumping factor. The clumping factor exists to capture the increased H_2 formation rate when dust clumps into denser knots that cannot be resolved by the

simulation. Typical values for this clumping factor range from $10 < C_\rho < 100$ (Sillero et al. 2021), but this factor is typically only used when simulating on the scale of galaxies. For simulations of individual clouds or photodissociation regions, no clumping factor is used; effectively $C_\rho = 1$. Most of the tests performed later in this thesis are of isolated clouds, and therefore take $C_\rho = 1$.

There are, however, some variations on the formation coefficient R_d that depend on temperature. In Röllig et al. (2007), the authors use a coefficient R_d that is proportional to $\sqrt{T}$:

$$R_d = 3.8 \times 10^{-18} \sqrt{T} Z C_\rho \text{ cm}^3 \text{ s}^{-1} \tag{2.8}$$

I bring this form up now because the authors use this in their comparison tests to establish a benchmark between numerous PDR codes. When comparing my code against this benchmark, I must use this form of R_d.

More complicated version of the rate coefficient also exist, in an attempt to capture how the rate of HI collisions with dust grains increases with T, while the sticking coefficient for HI onto grain surfaces decreases with T (Wolfire et al. 2008). Consider this rate coefficient from Equation 3.8 of Hollenbach and McKee (1979); I present the form from Kim et al. (2023):

$$R_d = 3 \times 10^{-17} Z_d \frac{2T_2^{0.5}}{1 + 0.4T_2^{0.5} + 0.2T_2 + 0.08T_2^2} \text{ cm}^3\text{s}^{-1} \tag{2.9}$$

where $T_2 = T/100\text{K}$. The more complex temperature dependence means that the rate coefficient reaches a peak value of 3.7×10^{-17} cm^{3}s^{-1} and decreases rapidly for $T > 300$K. Notably, this equation is adopted by the CLOUDY code (Ferland et al. 2017) and in the TIGRESS simulations (Kim et al. 2023), which simulate individual high-density regions of the ISM (Kim and Ostriker 2017). It is not immediately obvious which of these three possibilities is the best choice for the formation rate, as the rate coefficient for the formation of H_2 on dust grains is poorly constrained. Unless stated otherwise, I will use the constant coefficient from Equation 2.7 throughout this thesis.

2.2.2 Gas-phase formation

There are two remaining pathways to form H_2, which are referred to as the gas-phase formation pathways. No dust grains are required in the gas-phase formation pathways, so these processes can proceed in environments with very low metallicity, and are essential

for determining the abundance of H_2 at high redshifts (Bovino and Galli 2019). We will see this more in Section 3.10.

The first gas-phase formation pathway follows associative detachment of H^- ($HI + H^- \rightarrow H_2 + e^-$). The rate equation for this process depends on the density of H^- and the abundance of HI as follows:

$$\dot{Y}_{H_2,H^-} = k_2 n_{H^-} Y_{HI} \tag{2.10}$$

where the rate coefficient k_2 is given by Glover and Abel (2008). The value of k_2 varies with T, but a typical value for this coefficient is $k_2 \sim 1.428 \times 10^{-9}$ cm^{3}s^{-1}.

The second gas-phase formation pathway follows charge exchange of H_2^+ with atomic hydrogen ($HI + H_2^+ \rightarrow HII + H_2$). The rate equation for this process the density of H_2^+ and the abundance of HI as follows:

$$\dot{Y}_{H_2,H_2^+} = k_4 n_{H_2^+} Y_{HI} \tag{2.11}$$

where once again, the rate coefficient k_4 is given by Glover and Abel (2008). This rate coefficient has a constant value of $k_4 = 6.4 \times 10^{-10}$ cm^{3}s^{-1}.

Although both rate coefficients k_2 and k_4 are much larger than R_d from Equation 2.7, the actual rates at which H_2 forms through either of this processes is dependent on the abundance of H^- or H_2^+ respectively, which are typically much less than 1. Hence, the dust grain formation pathway still typically dominates whenever dust is present.[1]

Equilibrium assumption for H^- and H_2^+

To include these gas-phase formation processes, the abundance of H^- and H_2^+ would need to be solved for in the full chemical network. However, Gnedin and Kravtsov (2011) propose a reduced chemical network which assumes that H^- and H_2^+ are always in equilibrium, thus avoiding the expense of tracking H^- and H_2^+ explicitly. H^- and H_2^+ reach equilibrium on relatively short timescales, on the order of 10^{12} s, or ~ 0.1 Myr, which is shorter than the typical cooling or dynamical timescale of cool, H_2-forming gas, which typically exceeds 1 Myr (Glover et al. 2006).

---

[1]The CLOUDY documentation (Hazy 3, page 33) suggests that the H^- formation route is faster than dust grain formation for conditions of moderate ionization $\frac{n_{e^-}}{n_H} > 4 \times 10^{-3}$, even when grains are present (Shaw et al. 2005).

This assumption breaks down in situations where the gas can cool or collapse faster than H^- or H_2^+ can reach equilibrium *and* either gas-phase formation process provides the dominant formation pathway for gas in that phase (temperature, density, and metallicity). Abel et al. (1997) and Gnedin and Kravtsov (2011) suggest that the equilibrium assumption should be satisfied in all regimes relevant to cosmology, so we assume that it is reasonable that the fraction of H^- and H_2^+ should quickly reach equilibrium within a given integration step, but should be mindful of any dynamical processes with timescales less than 0.1 Myr.

To implement this assumption in our chemical network, we assume that any H^- that forms during a step will be destroyed through collisional ionization to form H_I, and that any H_2^+ that forms during a step dissociates collisionally to form $2H_I$. During the step, either species can be used like a catalyst to enable the formation of H_2. Since H_2 can be ionized to make H_2^+, H_2 ionization functionally becomes similar to H_2 dissociation, as any newly ionized H_2^+ can readily dissociate to form $2H_I$. In this manner, H_2^+ that is formed by radiative association creates a pathway to form H_2, while ionization of H_2 through cosmic rays or ionizing radiation provides a pathway to *destroy* H_2 (Bovino and Galli 2019).

To solve for the density of H^- and H_2^+, we simply balance the rates of formation (numerator) and destruction (denominator). The H^- equilibrium assumption is based on Gnedin and Kravtsov (2011), with rate coefficients k_i from Glover and Abel (2008):

$$n_{H^-} = \frac{k_1 n_{e^-} n_{H_I} + k_{23} n_{e^-} n_{H_2}}{\Gamma_A + k_2 n_{H_I} + k_5 n_{H_{II}} + k_{14} n_{e^-} + k_{15} n_{H_I} + k_{16} n_{H_{II}} + k_{28} n_{He_{II}} + k_{29} n_{He_I}}$$

(2.12)

The coefficients k_i describe the rate of each contributing reaction. k_1 describes radiative association ($H_I + e^- \rightarrow H^- + \gamma$), k_{23} describes collisional dissociation of H_2 with e^- where the electron attaches to one of the H_I atoms ($H_2 + e^- \rightarrow H^- + H_I$), k_2 describes associative detachment ($H_I + H^- \rightarrow H_2 + e^-$), k_5 describes collisional ionization of H^- with H_{II} ($H^- + H_{II} \rightarrow 2H_I$), k_{14} describes collisional ionization with e^- ($H^- + e^- \rightarrow H_I + 2e^-$), k_{15} describes collisional ionization with H_I ($H^- + H_I \rightarrow 2H_I + e^-$), k_{16} describes associative detachment with H_{II} ($H_{II} + H^- \rightarrow H_2^+ + e^-$), k_{28} describes charge exchange with He_{II} ($H^- + He_{II} \rightarrow H_I + He_I$), and k_{29} describes collisional ionization with He_I ($H^- + He_I \rightarrow He_I + H_I + e^-$). Note that associative detachment with H_{II} (k_{16}) does not appear anywhere else in our network because the H_{II} abundance is solved for implicitly. Γ_A is the photodetachment of H^-; see Section 2.2.3 for more details.

The H_2^+ equilibrium assumption is similarly taken from Gnedin and Kravtsov (2011), with rate coefficients k_i from Glover and Abel (2008) as follows:

$$n_{H_2^+} = \frac{\Gamma_D n_{H_2} + k_3 n_{HI} n_{HII} + k_7 n_{H_2} n_{HII} + k_{16} n_{HII} n_{H^-} + k_{25} n_{H_2} n_{HeII}}{\Gamma_B + \Gamma_C + k_4 n_{HI} + k_6 n_{e^-}} \quad (2.13)$$

Here, k_3 describes radiative association of HI with HII (HI + HII $\rightarrow$ H_2^+ + γ), k_7 describes collisional ionization of H_2 with HII (H_2 + HII $\rightarrow$ H_2^+ + HI), k_{16} describes associative detachment of HII with H^- (HII + H^- $\rightarrow$ H_2^+ + e^-), k_{25} describes charge exchange of H_2 with HeII (H_2 + HeII $\rightarrow$ H_2^+ + HeI), k_4 describes charge exchange of HI with H_2^+ (HI + H_2^+ $\rightarrow$ H_2 + HII), and k_6 describes collisional dissociation of H_2^+ with e^- (H_2^+ + e^- $\rightarrow$ 2HI). Γ_D is the rate of photoionization[2] of H_2.

2.2.3 Missing physics

Before continuing, I would like to list which processes I did *not* include from the Gnedin and Kravtsov (2011) chemical network, along with some justification as to why these processes were excluded.

- Three-body reactions for the formation of H_2 (reactions 30, 31, and 32 in Glover and Abel 2008). These three-body reactions are only significant at densities $n \geq 10^8 \text{cm}^{-3}$, which is much higher than the densities galaxy simulations are currently capable of resolving.

- Photodetachment of H^- (H^- + γ $\rightarrow$ HI + e^-), labelled Γ_A in Gnedin and Kravtsov (2011), is currently not implemented in the radiative transfer routine because this would require adding a new radiation band, as photodetachment of H^- is triggered by photons of lower energies than those in the bands captured by radiative transfer routine. Neglecting this process significantly influences the amount of primordial H_2 that forms, so we discuss a provisional implementation for photodetachment in Section 3.10.

- Photodissociation of H_2^+, labelled Γ_B and Γ_C in Gnedin and Kravtsov (2011). These two coefficients describe the reaction rates for H_2^+ + γ $\rightarrow$ HI + HII and H_2^+ + γ $\rightarrow$ 2HII + e^- respectively. My justification for not including this is that we expect any H_2^+ to rapidly be destroyed by collisions with free e^-, but again in

---

[2]In this thesis, I will use ξ_{H_2} to denote the photoionization rate of H_2. Γ_i generally denotes the heating due to photoionization of species i. Only in these equations from Gnedin and Kravtsov (2011) will Γ_i denote a photoionization process.

Section 3.10 we find that modeling the dissociation of H_2^+ is necessary to obtain correct abundances for H_2 at very high redshifts.

- Direct photodissociation of H_2 by photons with energy $h\nu > 13.6$ eV, labelled Γ_E in Gnedin and Kravtsov (2011) is not included because it is unclear how this process interacts with shielding. Additionally, since shielding permits a trace H_I fraction to persist up to very high depths, for any situation where we have H_2 we expect there to be available H_I that can more readily absorb this radiation.

2.2.4 Cooling Processes

Here, I outline some of the most dominant cooling and heating processes in our model. This is not an exhaustive list of all processes, but rather a short list of those processes that are most important when considering the formation and destruction of H_2. All the processes listed here are accounted for in our model.

Radiative Recombination

Recombination is the process by which ionized hydrogen (H_{II}) and a free electron (e^-) recombine to form neutral hydrogen: ($H_{II} + e^- \rightarrow H_I + \gamma$). The newly formed H_I emits photons as the electron de-excites to the ground state. These photons remove energy from the system, so recombination cools the gas. The cooling rate due to radiative recombination of H_{II} ($n^2\Lambda_{\mathrm{recomb}}$) is given by the following equation (Tielens 2005):

$$n^2\Lambda_{\mathrm{recomb}} = n_{e^-} n_{H_{II}} kT\beta(T) \tag{2.14}$$

where $\beta(T)$ is the recombination rate coefficient, k is the Boltzmann constant, and T is the temperature of the gas. Recombination is most effective when the gas temperature is around $T \sim 10^4$ K, when hydrogen is fully ionized. At a temperature of $T = 10^4$ K, the recombination coefficient has a value of $\beta(T = 10^4 \text{ K}) \sim 4.18 \times 10^{-13}$ erg s^{-1} (Tielens 2005). As recombination proceeds, gas cools, and the ionized fraction of hydrogen drops. At $T < 10^4$ K, when gas becomes mostly neutral, the effectiveness of recombination cooling decreases markedly, and other forms of cooling are required to cool the gas further.

Line Cooling

Collisions with free electrons can raise the bound electrons of an atom into an excited state. These bound, excited electrons spontaneously de-excite by emitting a photon,

cooling the gas. Line cooling by HI (Lyman-α), HeI, and HeII are very effective coolants at temperatures above $T > 10^4$ K (Tielens 2005). At lower temperatures, cooling is dominated by the excitation of fine structure levels of trace elements (Tielens 2005). For high density and metallicity, line cooling from CII and OI are the dominant coolants in the ISM (Wolfire et al. 1995; Wolfire et al. 2003). Since our chemical network does not explicitly track the abundance of each individual metal species, line cooling rates from metals are accounted for using a single cooling function which is tabulated based on density, temperature, and metallicity. We refer to this function as the metal cooling table.

Cooling by Molecular Hydrogen

When H_2 collides with another particle, some kinetic energy of that collision is transferred into rotational/vibrational energy as H_2 excites. H_2 can then spontaneously de-excite to the ground state by emitting a photon, which carries that energy away from the system (Glover and Abel 2008). The excitation of H_2 is typically dominated by collisions with HI, HII, e⁻, HeI, and H_2. The probability of each collisional process varies with temperature, so we use Table 8 from Glover and Abel (2008) to fit these cooling functions. The contribution that H_2 provides to cooling is relatively small, and is only important in an environment with low metallicity.

2.2.5   Heating Processes

Photoionization and Photodissociation

To ionize an atom, photons must exceed the energy needed to unbind an electron from the ground state. Any excess energy from that photon is given to the ionized electron, which transfers that energy to the gas. Heating by photoionization is detailed in Section 3.4.3. On average, the dissociation of a H_2 molecule into 2 HI atoms by a Lyman-Werner photon deposits 0.4 eV of energy into the gas (Gnedin and Kravtsov 2011). The process of photodissociation is explained in Section 2.3.1.

Photoelectric Effect

The photoelectric effect is the dominant heating effect in the ISM (Wolfire et al. 2003). Ultraviolet photons (5.6 eV $< h\nu <$ 13.6 eV) are absorbed by grains to create energetic electrons, which can escape the grain and transfer several eV of energy to the gas (Tielens 2005). This heating process is only functional in regions where dust grains are present.

Cosmic Ray Heating

Cosmic rays are relativistic particles, primarily protons, that are produced by supernova remnants (Ackermann et al. 2013). Ionization of H$\textsc{i}$ and H$_2$ by collisions with cosmic rays provides a source of heating that persists to high column densities in atomic and molecular clouds. The cosmic ray heating rate is taken from Glover and Mac Low (2007), given by Equation 2.15:

$$\Gamma_{\text{CR}} = 3.2 \times 10^{-28} \left(\frac{\xi}{10^{-17} \text{ s}^{-1}} \right) n \text{ erg s}^{-1} \text{ cm}^{-3} \tag{2.15}$$

where ξ is the rate of cosmic ray ionization of H$\textsc{i}$ and n is the number density of the gas.

2.3   Photochemistry

2.3.1   Lyman-Werner band: dissociating H$_2$

The easiest way for photons to dissociate H$_2$ is through the two-step Solomon process (Field et al. 1966; Stecher and Williams 1967) triggered through radiation in the Lyman-Werner band (11.2 eV to 13.6 eV). The two-step Solomon process is illustrated in Figure 2.1, reproduced from Hollenbach and Tielens (1999), and functions as follows: H$_2$ can absorb a photon to enter an excited rotational-vibrational state. The H$_2$ molecule can then spontaneously decay from that excited state. Roughly 85% of these decays do not result in dissociation,[3] but instead will return the molecule to a bound vibrational state (Allison and Dalgarno 1969), and the molecule will cascade down through these bound vibrational states to the ground state. Below some critical density (around 10^4 cm^{-3}, Hollenbach and Tielens 1999), the energy from these bound vibrational states is lost through spontaneous emission in the infrared band, so the energy leaves the gas. Above this critical density, collisional deexcitation is more probable, so this energy is transferred back to the gas (Bovino and Galli 2019). This heating process is called ultraviolet pumping. We do not expect to exceed this critical density at the current resolution of galaxy simulations, but for future reference, Equation 37 of Kim et al. (2023) gives a functional form for heating due to H$_2$ ultraviolet pumping. The point we wish to emphasize here is that roughly 85% of Lyman-Werner photon absorptions do not actually lead to a dissociation event, but do reprocess the radiation into a lower energy band, removing the photon from the beam. Below some critical density, this process removes the Lyman-Werner photon without even heating the gas.

---

[3]We defer discussion of dissociation momentarily, because it is the simpler of the two outcomes.
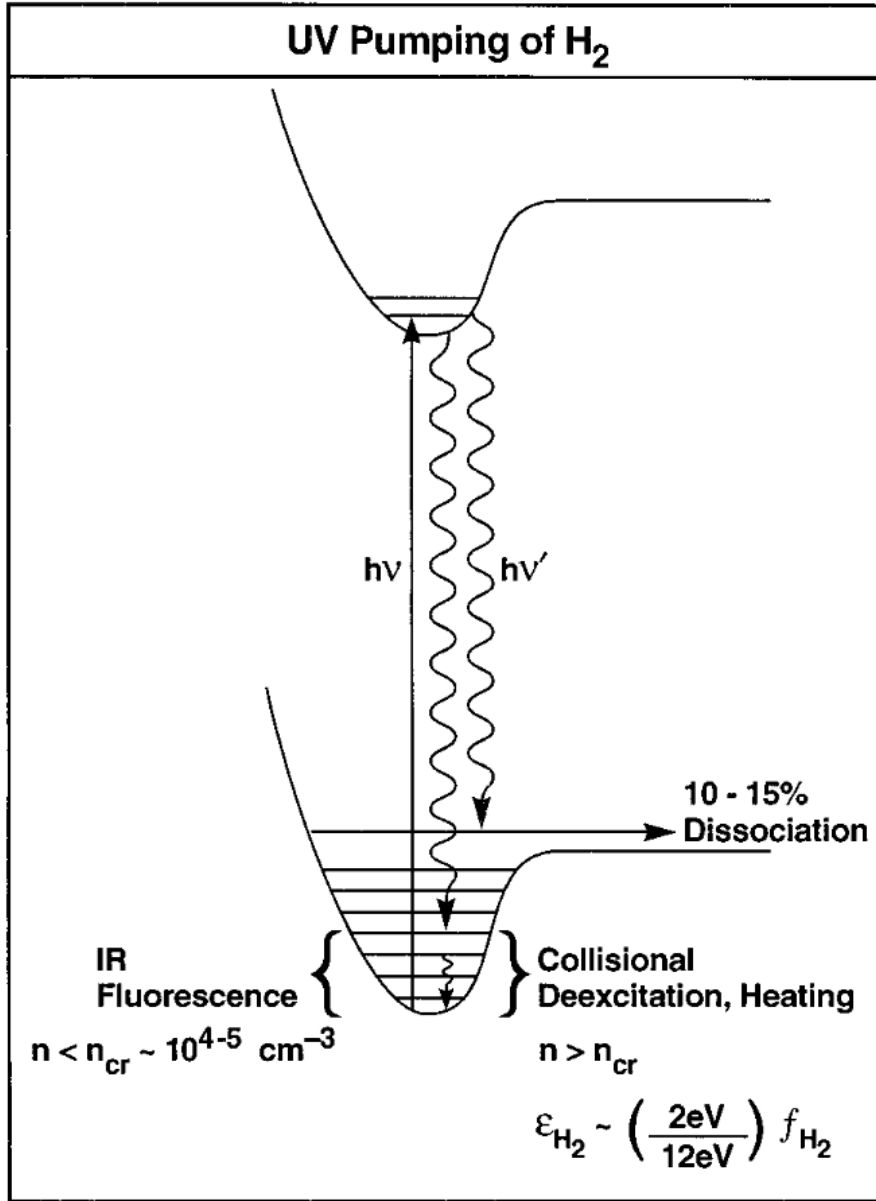
FIGURE 2.1: Reproduction of Figure 8 from Hollenbach and Tielens (1999) showing the energy level transitions of the H_2 molecule when absorbing a LW photon of energy $h\nu$. Axes are not labeled, but show the energy of each state (y-axis) vs. inter-nuclear separation of the Hydrogen atoms (x-axis). The molecule absorbs a photon of energy $h\nu$ to enter an excited state. Next, the molecule will spontaneously decay from this excited state by emitting a photon with energy $h\nu'$. $\sim 85\%$ of these decays will return the molecule to a bound vibrational state, while $\sim 15\%$ of these transitions will decay to the continuum and cause the H_2 molecule to dissociate.
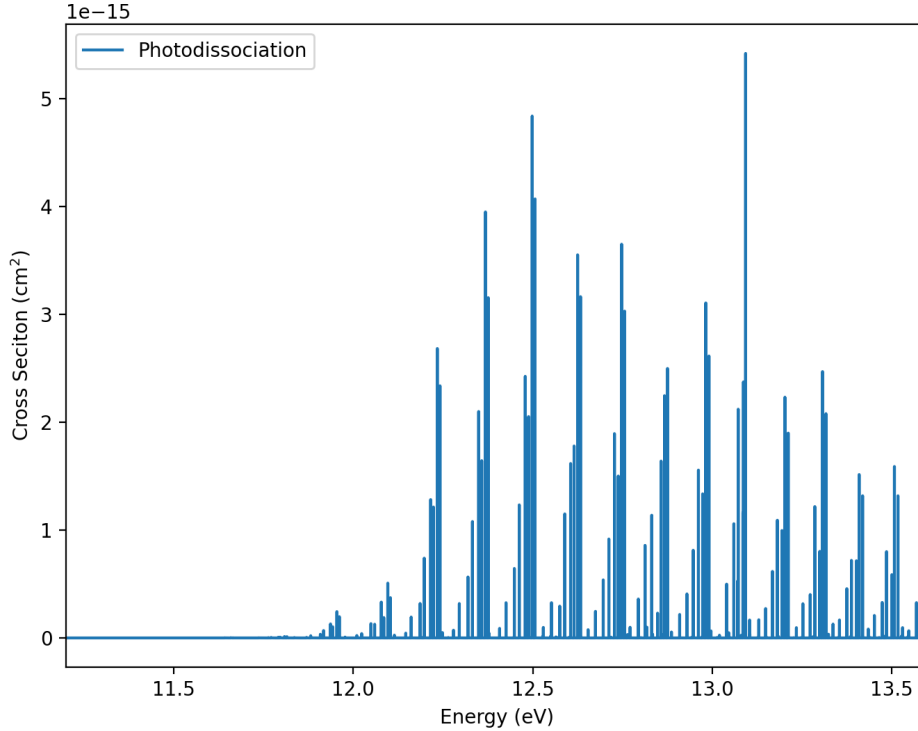
FIGURE 2.2: Cross section for the photodissociation of H_2 from the ground state as a function of incoming photon energy, generated with data from Heays et al. (2017). The displayed range of energies covers the Lyman-Werner radiation band from 11.2 eV to 13.6 eV. This figure illustrates the line dominated nature of the H_2 cross section. The tallest points on this plot correspond to the deepest line centers in the Lyman-Werner band.

Otherwise, roughly 15% of decays from the excited state will decay to the continuum, causing the molecule to dissociate (Draine and Bertoldi 1996). The complication with modeling the Solomon process is that it is a line based method, caused by distinct energy level transitions. The cross section for H_2 dissociation is shown in Figure 2.2 based on data from Heays et al. (2017). This has a dramatically different shape from the cross section for photoionization for other species in our chemical network, which can be fit with a single power law (Baumschlager et al. 2023). In some codes, dissociation is computed by integrating over thousands of bins in the LW band in order to capture this entire spectrum (Ricotti et al. 2002; Shaw et al. 2005; Goicoechea and Le Bourlot 2007). Other authors have proposed functional fits to parameterize this behaviour as a

function of depth (Draine and Bertoldi 1996). Nonetheless, this line based cross section dramatically alters how radiation and molecular hydrogen interact.

2.3.2 Shielding

As Lyman-Werner radiation travels through a cloud of H_2, photons from the line centers of the spectrum (Figure 2.2) are rapidly removed to dissociate H_2, and the gas becomes optically thick to those photons. Once the Doppler cores of these lines are all used up, only photons in the damping line wings remain available for photodissociation (Stecher and Williams 1967). So, as the optical depth into the cloud increases, the effective cross-section for dissociation decreases. Normally, the photoionization rate of atomic gas scales with flux, which is attenuated as $e^{-\tau}$. However, the complicated structure of absorption lines for molecular hydrogen means that the effective dissociation rate for H_2 as a function of depth has a complicated functional form given by Equation 2.17.

Instead of simulating each rovibrational energy level transition in detail, we can parameterize the behaviour of shielding by using a shielding function. The simplified version of the shielding equation from Draine and Bertoldi (1996) is given by Equation 2.16 and is useful for gaining a qualitative understanding of the behaviour:

$$f_{\text{shield}}(N_{H_2}) = \begin{cases} 1 & \text{for } N_{H_2} < 10^{14} \text{ cm}^{-2} \\ (N_{H_2}/10^{14} \text{ cm}^{-2})^{-0.75} & \text{for } N_{H_2} > 10^{14} \text{ cm}^{-2} \end{cases} \tag{2.16}$$

Here, we see that shielding by H_2 is not significant until the column density of H_2 reaches 10^{-14} cm^{-2}. For column densities deeper than 10^{-14} cm^{-2} the photodissociation rate drops off roughly as a function of $(N_{H_2})^{-\frac{3}{4}}$, although this approximation does not apply for arbitrarily large column densities ($N_{H_2} \to \infty$) (Draine and Bertoldi 1996).

The full shielding equation from Draine and Bertoldi (1996) will be used in our model, and is given by Equation 2.17:

$$f_{\text{shield}}(N_{H_2}) = \frac{0.965}{(1 + x/b_5)^2} + \frac{0.035}{(1 + x)^{0.5}} e^{-8.5 \times 10^{-4}(1+x)^{0.5}} \tag{2.17}$$

where $x = N_{H_2}/5 \times 10^{14}$ cm^{-2} and $b_5 = b/10^5$ cm s^{-1} is the turbulent Doppler parameter. This shape of this function is illustrated in Figure 2.3.

The shielding function presented in Equation 2.17 is used in place of opacity to obtain the dissociation rate of H_2 as a function of column density of H_2, $\zeta_{\text{diss}}(N_{H_2})$. This functional fit to dissociation was originally provided by Equation 40 of Draine and
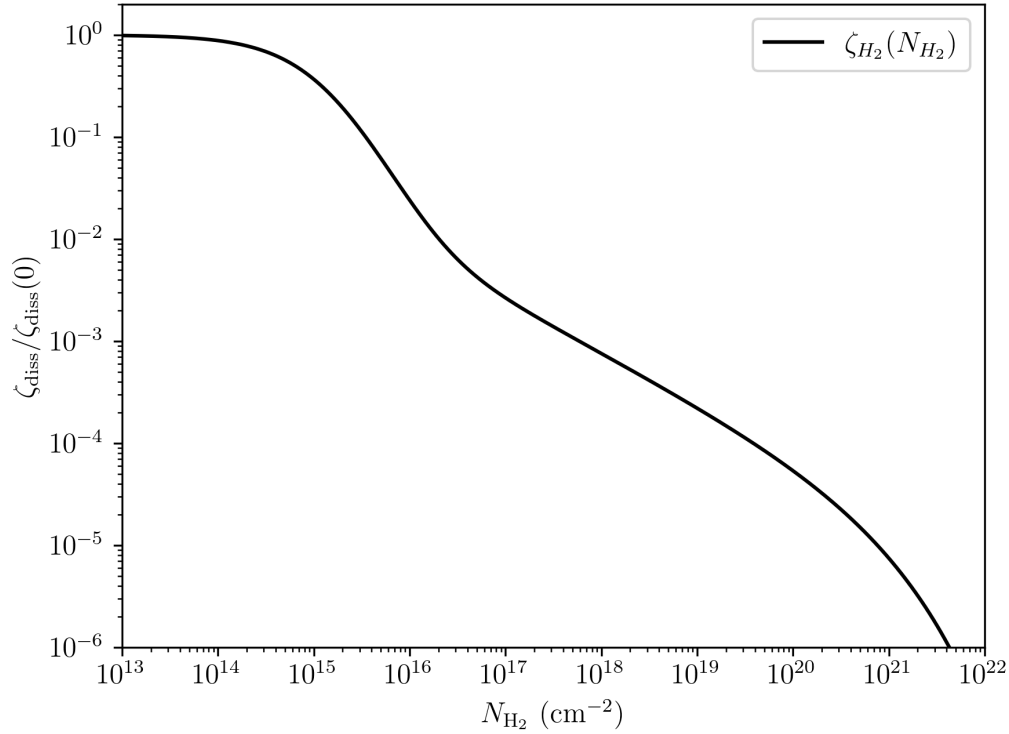
FIGURE 2.3: Plot of the Draine and Bertoldi (1996) shielding function from Equation 2.17. This fit shows the H_2 photodissociation rate ζ_{diss} as a function of column density of molecular hydrogen, N_{H_2}, relative to the unattenuated photodissociation rate at the source, $\zeta_{\text{diss}}(0)$.

Bertoldi (1996), and is presented here in Equation 2.18:

$$\zeta_{\text{diss}}(N_{H_2}) = f_{\text{shield}}(N_{H_2})e^{-\tau_{\text{dust}}}\zeta_{\text{diss}}(0) \tag{2.18}$$

where $\zeta_{\text{diss}}(0)$ is the incident photodissociation rate from the source, and $e^{-\tau_{\text{dust}}} = e^{-\sigma_{\text{dust}}N_H Z/Z_\odot}$ accounts for attenuation due to dust extinction. For dust attenuation, we use the total column of neutral and atomic hydrogen; $N_H = N_{HI} + 2N_{H_2}$. The assumption here is that dust is not present in regions of predominantly ionized hydrogen (HII) in the ISM, but this assumption is discussed further in Section 3.4.2.

In general, the shielding function exhibits a $\frac{1}{x^2}$ dependency at low N_{H_2}, and transitions to an $\frac{e^{-\sqrt{x}}}{\sqrt{x}}$ dependency at higher N_{H_2}. It should be noted that Equation 2.17 does not apply for arbitrarily large column densities either, as the $\frac{1}{x^2}$ behaviour takes over

for $N_{\mathrm{H_2}} > 10^{23}$ cm^{-2} even though the physical expectation is for the $\frac{e^{-\sqrt{x}}}{\sqrt{x}}$ behaviour to continue. Beyond $N_{\mathrm{H_2}} > 10^{23}$ cm^{-2}, the photodissociation rate does not drop off as quickly as expected. This behaviour is usually overlooked in the literature, likely because very few simulations reach a column density for H$_2$ in excess of 10^{23} cm^{-2}. Additionally, at such high column densities, the H$_2$ photodissociation rate is already smaller than 10^{-8} times the incident rate, so this feature is relatively insignificant.

Past attempts to incorporate shielding in galaxy simulations have estimated a column density $N_{\mathrm{H_2}}$ from the local properties of the gas using a Sobolev approximation (Baczynski et al. 2015; Kannan et al. 2020; Richings et al. 2022). This supposes that the column density at a single resolution element is proportional to a characteristic length L_{Sobolev}:

$$N_i \approx n_i L_{\mathrm{Sobolev}} \tag{2.19}$$

where n_i is the number density of that gas element. L_{Sobolev} is generally given by the ratio of the density of the resolution element to the gradient of density around that point (Gnedin et al. 2009):

$$L_{\mathrm{Sobolev}} = \frac{\rho}{|\nabla \rho|} \tag{2.20}$$

The main issue with a Sobolev-like approximation is that it makes the shielding entirely reliant on the local properties of the gas, when in practice shielding depends on the properties of the intervening material between the gas and the source of the radiation. Additionally, computing $\nabla \rho$ is based on some length scale, like inter-particle spacing, which is a resolution dependent property, not a physical property. This means that the Sobolev approximation is tied to resolution of the simulation, rather than a physical property of the cloud. Although we do not present any galaxy simulations in this thesis, we remove the need for a Sobolev length in this method by relying on column densities computed by ray tracing with the TREVR/TREVR2 radiative transfer scheme, which is discussed in more detail in Section 3.2.

Line Overlap

Although shielding reduces the photodissociation rate of H$_2$, the shielding function from Equation 2.17 only applies to the photodissociation rate, not the incoming flux. Photons are still absorbed when H$_2$ is dissociated, but up until a column density of about $N_{\mathrm{H_2}} \sim 10^{21}$ cm^{-2}, only the photons from the line centers are removed. So, shielding does not cause significant amounts of photons to be removed from the spectrum, but rather describes how the photons remaining in the spectrum are less effective at dissociation

as the radiation travels deeper through a cloud of H_2. However, at column densities $N_{H_2} > 10^{21}$ cm^2, the damping wings from individual lines in the Lyman-Werner band begin to overlap, blanketing the intensity across the entire band (Gnedin and Draine 2014). This process is referred to as line overlap. We attempt to fit line overlap as a function of N_{H_2} in Section 3.4.5.

2.3.3   15.2 - 24.6 eV band: ionizing H_2

While photons in the Lyman-Werner band are primarily responsible for the dissociation of H_2, photons with energies greater than 15.2 eV are capable of ionizing H_2. Photoionization of H_2 is the main process by which photons outside of the Lyman-Werner band are capable of destroying H_2, since H_2^+ dissociates by colliding with electrons on a relatively short timescale (Glover et al. 2006). Unlike the photodissociation cross section, the cross section for H_2 ionization is *not* line based, and therefore is not subject to shielding — any photon with an energy exceeding 15.2 eV can ionize H_2. The treatment of this method will follow the method outlined by Baczynski et al. (2015), and we detail the implementation of H_2 photoionization in Chapter 3.

2.3.4   The ultraviolet radiation background

The cosmic ultraviolet radiation background consists of radiation produced by massive stars in young galaxies, and maintains the ionized state of intergalactic gas (Haardt and Madau 1996). This background is based on empirically calibrated values by Haardt and Madau (2012). The metal cooling table used to parameterize cooling by metals in the GASOLINE chemical network is calibrated based on ionization states for intergalactic gas exposed to the Haardt and Madau (2012) background as a function of redshift. This metal table only strictly applies in regions where the gas is fully exposed to the UV background spectrum. In the dense ISM, this background is attenuated by intervening gas and dust, so the ionization state of metals in the ISM should be different, and would therefore require a different metal table. For the tests presented in Chapter 3, we use a high-redshift column of the metal cooling table to represent the more neutral ionization state expected in the ISM.

2.3.5   Cosmic ray ionization

Cosmic ray ionization is important for setting the trace HII and HI fractions at large column densities where the FUV radiation field has been attenuated (Kim et al. 2023). To compute the rate of cosmic ray ionization of H_2, we use the following formula from

Kim et al. (2023):

$$\zeta_{\mathrm{CR}} = 2\xi_{\mathrm{CR}}(2.3X_{\mathrm{H}_2} + 1.5X_{\mathrm{HI}}) \tag{2.21}$$

where ζ_{CR} is the cosmic ray ionization rate of H_2, ξ_{CR} is the cosmic ray ionization rate of HI, and X_{HI} and X_{H_2} are the gas mass fractions of HI and H_2 respectively. For all tests in this thesis, we use the benchmark cosmic ray ionization value from Röllig et al. (2007) as the cosmic ray ionization rate for HI:

$$\xi_{\mathrm{CR}} = 5 \times 10^{-17} \ \mathrm{s}^{-1} \tag{2.22}$$

Chapter 3

The Molecular Hydrogen Model

"If science were easy, I'd be out of a job."

Graduate student idiom

This chapter will discuss how the physical processes introduced in Chapter 2 were implemented to make a model for molecular hydrogen that is compatible with the GASOLINE code. These methods are presented alongside several tests of the implementation, which informed further development of the model.

3.1   Cooling in Gasoline

The GASOLINE code is predominantly used for simulations of galaxies. I am particularly interested in developing how the interstellar medium of galaxies is represented in GASOLINE. While the chemical network for molecular hydrogen presented in this thesis was developed with the constraints of the GASOLINE code in mind, these methods should be applicable to any simulation of the interstellar medium.

The chemistry integrator in GASOLINE is a non-equilibrium solver. Chemistry is solved by sub-cycling, where for a given hydrodynamic timestep, arbitrarily many substeps are taken to integrate the chemistry (Wadsley et al. 2017). This is necessary, as many of the equations that make up this network are stiff; the equations can vary rapidly, and the integration will become unstable unless a small timestep is used (Bovino and Galli 2019). This framework informs the development of many of our tests for molecular hydrogen: for any change in the radiation state which takes place over some timescale, the chemistry integrator from GASOLINE will integrate the chemistry using as many substeps as necessary to maintain stability.

GASOLINE is also designed to be highly modular, so that different parts of the code can be isolated for testing and development. This is important to mention, as tests we perform in this thesis mainly use the cooling code in isolation from the other GASOLINE modules such as gravity. This modularity also enables additional physics to be added to the code as technology develops or new methods become available. The initial publication of GASOLINE does not present methods for radiative transfer, but the current version of GASOLINE supports simulations of radiative transfer through recent developments in the TREVR algorithm (Grond et al. 2019; Wadsley et al. 2023). With the combination of smoothed particle hydrodynamics from GASOLINE and radiative transfer from TREVR, we can simulate how radiation couples to the gas of the ISM and interacts with the physics of molecular hydrogen.

3.2 The TREVR/TREVR2 Radiative Transfer Methods

Radiative transfer in astrophysics is a complex and computationally expensive problem. The full radiative transfer problem requires solving for the specific intensity I_ν at each point in space. In practice, this is a roughly 7-dimensional problem: I_ν varies at each point in space $\vec{r}$ (3 dimensions), varies with direction $\hat{n}$ (2 dimensions),[1] varies with frequency ν (1 dimension), and varies with time t (1 dimension) (Grond et al. 2019):

$$I_\nu(\vec{r}, \hat{n}, \nu, t) \tag{3.1}$$

A naive solution to this problem scales extremely poorly, incurring a computational expense on the order of the number of simulation elements raised to the power of $\frac{7}{3}$, $O(N^{\frac{7}{3}})$, which precludes any radiative transfer implementation in many astrophysical simulations (Grond et al. 2019).

There are, however, methods to reduce the computational cost of this problem. We are particularly interested in the Tree-based REVerse Ray Tracing TREVR method by Grond et al. (2019). TREVR uses the tree structure from the gravity solver to reduce the scaling of the radiative transfer problem. Recall from Section 1.3.1 that while the full solution for gravity scales as $O(N^2)$, the gravity tree reduces the scaling of this problem to $O(N \log N)$ (Barnes and Hut 1986). The original TREVR method aims to solve radiative transfer with $O(N \log N^2)$ scaling, which is slightly slower than $O(N \log N)$ gravity, but still manageable. TREVR is therefore most applicable when the environment being

---

[1]Since direction $\hat{n}$ is a unit vector, the length of $\hat{n}$ is always 1, so the components of $\hat{n}$ in two directions constrains the third. Hence, only two dimensions are needed to compute direction.

studied depends strongly on precise radiative transfer, but its $O(N \log N^2)$ scaling means that the radiation physics still demand long computational times. The more recent TREVR2 method is capable of reaching $O(N \log N)$ scaling, albeit at the cost of some accuracy (Wadsley et al. 2023). Since the TREVR2 method is on the same order of efficiency as gravity, radiative transfer can be be adopted in any simulation that is already solving gravity.

Both TREVR and TREVR2 are reverse ray tracing methods. Reverse ray tracing follows rays from receivers outwards to find all the sources that strike that resolution element (Grond et al. 2019). Ray tracing is necessary because the intensity received by each resolution element in a simulation depends on the properties of the intervening material between the source and the receiver. This treatment in particular is essential for our model of H_2, where the amount of dissociation depends on shielding, and shielding is governed by the column density of H_2 between the source and receiver (N_{H_2}), rather than the local properties of gas near the receiver. Moreover, shielding from multiple directions is not linear, so unlike other photo-destruction processes that scale as $e^{-\tau}$, shielding needs to be computed independently along each incoming ray. Ray tracing enables us to solve for N_{H_2} along each incoming ray to a source, thereby providing us with the means to model the contribution of multiple sources to H_2 dissociation without relying on approximations for N_{H_2} that are based on local quantities.

3.3 Radiation Bands

All radiation in the TREVR/TREVR2 method is divided into several distinct energy bands, each of which is based on the energies needed to ionize and dissociate the elements in our chemical network. The intensity of 12 specific frequencies are sampled from the radiation spectrum, generally corresponding to the upper and lower limits of key ionization thresholds. The shape of the spectrum between these points is then fit with a power law to connect the upper and lower band edges, which enables us to capture the effects of radiation hardening at increasing optical depths (Baumschlager et al. 2023). Generally, the cross section for ionization is highest at the threshold energy, and decreases as photons become more energetic. So, radiation is predominantly removed from the lower band edge before the upper band edge. This makes the remaining radiation increasingly *hard*, as it penetrates deeper into the cloud with lower cross section. The effects of radiation hardening can be seen in Figure 3.1, alongside the limits of the radiation bands used in TREVR2.
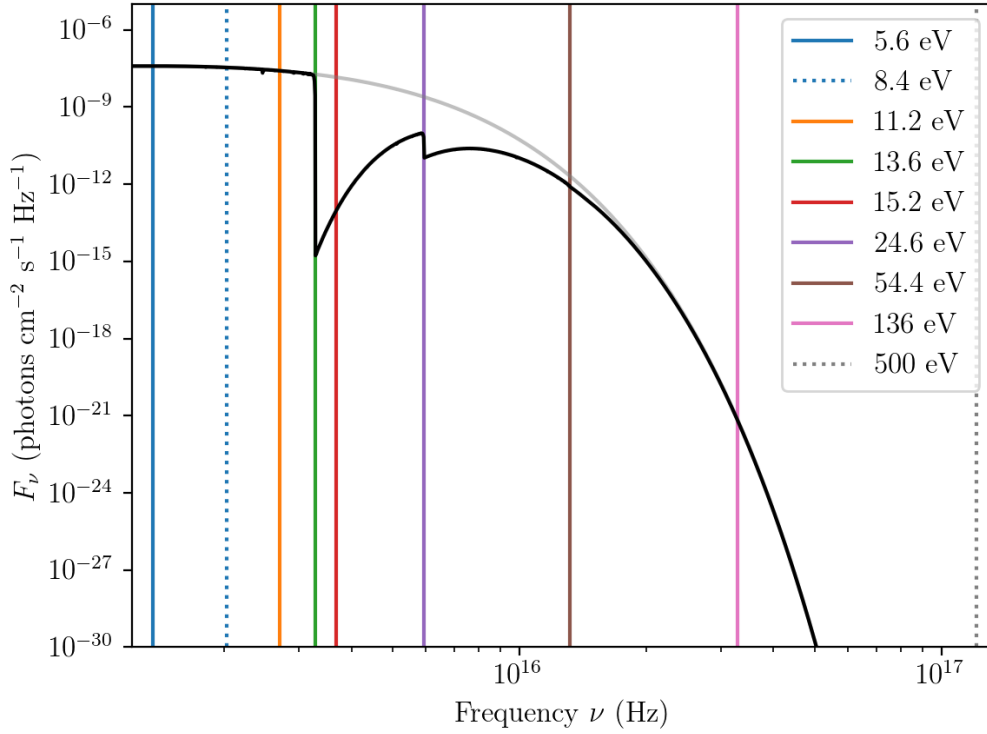
FIGURE 3.1: Limits of the radiation bands used in the TREVR2 multi-band method, plotted over a CLOUDY spectrum at a depth of $N_\mathrm{H} = 3.6 \times 10^{18}$ cm^{-2} to show the effects of radiation hardening. The solid black line shows the CLOUDY spectrum at $N_\mathrm{H} = 3.6 \times 10^{18}$ cm^{-2} into an HII region, while the grey line shows the incident spectrum. The dotted lines indicate the location of bands that are captured with a single average value, rather than integration over the whole band.

3.3.1 Far-Ultraviolet (8.4 eV)

Only one averaged value is used for this entire band. Since there are no species in our network that are ionized by far-ultraviolet (FUV) photons, the shape of the radiation spectrum in this band is unlikely to change with depth, so capturing radiation hardening is not important. The primary purpose of this band is to compute photoelectric heating; dust is currently the only contributor to the absorption of FUV photons.

3.3.2   Lyman-Werner (11.2 eV - 13.6 eV)

The two values for this band originally represented the upper and lower band edges. However, radiation in the Lyman-Werner (LW) band does not harden in the same manner as the other bands. Instead, radiation in the LW band becomes less effective at dissociating H_2 due to H_2 self-shielding, as outlined in Section 2.3.2. Computing an upper and lower flux value for this band does not yield any useful information. Rather, we use one of the two LW bins to compute the attenuation of radiation due to dust only, much like in the FUV band. This first intensity is used to compute the contribution of Lyman-Werner photons to photoelectric heating. The second Lyman-Werner bin is used to compute the photodissociation rate of H_2, tracking shielding of LW radiation alongside dust attenuation. We cannot apply the shielding function directly to the intensity, since the shielding function is not itself an opacity but simply a fit to the photodissociation rate of H_2 as a function of depth. So, this second band is used to explicitly track the photodissociation rate of H_2. If we need a physical intensity for the Lyman-Werner band, we simply use the bin that is only affected by dust attenuation. In the future, we hope to implement both dust attenuation and absorption by H_2 radiation into this bin, and we propose a potential method for capturing the effect of H_2 opacity on this flux in Section 3.4.5.

3.3.3   Hydrogen-ionizing (13.6 eV - 15.2 eV)

Every bin with energy greater than 13.6 eV contributes to the ionization of atomic Hydrogen. The first Hydrogen-ionizing bin originally captured all photons with energies 13.6 eV to 24.6 eV, but this bin was split by the addition of H_2 photoionization physics, which required another bin to be inserted in this range. So, the Hydrogen-ionizing bin now only covers the smaller range of 13.6 eV to 15.2 eV.

3.3.4 H_2-ionizing (15.2 eV - 24.6 eV)

This bin covers photons with energies ranging from 15.2 eV to 24.6 eV. The HI ionization cross section continues through this bin without interruption. Meanwhile, the shape of the H_2 cross section deviates from the typical power-law shape at the low end of this band, but adopts a power law shape starting at 18.10 eV. The shape of the H_2 ionization cross section is discussed further in Section 3.4.3.

3.3.5   Helium-ionizing and higher bands (> 24.6 eV)

All remaining bands cover the ionization of HeI (24.6 eV - 54.4 eV), HeII (54.4 eV - 136 eV), and very hard, high energy photons (136 eV - 500 eV). Ionization cross sections for HI and H_2 persist through all of these bands, although the cross section for ionization at these energies is rather small.

3.4   Implementing Molecular Hydrogen Photochemistry

3.4.1   Dissociation and shielding in the Lyman-Werner band

The shielding function f_{shield} from Equation 2.17 is a fit to the photodissociation rate as a function of N_{H_2} relative to the unshielded, unattenuated photodissociation rate $\zeta_{H_2}(0)$. It therefore captures all effects of radiation hardening and opacity on the H_2 photodissociation rate. When computing the photodissociation of H_2, we should not model the effects of opacity on the Lyman-Werner band; not only are these behaviours are already fit via the shielding function, but since the effective opacity of the Lyman-Werner band is set by the line based cross section of H_2, LW opacity exhibits a different behaviour with depth than other bands. Instead, we use Equation 40 from Draine and Bertoldi (1996) to approximate H_2 dissociation as a function of the H_2 column density. This equation was presented previously as Equation 2.18, but we repeat it here for convenience:

$$\zeta_{\text{diss}}(N_{H_2}) = f_{\text{shield}}(N_{H_2})e^{-\tau_{\text{dust}}}\zeta_{\text{diss}}(0) \tag{3.2}$$

where $f_{\text{shield}}(N_{H_2})$ is the shielding function given by Equation 2.17, ζ_{diss} is the dissociation rate of H_2, $\zeta_{\text{diss}}(0)$ is the photodissociation rate at the source, and $e^{-\tau_{\text{dust}}}$ is the contribution from dust opacity to shielding LW radiation. Figure 3.2 illustrates the difference between the H_2 photodissociation rate as a function of depth using Equation 3.2 to the $e^{-\tau} = e^{-\sigma_{H_2}N_{H_2}}$ behaviour that is typically exhibited by other species in our network. In Section 3.9, we detail how the shielding function is handled in a radiative transfer simulation.

It is worth nothing that the photodissociation cross section extends *above* 13.6 eV, which can be seen in the Heays et al. (2017) cross section data. This implies that H_2 can be dissociated by photons with $h\nu > 13.6$ eV, however we choose not to model this process. The practical reason for this choice is that it is unclear how shielding should be applied to the same flux that ionizes HI. A new shielding function would need to be calibrated which reduces the effectiveness of H_2 dissociation without reducing the amount of HI that can be ionized. Our justification for ignoring this process is
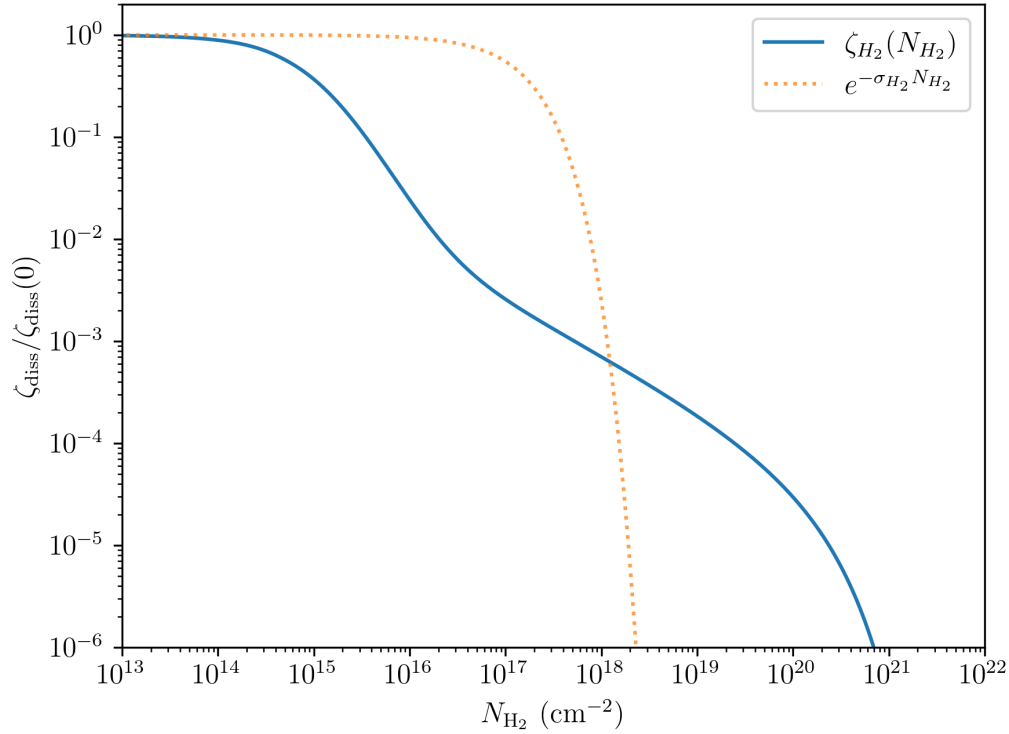
FIGURE 3.2: The photodissociation of H_2 as a function of depth using Equation 3.2 (blue line) compared to the $e^{-\tau}$ shape that typically follows from ionization as a function of depth (dotted orange line). This comparison illustrates why photodissociation of H_2 requires a separate treatment from photoionization of other species in our network, which typically follow an $e^{-\tau}$ behaviour. The $e^{-\tau}$ function exhibits a much higher photodissociation rate at moderate column densities, until $N_{H_2} \sim (\sigma_{H_2})^{-1} \approx 1.67 \times 10^{17}$ cm^{-2}, at which point the $e^{-\tau}$ behaviour takes over, and the photodissociation rate plummets. At very high column densities, there would be no persistent photodissociation of H_2, whereas with shielding we expect some photodissociation to persist at depths $N_{H_2} > 10^{19.5}$ cm^{-2}.

that there should always be some trace HI fraction that can absorb this radiation more effectively than H_2 can. In practice, photodissociation regions are typically surrounded by HII regions, which ensure that this ionizing flux is absorbed or reprocessed before reaching the molecular gas. Additionally, a scenario where a molecular cloud is *only* exposed to radiation in the range of 13.6 eV to 15.2 eV is physically unlikely, especially given that σ_{HI} provides one of the largest sources of opacity in our radiative transfer routines, and reaches a maximum value at 13.6 eV. Still, if a molecular cloud under our

model were to be irradiated exclusively by photons in this range, the cloud would remain molecular, and the trace H$_\text{I}$ fraction would be replaced by a trace H$_\text{II}$ fraction until all the ionizing photons had been absorbed. Generally this behaviour is not physical, and while accounting for this process may be necessary moving forward, this scenario did not appear in any tests we have performed so far.

3.4.2 Dust Opacity

Dust opacity provides the primary method for attenuating FUV flux and for suppressing Lyman-Werner flux at very high column densities. Equation 3.3 is used for both the FUV band and the Lyman-Werner band:

$$e^{-\tau_{1000}Z/Z_\odot} = e^{-\sigma_\text{dust}N_\text{H}Z/Z_\odot} = e^{-\sigma_\text{dust}(N_\text{HI}+2N_{\text{H}_2})Z/Z_\odot} \tag{3.3}$$

where σ_dust is the cross section for absorption by dust, N_H is the column density of hydrogen, and $Z/Z_\odot$ is the metallicity of the gas relative to the solar metallicity. This expression assumes that the amount of dust present in a cloud is directly proportional to metallicity. We use a constant value for dust opacity based on the opacity of solar metallicity dust at 1000 Angstroms, computed from the Röllig et al. (2007) model parameters:

$$\kappa_\text{dust} = 1137 \text{ cm}^2\text{g}^{-1} \tag{3.4}$$

which corresponds to a dust absorption cross section of:

$$\sigma_\text{dust} = 1.899 \times 10^{-21} \text{ cm}^2 \tag{3.5}$$

We note that Draine and Bertoldi (1996) use a dust cross section of $\sigma_\text{dust} = 2 \times 10^{-21}$ cm^{-2}, 5% larger than our adopted value.

For the column density in Equation 3.3, we choose $N_\text{H} = N_\text{HI} + 2N_{\text{H}_2}$. This assumes that dust is present in any neutral gas, but not in ionized gas, and is somewhat contrary to the choice made by Draine and Bertoldi (1996), who use the total column density of hydrogen, $N_\text{H} = N_\text{HI} + 2N_{\text{H}_2} + N_\text{HII}$. Accounting for the column density of ionized hydrogen may be sensible when modeling an H$_\text{II}$ region, as the presence of dust in H$_\text{II}$ regions can be inferred by scattering (Tielens 2005), and dust grains in H$_\text{II}$ regions can absorb and reprocess ionizing radiation (Kim et al. 2016). However, none of the H$_\text{II}$ regions simulated in this thesis have column densities larger than $N_\text{HII} \sim 10^{19}$ cm^{-2}, which is much smaller than the column density $N_\text{H} > 5\times10^{20}$ cm^{-2} that would be needed for dust opacity to significantly reduce the intensity of radiation transmitted through

an H$_{\text{II}}$ region, so our choice to exclude N_{HII} from the total column density N_{H} should not influence our simulated PDRs. It is not sensible for dust to be present alongside H$_{\text{II}}$ in other phases of the ISM, since dust in the warm/hot ionized medium is typically destroyed by shocks or collisions with other dust grains (Tielens 2005). Dust may exist for several Mpc outside of the galaxy where temperatures exceed $T > 10^6$ K and gas is highly ionized, so more detailed examinations of these assumptions are warranted (Ménard et al. 2010).

3.4.3 Photoionization of H$_2$

Photoionization of H$_2$ is the primary process by which photons outside of the Lyman-Werner band can destroy H$_2$ molecules. Although these photons do not dissociate H$_2$ directly, the H$_2$ anion H$_2^+$ can be readily destroyed by dissociative recombination with free electrons in the gas (H$_2^+$ + e$^-$ → 2H$_{\text{I}}$) (Baczynski et al. 2015). To account for photoionization of molecular hydrogen, we follow a similar prescription to the FERVENT code, as outlined in Baczynski et al. (2015). H$_2$ can be photoionized by photons with energies $h\nu > 15.2$ eV. The shape of the H$_2$ photoionization cross section is shown in Figure 3.3, and is fit based on work by Liu and Shemansky (2012). We fit the photoionization cross section for H$_2$ using a piece-wise step function from 15.2 eV to 18.1 eV, followed by a power law of

$$\sigma_{\text{H}_2} = 9.75 \times 10^{-18} \left(\frac{\nu_{18.10}}{\nu} \right)^3 \tag{3.6}$$

for energies $h\nu > 18.1$ eV, where $\nu_{18.10}$ is the frequency of photons with an energy of 18.10 eV (Baczynski et al. 2015).

In Section 3.4.1, we assumed that modeling direct photodissociation of H$_2$ by H$_{\text{I}}$ ionizing photons ($h\nu > 13.6$ eV) is unnecessary because this radiation will have already been absorbed in the ionization of H$_{\text{I}}$. H$_2$ is photoionized by photons with energies $h\nu > 15.2$ eV, which can also be readily absorbed by H$_{\text{I}}$. We still choose to model this process because the photoionization cross section for H$_2$ is actually *larger* than that of H$_{\text{I}}$ at energies near to 15.2 eV (see Figure 3.3). If a molecular cloud with trace H$_{\text{I}}$ is exposed to H$_{\text{I}}$ ionizing radiation, then the H$_2$ will actually be more capable of absorbing this radiation than the atomic hydrogen. It should be noted that this power law fit for the H$_2$ ionization cross section σ_{H_2} decreases more steeply than the H$_{\text{I}}$ cross section σ_{HI}, so while H$_2$ photoionization can absorb more photons at lower energies, H$_{\text{I}}$ ionization is more capable of removing higher energy photons.
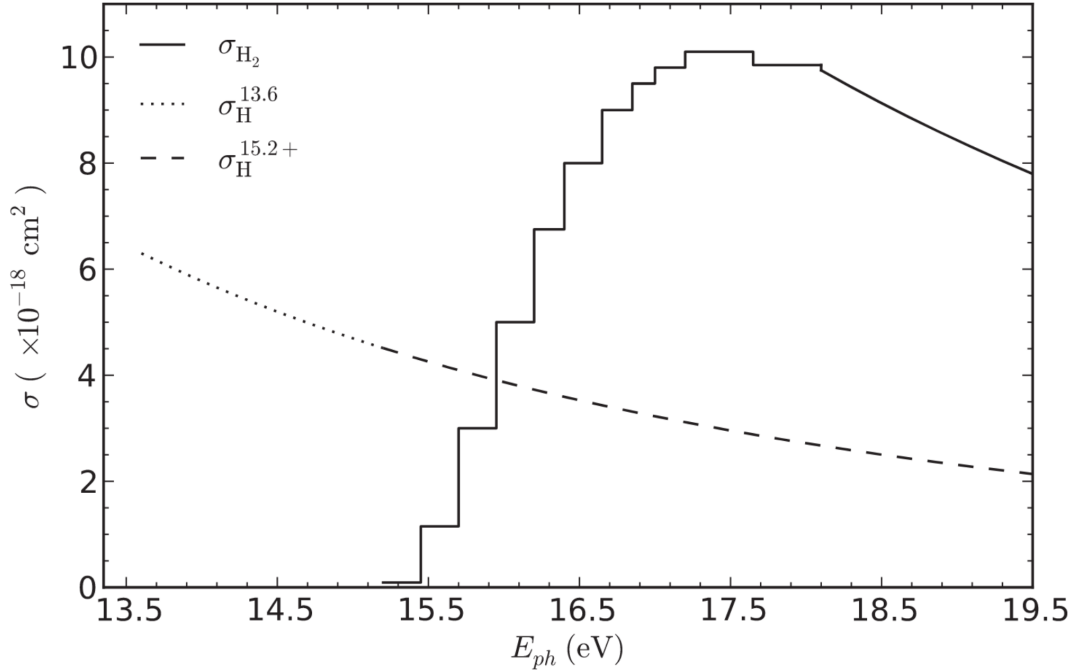
FIGURE 3.3: Reproduction of Figure 1 from Baczynski et al. (2015) comparing the cross section for photoionization of molecular hydrogen (solid line) to the photoionization cross section of atomic hydrogen (dotted and dashed lines). The H_2 photoionization cross section follows a piece-wise step function for photons with energies in the range of 15.2 eV to 18.1 eV. This transitions to a power law for energies above 18.1 eV.

Baczynski et al. (2015) find that radiation in the range 13.6 eV to 15.2 eV cannot be absorbed by fully molecular gas, which can create a scenario where photons with energies greater than 15.2 eV ionize H_2 to create HI, but too late in their method for this HI to absorb the lower energy radiation (13.6 eV $< h\nu <$ 15.2 eV). To remedy this issue, the authors compute the 15.2 eV photoionization of H_2 *before* the 13.6+ eV ionization of HI.

Deriving photoionization from power-law cross section fits

While photodissociation of H_2 is complicated by shielding and requires special treatment to implement as outlined in Section 3.4.1, the photoionization of H_2 can be treated in the same manner as the ionization of any other hydrogen or helium species. Here, I outline the method used to derive the H_2 photoionization rate given an incident radiation spectrum.

The radiative transfer code provides a radiation spectrum divided into bins, or radiation bands (see Section 3.3). A power law is used to fit the shape of the spectrum connecting the two ends of these bands. To derive the photoionization rate (ξ_i) for a species i in a certain band that ranges in frequency from ν_1 to ν_2, we need to integrate the product of intensity (equivalently flux F_ν for this derivation) and cross section of that species (σ_ν) as a function of the frequency. For the shape of the spectrum in the band, we assume the left edge of the band is connected to the right edge of the band by a power law:

$$F_\nu = F_j \nu^\alpha \tag{3.7}$$

where $\alpha = \frac{\ln(F_2/F_1)}{\ln(\nu_2/\nu_1)}$ and $F_j = \frac{F_1}{\nu_1^\alpha}$. Here, F_1 and F_2 are the intensities at the lower and upper edges of the band respectively, and F_j calibrates our power law so that $F_{\nu_1} = F_1$ at the lower band edge, and $F_{\nu_2} = F_2$ at the upper band edge.

The cross section for photoionization, σ_ν is typically fit with a power law

$$\sigma_\nu = \sigma_0 \nu^a (b\nu + c) \tag{3.8}$$

where σ_0 is the cross section at the lower band edge, and a, b, and c are constants.

With the spectral shape established and our cross section in hand, we may begin the derivation of the photoionization rate:

$$
\begin{aligned}
\xi_i &= \int_{\nu_1}^{\nu_2} F_\nu \sigma_\nu d\nu \\
&= \int_{\nu_1}^{\nu_2} F_j \nu^\alpha \sigma_\nu d\nu \\
&= \int_{\nu_1}^{\nu_2} F_j \nu^\alpha (\sigma_0 \nu^a (b\nu + c)) d\nu \\
&= F_j \sigma_0 \int_{\nu_1}^{\nu_2} \nu^\alpha (b\nu^{a+1} + c\nu^a) d\nu \\
&= F_j \sigma_0 \int_{\nu_1}^{\nu_2} b\nu^{\alpha+a+1} + c\nu^{\alpha+a} d\nu \\
&= F_j \sigma_0 \left[\frac{b}{\alpha+a+2} \nu^{\alpha+a+2} + \frac{c}{\alpha+a+1} \nu^{\alpha+a+1} \right]_{\nu_1}^{\nu_2} \\
&= F_j \sigma_0 \left(\frac{b}{\alpha+a+2} \left(\nu_2^{\alpha+a+2} - \nu_1^{\alpha+a+2} \right) + \frac{c}{\alpha+a+1} \left(\nu_2^{\alpha+a+1} - \nu_1^{\alpha+a+1} \right) \right)
\end{aligned}
$$

Then, we make the substitution $F_j = \frac{F_1}{\nu_1^\alpha}$:

$$= \frac{F_1\sigma_0}{\nu_1^\alpha}\left(\frac{b}{\alpha+a+2}\left(\nu_2^{\alpha+a+2} - \nu_1^{\alpha+a+2}\right) + \frac{c}{\alpha+a+1}\left(\nu_2^{\alpha+a+1} - \nu_1^{\alpha+a+1}\right)\right)$$

and multiply through by $\frac{\nu_1^a}{\nu_1^a}$ so that we can simplify this computation...

$$= F_1\sigma_0\frac{\nu_1^a}{\nu_1^{\alpha+a+1}}\left(\frac{b}{\alpha+a+2}\left(\nu_2^{\alpha+a+2} - \nu_1^{\alpha+a+2}\right) + \frac{c}{\alpha+a+1}\left(\nu_2^{\alpha+a+1} - \nu_1^{\alpha+a+1}\right)\right)$$

$$= F_1\sigma_0\nu_1^a\left(\frac{1}{\nu_1^{\alpha+a+1}}\frac{b}{\alpha+a+2}\left(\nu_2^{\alpha+a+2} - \nu_1^{\alpha+a+2}\right) + \frac{1}{\nu_1^{\alpha+a+1}}\frac{c}{\alpha+a+1}\left(\nu_2^{\alpha+a+1} - \nu_1^{\alpha+a+1}\right)\right)$$

$$= F_1\sigma_0\nu_1^a\left(\frac{\nu_1}{\nu_1^{\alpha+a+2}}\frac{b}{\alpha+a+2}\left(\nu_2^{\alpha+a+2} - \nu_1^{\alpha+a+2}\right) + \frac{1}{\nu_1^{\alpha+a+1}}\frac{c}{\alpha+a+1}\left(\nu_2^{\alpha+a+1} - \nu_1^{\alpha+a+1}\right)\right)$$

$$= F_1\sigma_0\nu_1^a\left(\frac{b\nu_1}{\alpha+a+2}\left(\frac{\nu_2^{\alpha+a+2}}{\nu_1^{\alpha+a+2}} - \frac{\nu_1^{\alpha+a+2}}{\nu_1^{\alpha+a+2}}\right) + \frac{c}{\alpha+a+1}\left(\frac{\nu_2^{\alpha+a+1}}{\nu_1^{\alpha+a+1}} - \frac{\nu_1^{\alpha+a+1}}{\nu_1^{\alpha+a+1}}\right)\right)$$

$$= F_1\sigma_0\nu_1^a\left(\frac{b\nu_1}{\alpha+a+2}\left(\left(\frac{\nu_2}{\nu_1}\right)^{\alpha+a+2} - 1\right) + \frac{c}{\alpha+a+1}\left(\left(\frac{\nu_2}{\nu_1}\right)^{\alpha+a+1} - 1\right)\right)$$

Therefore, our H_2 photoionization rate is given by the following formula:

$$\xi_i = F_1\sigma_0\nu_1^a\left(\frac{b\nu_1}{\alpha+a+2}\left(\left(\frac{\nu_2}{\nu_1}\right)^{\alpha+a+2} - 1\right) + \frac{c}{\alpha+a+1}\left(\left(\frac{\nu_2}{\nu_1}\right)^{\alpha+a+1} - 1\right)\right) \quad (3.9)$$

where a, b, and c make the power law fit to the cross section data.

Deriving heating rate due to photoionization

Normally the energy released (heating) per ionization depends on the amount of excess energy left over after photoionization takes place. In the case of HI, any photon with energy greater than ionization threshold of 13.6 eV can ionize HI, and any remaining energy that photon carries is given to the ionized electron, which transfers that energy to the surrounding gas collisionally. So, the amount of energy released when a photon of energy $h\nu$ ionizes a Hydrogen atom is $(h\nu - 13.6)$ eV. For molecular hydrogen, the process is similar, although the ionization threshold for H_2 is $E_{\text{th}} = 15.2$ eV, so the amount of energy deposited when a photon ionizes H_2 is $\Delta E = (h\nu - 15.2)$ eV.

The equation for the rate of heating per ionization (Γ_i) is very similar to the ionization rate equation, but since the amount of energy released depends on the energy of the incoming photon, the photoheating equation has and additional frequency dependency

(Osterbrock 1989):

$$\Gamma_i = \int_{\nu_1}^{\nu_2} F_\nu h(\nu - \nu_{\text{th}})\sigma_\nu d\nu \tag{3.10}$$

where h is Planck's constant and ν_{th} is the frequency corresponding to the threshold energy E_{th} needed to ionize the species i. The derivation for this formula is very similar to the derivation outlined above for photoionization, so I will only present the final result:

$$\Gamma_i = h\nu_1^2\sigma_0\left(\frac{b}{\alpha + a + 3}\left(F_2\left(\frac{\nu_2}{\nu_1}\right)^{\alpha+a+3} - F_1\right) + \frac{c}{\alpha + a + 2}\left(F_2\left(\frac{\nu_2}{\nu_1}\right)^{\alpha+a+2} - F_1\right)\right)$$
$$- E_{\text{th}}\xi_i \tag{3.11}$$

Equation 3.11 applies for the heating per photoionization of H_2, but this formula cannot be used for the heating per *photodissociation* of H_2 because the dissociation cross section is line-based and cannot be not fit by a power law. Instead, the an approximation from Appendix A4 of Gnedin and Kravtsov (2011) is used, which takes the average heating per photodissociation of H_2 to be 0.4 eV. The heating per photodissociation of H_2 is given by Equation 3.12:

$$\Gamma_{H_2} = 0.4\text{eV} \times \zeta_{H_2} \tag{3.12}$$

3.4.4 Photoelectric Heating

For the total photoelectric heating rate, we use the expression given by equation 3.17 in Tielens (2005):

$$n\Gamma_{\text{PE}} = 10^{-24}\epsilon n G_0 \text{ erg cm}^{-3} \text{ s}^{-1} \tag{3.13}$$

where ϵ is the photoelectric heating efficiency, n is the number density of the gas, and G_0 is the strength of FUV radiation relative to the integrated intensity of the Habing field (Habing 1968). The Habing field characterises the intensity of FUV interstellar radiation in the solar neighborhood. In this context, FUV refers to all radiation with $E_\gamma < 13.6$ eV, so in our implementation this includes both the FUV band and the LW band. The photoelectric heating efficiency is given by equation 3.16 in Tielens (2005):

$$\epsilon = \frac{4.87 \times 10^{-2}}{1 + 4 \times 10^{-3}\gamma^{0.73}} + \frac{3.65 \times 10^{-2}(T/10^4)^{0.7}}{1 + 2 \times 10^{-4}\gamma} \tag{3.14}$$

where γ is the charging parameter, which represents the degree to which dust grains and PAHs[2] are charged, and is roughly proportional to the ratio of ionization rate to

---

[2]Polycyclic Aromatic Hydrocarbons, planar molecules in the ISM that provide a source of electrons for photoelectric heating similar to dust grains.

recombination rate. The charging parameter is given by the following expression from Tielens (2005):

$$\gamma = G_0 T^{1/2}/n_e \tag{3.15}$$

The photoelectric heating efficiency ϵ varies from roughly 5% in regions of low ionization ($\gamma \ll 10^3$ K$^{1/2}$ cm^3) to 1% in the warm neutral medium, and is lowest in dense PDRs where $\epsilon \sim 0.3\%$ ($\gamma \approx 10^5$ K$^{1/2}$ cm^3) (Tielens 2005).

The unit value for the integrated Habing field is 1.6×10^{-3} erg cm^{-2} s^{-1}, so that flux relative to the Habing field is $G_0 = \frac{F}{1.6 \times 10^{-3}}$ (Habing (1968), see also Draine and Bertoldi 1996)

The factor G_0 that I employ in the code is defined as follows:

$$G_0 = 18226 \frac{J_{\text{FUV}}}{4\pi(1.2 \times 10^{-4})} \tag{3.16}$$

where the factor of 18226 is needed to convert from mean intensity of the FUV band J_{FUV} (in photons cm^{-2} s^{-1} Hz^{-1}) to flux (in erg cm^{-2} s^{-1}) as follows:

$$\begin{aligned}
F_{\text{FUV}} &= \int_{5.6 \text{ eV}}^{11.2 \text{ eV}} J_{\text{FUV}} h\nu \, d\nu \\
&= \left[J_{\text{FUV}} \frac{h\nu^2}{2} \right]_{5.6/h \text{ Hz}}^{11.2/h \text{ Hz}} \\
&= \frac{h}{2} J_{\text{FUV}} [(11.2/h)^2 - (5.6/h)^2] \\
&= 18226 \text{ erg Hz photon}^{-1} J_{\text{FUV}}
\end{aligned}$$

To obtain the strength of the Habing field, we need to integrate over both the FUV radiation band (5.4 eV to 11.2 eV) and the LW radiation band (11.2 eV to 13.6 eV). Currently, the only process associated with FUV photons is the photoelectric effect, so treatment of this band is relatively straightforward, with radiation attenuated by a single $e^{-\tau_{\text{dust}}}$ parameter. Meanwhile, LW photons are both attenuated by dust and absorbed by H$_2$ dissociation. We therefore calculate two LW bands in our code, as outlined in Section 3.3.2, one of which tracks the intensity of the LW band to be used when computing the strength of the Habing field. In Section 3.4.5, we devise a method to properly compute absorption by H$_2$ on the averaged intensity across the Lyman-Werner band, which should enable us to correctly estimate the amount of Lyman-Werner flux that contributes to photoelectric heating.

3.4.5   Fit to the Lyman-Werner absorption
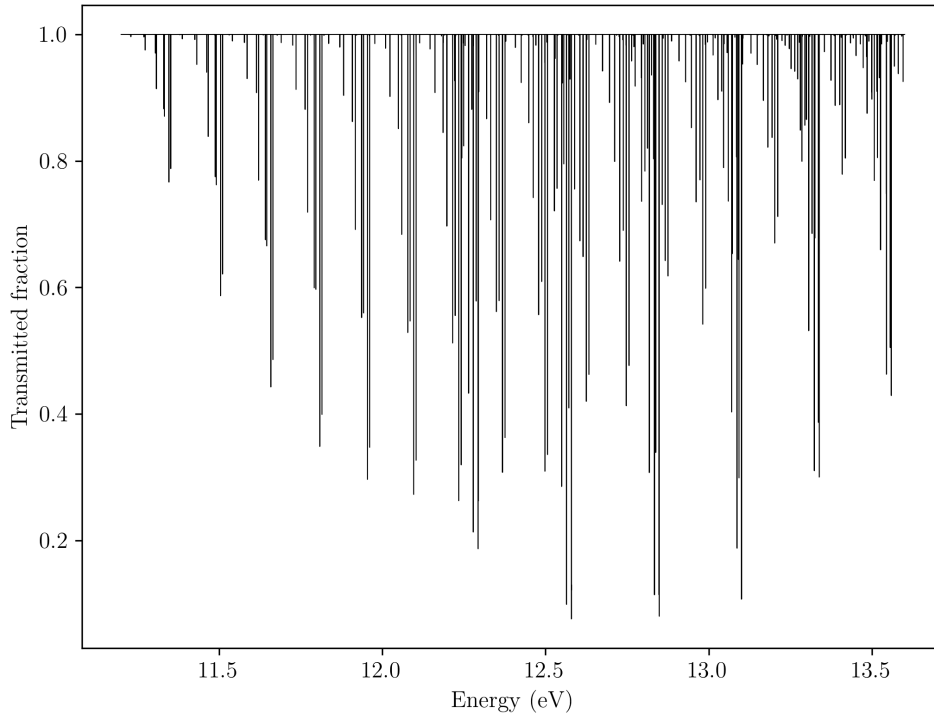
FIGURE 3.4: Lyman-Werner spectrum at $N_{\mathrm{H_2}} = 10^{14}$ cm^{-2}. At this relatively shallow depth, only photons in the line centers are removed from the spectrum. 99.8% of photons make it to this depth, with only 0.2% being absorbed by $\mathrm{H_2}$.

Here, I devise a method to estimate the average flux of the Lyman-Werner band as a function of depth. This enables us to capture the effect of the line-based structure of the $\mathrm{H_2}$ cross section on the absorption of Lyman-Werner photons, without actually having to simulate each individual line in the spectrum. Due to time constraints of the project, I have not been able to test this implementation, but I will briefly present the methods and functional fit.

Conceptually, this work bears some similarities the Draine and Bertoldi (1996) shielding function. Using data for the photoabsorption cross section (σ_ν) of $\mathrm{H_2}$ from Heays et al. (2017), I compute the fraction of flux that is transmitted through a given column density of gas, $N_{\mathrm{H_2}}$, by calculating $e^{-\sigma_\nu N_{\mathrm{H_2}}}$ at each frequency ν in the Lyman-Werner
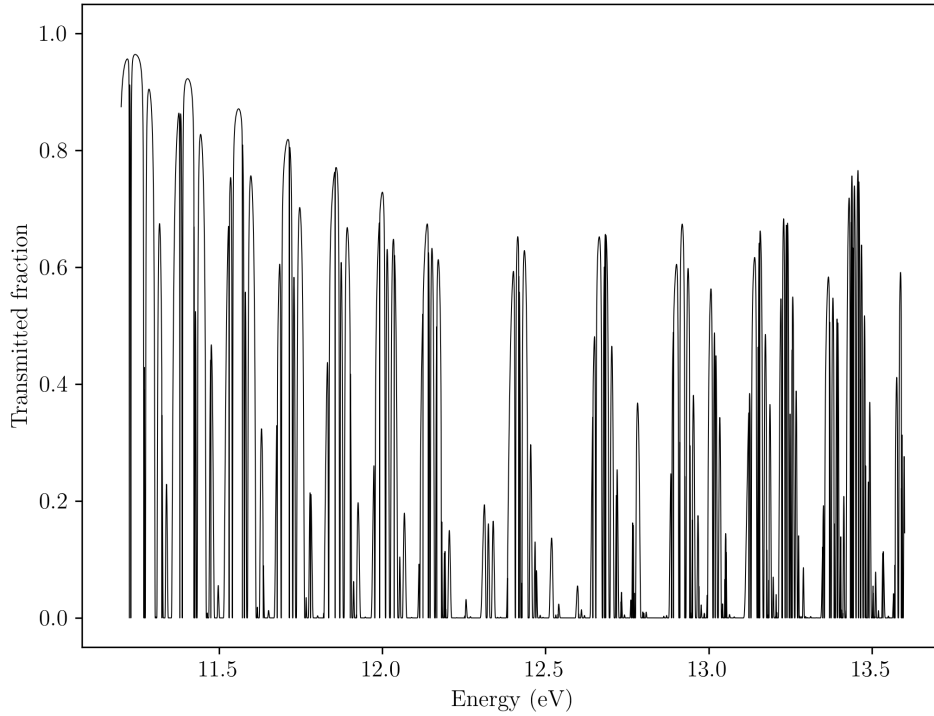
FIGURE 3.5: Lyman-Werner spectrum at $N_{H_2} = 10^{21}$ cm^{-2}. This is relatively deep into the cloud, where the line centers are optically thick and only photons in the line wings still contribute to H_2 dissociation. Overlap of the line wings is the strongest contributor to the overall absorption of Lyman-Werner photons (Gnedin and Draine 2014). Only 25.4% of photons make it to this depth; 74.6% of all incident photons have been absorbed by H_2.

band and then integrating over the spectrum:

$$f_{\text{transmitted}}(N_{H_2}) = \frac{\int_{\nu_1}^{\nu_2} e^{-\sigma_\nu N_{H_2}} \, d\nu}{\int_{\nu_1}^{\nu_2} d\nu} \tag{3.17}$$

The transmitted fraction is equivalent to the area under the Lyman-Werner spectrum. Comparing Figure 3.4 to Figure 3.5 illustrates this behaviour, as each shows the Lyman-Werner spectrum at column densities $N_{H_2} = 10^{14}$ cm^{-2} and $N_{H_2} = 10^{21}$ cm^{-2} respectively. Note that this transmitted fraction purely considers the H_2 contribution to absorption, and excludes the contribution from dust opacity. Absorption from dust depends on the metallicity of the gas, and is accounted for separately as per the usual
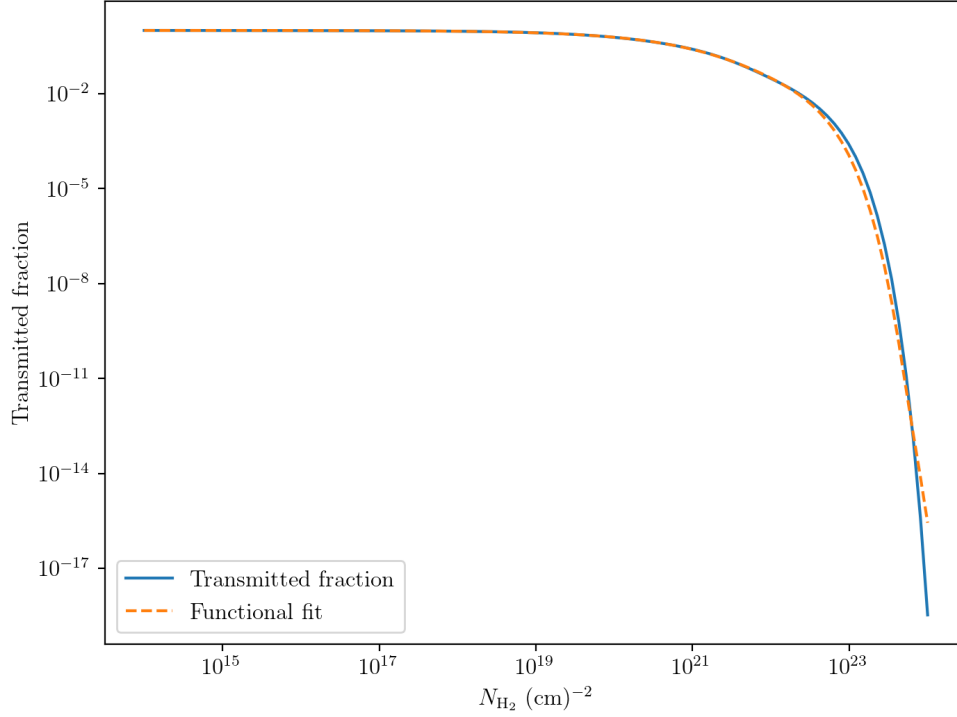
FIGURE 3.6: Fit to the fraction of Lyman-Werner flux that is transmitted up to a column density of N_{H_2}.

method outlined in Section 3.4.2.

The transmitted fraction of flux averaged over the Lyman-Werner band as a function of column density is shown in Figure 3.6. Equation 3.18 is used to fit the transmitted fraction as a function of column density:

$$f_{\text{transmitted}}(N_{H_2}) = 0.95 e^{-3.8 \times 10^{-10} N_{H_2}{}^{0.4572}} + 0.05 e^{-1.779 \times 10^{-18} N_{H_2}{}^{0.8061}} \qquad (3.18)$$

so that the intensity averaged over the Lyman-Werner band (I_{LW}) can be represented as:

$$I_{\text{LW}}(N_{H_2}) = f_{\text{transmitted}}(N_{H_2}) e^{-\tau_{\text{dust}}} I_{\text{LW}}(0) \qquad (3.19)$$

This bears a similar form to the photodissociation rate $\zeta_{H_2}(N_{H_2})$ from Equation 3.2, and since the column density N_{H_2} must already be computed to solve for the photodissociation of H_2, we can simply save the value of N_{H_2} and apply it to compute the physical

intensity averaged over the Lyman-Werner band using Equations 3.18 and 3.19.
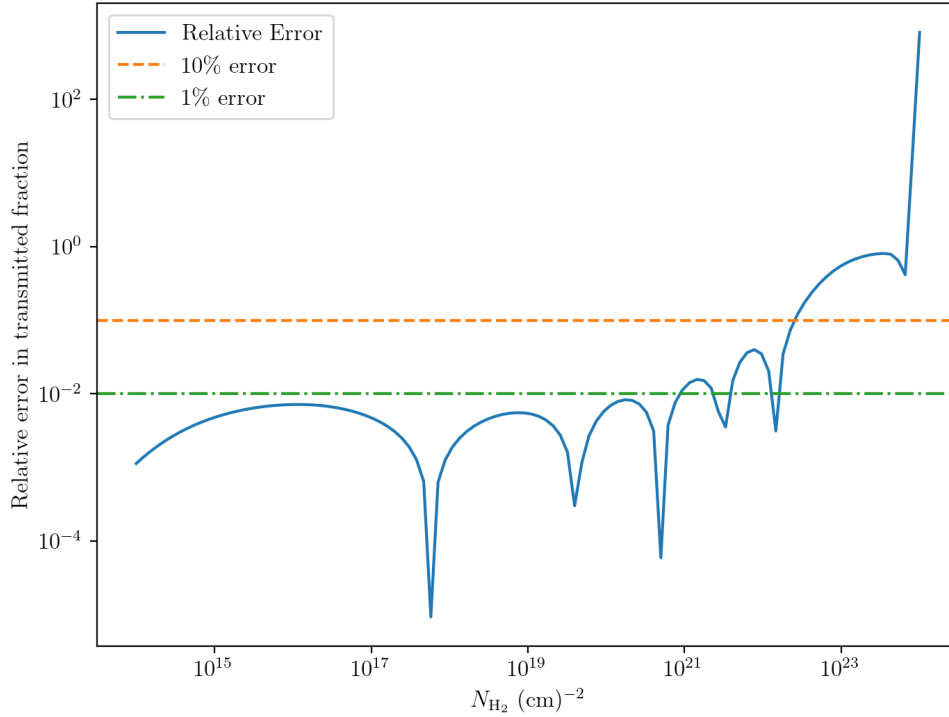
FIGURE 3.7: Relative error between the fraction of flux transmitted through the Lyman-Werner band and the functional fit given by Equation 3.18 as a function of N_{H_2}. The functional fit exceeds an error of 10% at $N > 5 \times 10^{22}$ cm^2, however the actual intensity of Lyman-Werner radiation at this depth is relatively low, so this error should not make much impact in practice.

In Figure 3.7, we compute the relative error between the integrated transmitted flux calculated using Heays et al. (2017) data (Equation 3.17) and the functional fit from Equation 3.18. At low column densities, the error on this fit is less than 1%, and between 10^{21} cm^{-2} $< N_{H_2} < 5 \times 10^{22}$ cm^{-2}, the error is less than 10%. Beyond this depth, the error between the fit and the integrated form exceeds 10%. At this depth, the actual intensity of the Lyman-Werner band will have been reduced to $I_{LW}(N_{H_2}) < 10^{-3}$ times the incident value, so we do not expect the large error in this range to strongly alter the behaviour of the gas.

The largest flaw in this method is the absence of Doppler broadening. Doppler broadening on the cloud scale can be accounted for by performing a convolution of the Heays et al. (2017) cross section data with a Doppler function. This issue is more complex when considering Doppler shifting based on the relative velocities between different clouds in the ISM. The Doppler shifting of light due to bulk velocity dispersion means that photons that were in the line wings of one cloud may be in the line centers of another cloud, and can therefore be absorbed more easily than is expected at that column density N_{H_2}. This is a limitation of the Draine and Bertoldi (1996) shielding function as well, which is also unable to capture Doppler shifting between separate clouds in the ISM. It is worth noting that the original Draine and Bertoldi (1996) shielding function was designed to fit stationary photodissociation fronts, not the transmission of Lyman-Werner radiation across the ISM. Further investigation may be necessary to establish whether it is appropriate to apply this function in the environment of the ISM, or whether a new functional fit is necessary.

3.5   The testcool Program

To test that my implementation of H_2 physics into the GASOLINE chemistry network functioned correctly, I made use of the testcool program from the GASOLINE testing package, and compared to results from a previous iteration of the GASOLINE chemistry network presented in Shen (2010). The testcool program computes cooling rates at a grid of density and temperature values (n, T) at a fixed redshift. The redshift determines what cosmic UV background the gas is exposed to, and also how much PdV work is done on the gas due to adiabatic expansion of the universe. At $z = 3$, the cooling due to adiabatic expansion is -1.71439×10^{-8} erg. The current example shown in Figure 3.8 reproduces a similar shape to Figure 3.13 from Shen (2010); this illustrates that the chemistry network is implemented correctly, and any differences between the two plots should be a result of the physics I have developed in this thesis.

Figure 3.8 represents the cooling function for gas exposed to the cosmic UV background at redshift $z = 3$. The diagram bears striking similarities to the phase diagram of a galaxy. In particular, we expect to see most of the ISM gas residing near equilibrium. In Figure 3.8, equilibrium is traced by the lowest contour in dark blue. Gas below this contour is heated towards equilibrium, while gas above this contour cools towards equilibrium. This plot is very similar in shape to Figure 1.1 from Shen (2010), which was computed from a previous iteration of the GASOLINE cooling code without molecular
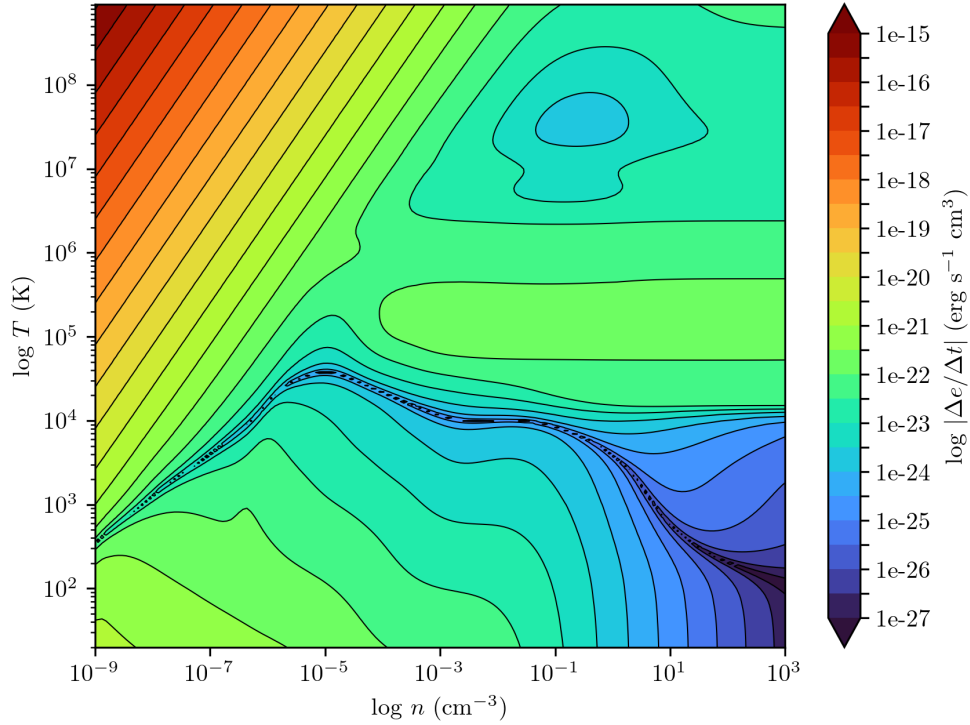
FIGURE 3.8: Net cooling rates from the testcool program at $z = 3$, as a function of density and temperature (n, T). This plot is directly comparable with Figure 3.13 of Shen (2010) (shown in Figure 1.1), which represents a previous version of the chemistry code prior to the addition of H_2. The gas is affected by cooling due to adiabatic expansion, photoelectric heating, and is exposed to a Haardt and Madau (2012) UV background at $z = 3$. This cooling code does not include cosmic rays, as we do not have a prescription for cosmic ray ionization or heating as a function of redshift. This plot shows heating and cooling over $\Delta t = 3 \times 10^4$s; given that the chemistry timescales are longer than this Δt, this plot shows the approximately instantaneous cooling function. The lowest contour in dark blue represents the equilibrium state of the gas, and ranges across all densities n and temperatures from 10^2 K $< T < 10^4$ K. Regions above the equilibrium curve are cooling, while regions below the equilibrium curve are heating.

hydrogen. This similarity is expected, since at solar metallicity H_2 cooling should have a minor impact relative to metal cooling.

The highest rate on this diagram is found in the high temperature, low density regime. At first this would seem to indicate that gas does not remain at this temperature and
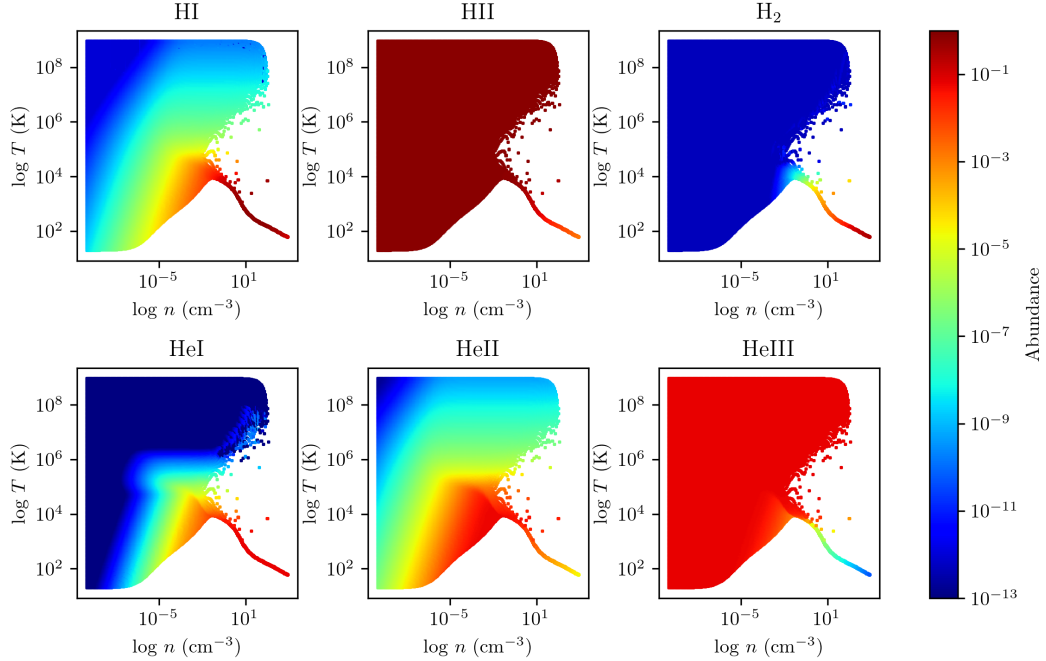
FIGURE 3.9: Abundances of each species as a function of (n, T) under the same conditions as in Figure 3.8 but after $\Delta t = 1$ Myr of integration, rather than instantaneous cooling. Here, the T axis shows the *final* temperature value, after cooling. This shows regions of strong heating and cooling, highlights shape of the equilibrium curve, and provides an estimate for equilibrium abundances. Since cooling allows temperature to change, there are large gaps in the data where gas cooled to equilibrium very efficiently. Much of the gas is able to cool to equilibrium well within the 1 Myr of integration time. Data that was initially in the blank space moved vertically to the equilibrium curve while remaining at fixed density n, either by cooling (decreasing T) or heating (increasing T).

cools very rapidly, but this is not the case. We can see in Figure 3.9 that gas can remain in this phase for up to 1 Myr while gas that has both high temperature and high density cools to equilibrium more quickly. The key point here is that the cooling rate given is normalized to the density of the gas, erg s^{-1} cm^3. Although the cooling rate in the high temperature, low density range of Figure 3.8 is relatively high, the density of the gas is very low, so the gas is restricted in its ability to effectively cool.

3.6 The RadT1d Setup

To test the implementation of H_2 shielding, I developed an idealized one-dimensional test case that simulates the evolution of a cloud of gas exposed to ionizing and dissociating radiation. This test program is called RadT1d, and is part of the GASOLINE testing package.[3] An original RadT1d setup existed in the testing package, but the functionality of this program was extremely limited and did not provide the necessary details to test my implementation of H_2. I made several significant developments to the RadT1d code over the course of this thesis, bringing it from a simple test of radiative transfer through cells to a more thorough and precise model of HII regions and photodissociation regions for differing spectral shapes and intensities, with shielding for H_2.

Since GASOLINE is a non-equilibrium chemistry solver, and the resolution elements of the RadT1d cloud are linearly spaced, one of the largest developments to RadT1d was the addition of an adaptive timestep. Without the adaptive timestep, none of the tests performed with RadT1d would have been feasible, as solving a PDR model requires integrating with precision right at the radiation front. This addition also enables RadT1d to solve for the time dependent evolution of radiation fronts.

The primary purpose for RadT1d is to test my implementation of H_2, specifically my treatment of shielding. RadT1d is capable of using all radiation bands in its calculation (Section 3.3), so I can test my modifications to the Lyman-Werner band (H_2 photodissociation) and my implementation of the 15.2+ band (H_2 photoionization). I also use RadT1d identify which physical processes are important to capture at the scale of photodissociation regions (Hollenbach and Tielens 1999).

3.7 Comparison to a Photodissociation Region Benchmark

To evaluate the ability of my chemical network to simulate correct photodissociation regions, I compared the RadT1d simulation to the PDR benchmark comparison test presented in Röllig et al. (2007). In this paper, the authors tested several dedicated PDR codes against eight model clouds, in order to understand the difference between these codes and how the methods chosen by each code affected the resulting simulation. This data presents me with the opportunity to see if RadT1d can reproduce the same

---

[3]For future readers, the code I actually use is called `RadT1d_H2.c`, as enough alterations were made to this program to warrant a new version. This program may eventually merge with the original `RadT1d.c`. For the purpose of this thesis, any reference to RadT1d is technically a reference to the `RadT1d_H2.c` code.

detailed structure as dedicated PDR codes, identify the errors and limitations in the chemistry network I have developed, and understand what degree of errors are tolerable.

Although the authors simulated eight model clouds, not all results are presented in this paper. I chose two model clouds to compare against, both with density $n = 10^3$ cm^{-3}, but exposed to different ISRF intensities. Both clouds use the same ISRF from Draine (1978), which only contains FUV and LW photons. Since the intensity of this field is 0 for all energies above 13.6 eV, there are no photons capable of ionizing HI, HeI, or HeII, so we are only comparing the behaviours of H$_2$ formation and destruction, as well as photoelectric heating.

It should be noted that one of the models we are comparing against, labelled the F1 model, was simulated at constant temperature. RadT1d is not actually capable of simulating at constant temperature, so in this comparison we will see some effects of heating and cooling that actually cause our solution to deviate from the benchmark solution. We will discuss the error incurred by this assumption later on. This constant temperature model is still useful for understanding the effect of modifying the radiation intensity on our cloud, as the second model, labelled the V2 model, is exposed to an ISRF with 10^4 times stronger intensity. Ideally I would compare the V1 and V2 models from Röllig et al. (2007), as both those models involve simulating the full thermodynamic state of the gas to get a variable temperature, however the data from the V1 model is not presented in this paper, so we must compare to the F1 model instead.[4]

The F1 model is simulated at a density of $n = 10^{-3}$ cm^{-3}, and is exposed to an ISRF at 10 times the Draine (1978) intensity ($\chi = 10$). As mentioned previously, the Röllig et al. (2007) F1 simulation is performed at a constant temperature of $T = 50$ K, whereas the RadT1d simulation is performed with variable temperature. The results of this comparison are shown in Figure 3.10.

In Figure 3.10, the HI/H$_2$ transition occurs at a shallower depth in RadT1d than in the Röllig et al. (2007) tests, suggesting that once shielding begins to take effect, my code produces H$_2$ more rapidly than expected. Correspondingly, the photodissociation rate, while initially within the benchmark range of values, decreases more rapidly with depth than in the Röllig et al. (2007) test. This suggests that the Draine and Bertoldi (1996) shielding function may be too aggressive in this environment. The PDR codes used in the Röllig et al. (2007) comparison tests often do not rely on a prescription for the shielding function, but rather model the population of excited states of H$_2$ and

---

[4]Data for all models from Röllig et al. (2007) are available online, but I did not find them until after the completion of this analysis.
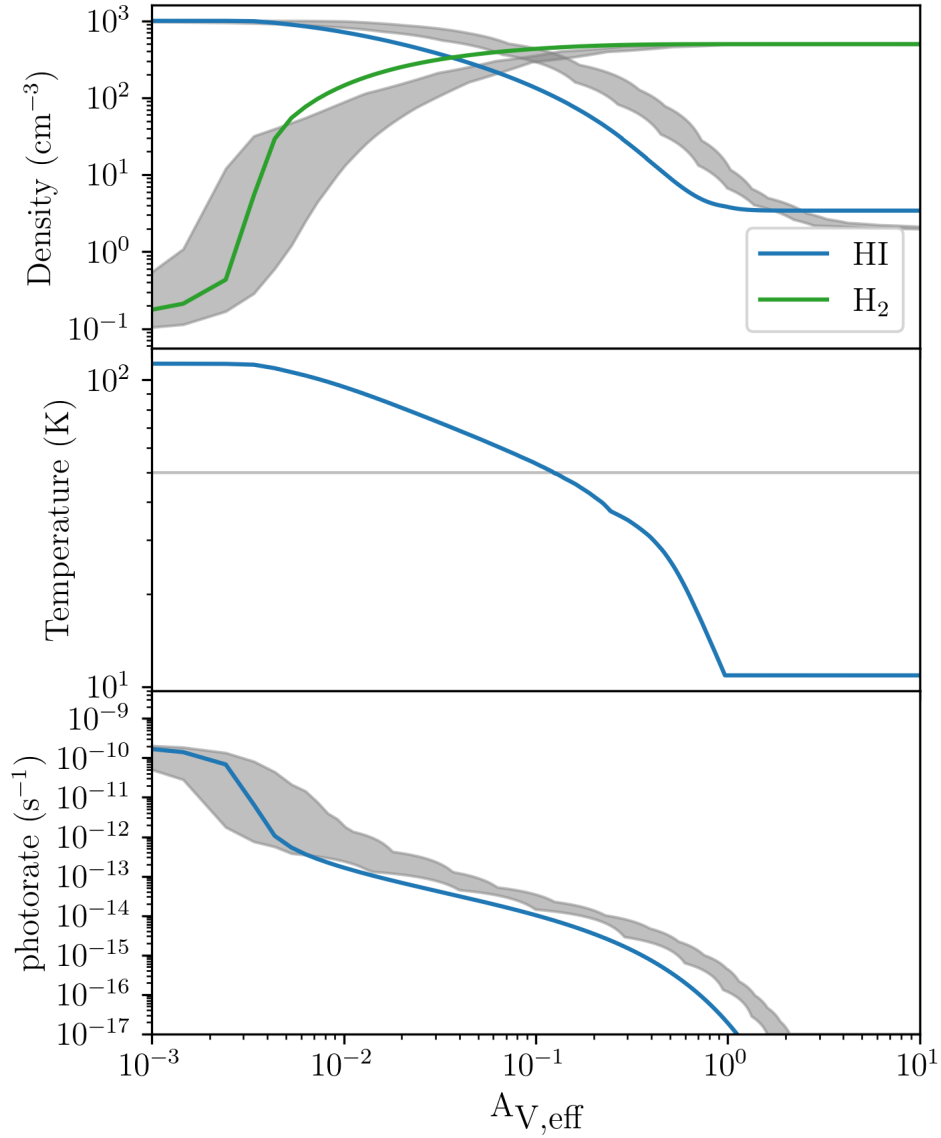
FIGURE 3.10: Comparison of RadT1d simulated cloud (solid lines) to the spread of simulated results using various PDR codes from the Röllig et al. (2007) comparison (grey areas) for the F1 benchmark test case ($n = 10^3 \text{cm}^{-3}$, $\chi = 10$, $T = 50$ K). Plots show density of HI and H_2 (above), temperature of the cloud (middle), and H_2 photodissociation rate (below) as a function of depth ($A_V = 6.289 \times 10^{-22} N_{H_{total}}$).

integrate the LW spectrum from first principles to obtain the photodissociation rate as a function of depth (Black and van Dishoeck 1987; Sternberg and Dalgarno 1995; Shaw et al. 2005; Le Petit et al. 2006). An inherent limitation of the shielding function is that

it cannot adapt to new environments. It is calibrated for the Draine and Bertoldi (1996) conditions, but in reality shielding can vary based on the population of H_2 excited states, which is dependent on temperature (Draine and Bertoldi 1996).

We also find some discrepancy between the HI fraction deep into the cloud. The trace HI fraction at large depths is typically set by the rate of H_2 destruction by cosmic rays, and this parameter is calibrated to $\xi_{CR,H} = 5 \times 10^{-17}$ s^{-1} in both the Röllig et al. (2007) F1 model and in RadT1d. So, the cosmic ray destruction rate is not the source of this discrepancy; in fact, we will see in the V2 model, it is in good agreement between the two codes. Instead, this discrepancy is caused by the rate of formation of H_2 on dust grains. In Section 2.2.1, we discussed the different prescriptions for dust grain formation coefficients R_d, and in Röllig et al. (2007), the authors use a rate coefficient that is proportional to $T^{1/2}$. In RadT1d, the temperature of the gas reaches the cooling floor of $T = 10$ K at high depths ($A_V > 1$), whereas in the F1 model, T is held at a constant 50 K. This behaviour can be seen in the middle panel of Figure 3.10, where the grey line shows the constant 50 K temperature of the F1 model. Due to this temperature discrepancy, the rate at which HI forms into H_2 on dust grains at high depths is a factor of 2 smaller in RadT1d than in the F1 model. Since this process that removes HI is suppressed, we find that there is more HI at high depths in RadT1d than there is in the Röllig et al. (2007) F1 model.

Next, we simulated the V2 model, which is also simulated at a density of $n = 10^3$ cm^{-3}, but is exposed to a much more intense Draine (1978) field with $\chi = 10^5$. The results of this comparison are shown in Figure 3.11. Additionally, in this model the full thermodynamic state of the gas is solved, so T is no longer held constant. This gives us another constraint on our PDR model, which can also be seen in Figure 3.11.

In Figure 3.11, we can see that the initial H_2 fractions are in agreement, suggesting that the ISRF photodissociation rate and H_2 formation rates are balanced. Additionally, the high-depth fractions ($A_V > 10$) are also in agreement, indicating that the cosmic ray destruction rate for H_2 is calibrated correctly, providing a floor for the trace amount of HI. Once again, at moderate depths, the HI/H_2 transition occurs earlier in RadT1d than any codes in the Röllig et al. (2007) test. This transition seems to correlate with our photodissociation rate decreasing more rapidly than in the benchmark models, shown in the lower panel of Figure 3.11. Since the shielding function itself is calibrated based on N_{H_2}, if the transition to H_2 occurs earlier, the column of N_{H_2} will increase more rapidly, leading to a subsequent rapid increase in the shielding. It is possible that our shielding function is slightly too strong at low depths, a feature we will see again in Section 3.8.1.
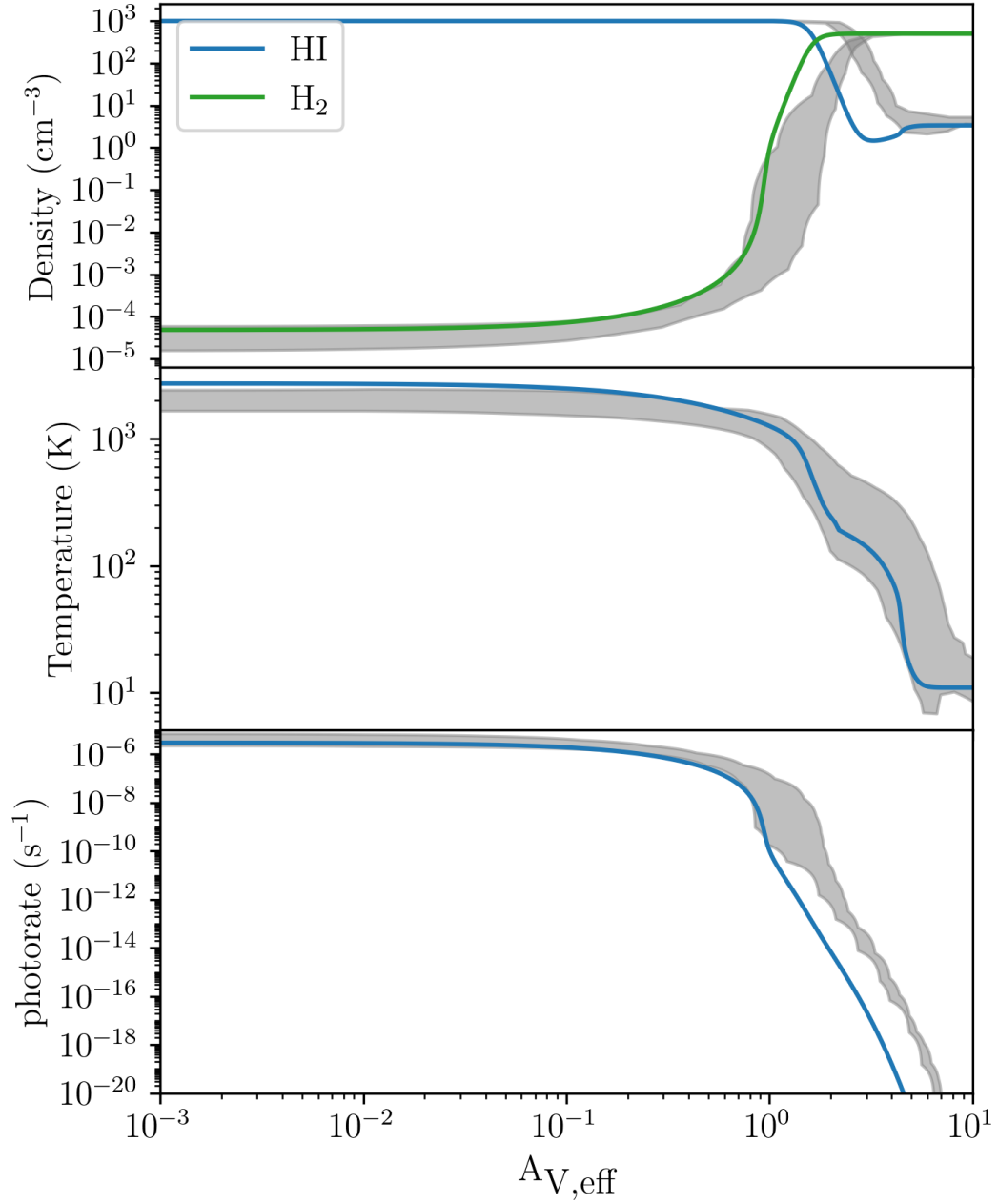
FIGURE 3.11: Similar to Figure 3.10, but for the V2 test case ($n = 10^3 \text{cm}^{-3}$, $\chi = 10^5$, with variable T).

The temperature profile in Figure 3.11 was initially in disagreement with the Röllig et al. (2007) V2 benchmark, with an initial temperature that was a factor of 2 too cool. The source of this error was due to ionization state of metals under the cooling table

settings I had used. The ionization state of the gas strongly affects the cooling rate — see Figure 1 of Gnedin and Hollon (2012) for an example. Dedicated PDR codes such as the ones used in the Röllig et al. (2007) comparison will solve for the ionization states of these metals for any given radiation field (Ferland et al. 2017). Meanwhile, the only way that the cooling table is able to adapt to different radiation fields is through a redshift dependency, which parameterizes the ionization state of the metals based on the shape of the UV background spectrum at that redshift. Initially, this RadT1d simulation was run at redshift $z = 0$, but is supposed to simulate a cloud that is only exposed to the Draine (1978) ISRF, which only contains photons with energies $h\nu < 13.6$ eV — the ionization state of the gas should therefore be very neutral. At redshift $z = 0$ however, gas that is exposed to the cosmic UV background is highly ionized, so the metal table at this redshift provided very strong cooling. Therefore, I re-ran this simulation and explicitly used a high redshift column of the metal cooling table, $z = 16$. The cosmic UV background at redshift $z = 16$ has low intensity, so the ionization state of the metals is more neutral, which is more in line with what we expect for the ISM and this benchmark. This change greatly improved our fit to the temperature profile, which is currently displayed in Figure 3.11, although the temperature at the leading edge of the cloud is slightly higher than the Röllig et al. (2007) benchmark values. This correction illustrates the issues with the cooling table when exposed to varying spectra. While the ionization states of metals from $z = 16$ are much closer to the ionization states expected for solar metallicity gas exposed to the Draine (1978) ISRF, the metal table is still not calibrated for this specific radiation field, so it is difficult to disentangle whether any remaining discrepancy between temperature in the Röllig et al. (2007) benchmark and RadT1d is due to the metal table calibration or due to some specific heating or cooling treatment in our model.

Ultimately, the Röllig et al. (2007) benchmark test suggests that there is a range of acceptable values for PDR codes. We can tune RadT1d to lie within these limits in most situations, however using a shielding function inhibits our ability to capture the detailed structure of H_2 shielding, which can lead to differences in the depth at which the HI/H_2 transition occurs by a factor of 2. If our primary concern is to adopt this H_2 model in galactic scale simulations, where the the HI/H_2 transition is unlikely to be resolved, then these errors are acceptable. We also find that metal cooling is dependent on the intensity of the radiation field, which varies as a function of depth. A full solution to metal cooling is beyond the scope of this thesis.

3.8 HII region with Cloudy

To examine the ability of our model to employ the full 12-band radiation spectrum, we simulate an HII region that leads into a photodissociation region. We then compare our results to the solution simulated with CLOUDY, a spectral synthesis and plasma simulation code that can simulate astrophysical environments under the effects of radiation (Ferland et al. 2017). This code was involved in the Röllig et al. (2007) comparison test, and was able to successfully fit their benchmark. Röllig et al. (2007) comment that the CLOUDY code, alongside the MEUDON code (Le Petit et al. 2006), was one of the most detailed codes studied in their comparison, generally relying less on fitting functions than other codes. In particular, CLOUDY is capable of reproducing H_2 shielding from first principles physics (Shaw et al. 2005), using a detailed spectrum and a full model of the excited states of H_2. A comparison with CLOUDY therefore provides an excellent test for our use of the Draine and Bertoldi (1996) shielding function to solve for H_2 dissociation in RadT1d. Our goal with this test is to show that our chemistry network is complex enough to resolved the detailed structure of photodissociation regions when all hydrogen and helium species in our network are involved.

For this test, we select a set of initial conditions that can generate an HII region and photodissociation region in CLOUDY, and then apply those same initial conditions to RadT1d. We then run RadT1d to equilibrium, and compare the resulting cloud profiles. Specifically, we examined the temperature, H_2 photodissociation rate, and mass fraction of each species as a function of the H_2 column density, N_{H_2}. We chose to plot these profiles in terms of column of H_2 rather than total column density so that we can make a more direct comparison between the fraction of each species and the dissociation rate to the shape of the shielding function presented in Draine and Bertoldi (1996).

3.8.1 Comparing Cloudy with RadT1d

Using CLOUDY, we generated a plane-parallel slab of gas with density $n = 100$ cm^3, irradiated by a 40000K blackbody source with intensity $10^{-2.8}$ erg cm^{-2} s^{-1}. This intensity was chosen to be roughly equal to that of the Habing (1968) field, $G_0 = 1.6 \times 10^{-3}$ erg cm^{-2} s^{-1}. The spectrum of this source was then extracted from CLOUDY and put directly into RadT1d using the 12-band treatment for radiation spectra. We then ran RadT1d to equilibrium using the same initial conditions, and compared results from the two codes. The structure of the HII region and photodissociation region is shown in Figure 3.12.
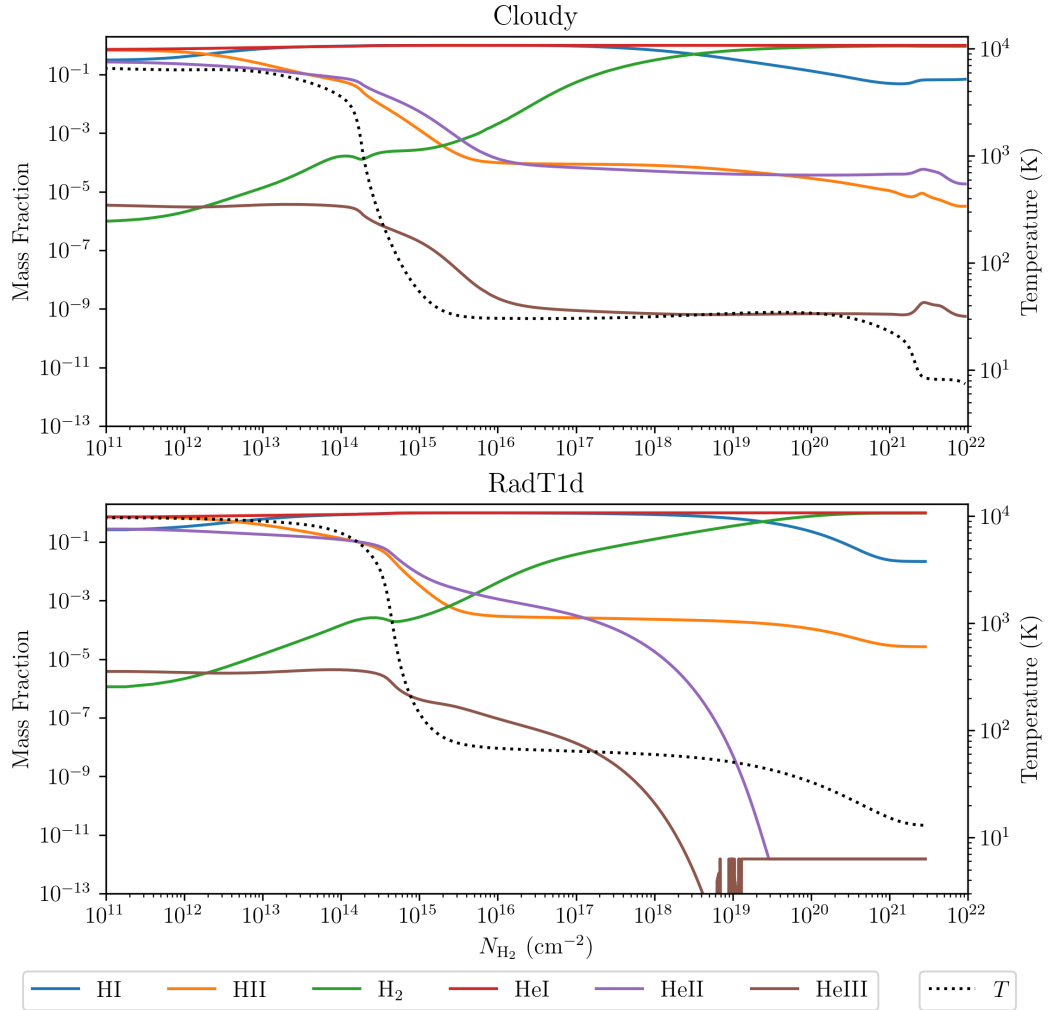
FIGURE 3.12: The mass fraction of each hydrogen and helium ionization state as a function of H_2 column density in the CLOUDY (above) and RadT1d (below) HII region simulations. Temperature is shown as the dotted black line. The shielding function produces a similar behaviour between the codes for HI and H_2, and a trace HI fraction persists to high column densities. There is some discrepancy in the temperature profile at low to moderate N_{H_2}, with RadT1d typically being hotter than CLOUDY. The cosmic ray ionization rate produces a floor for the HII fraction, but in CLOUDY it seems that HeII and HeIII also have floors, suggesting that cosmic ray ionization of Helium needs to be added to RadT1d in order to complete the PDR model.
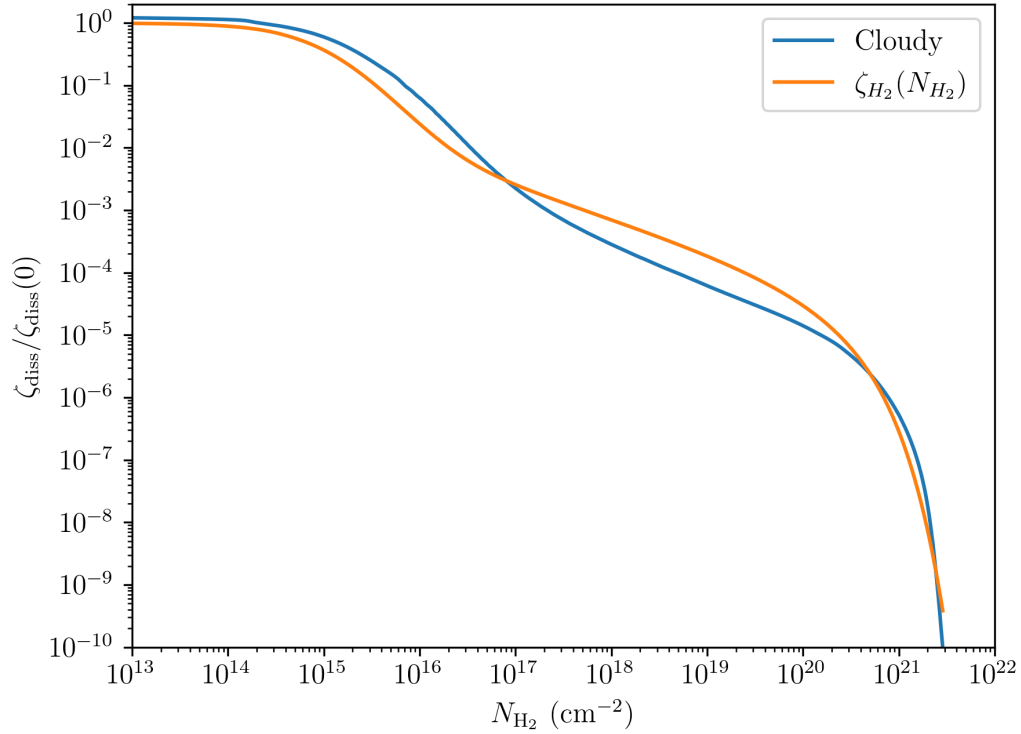
FIGURE 3.13: Plot of photodissociation of H_2 by LW photons as a function of H_2 column density using the explicit shielding approximation from Equation 3.2. This equation yields a similar profile to the expected H_2 self-shielding profile: the dissociation rate is suppressed at low column densities ($10^{14} < N_{H_2} < 10^{18}$), and includes the persistent tail of dissociation at high $N_{H_2} > 10^{18}$.

In the upper panel of Figure 3.12, I show the structure of the region generated with CLOUDY, and in the lower panel, the region generated with RadT1d. Using the chemical network I have developed, RadT1d is capable of producing a qualitatively similar structure to the CLOUDY simulation, albeit with some slight differences. Notably, this simulation would have been impossible prior to the development of this model, as GASOLINE contained no prescription for the detailed interaction of H_2 with radiation.

There is some disagreement in the behaviour of HeII and HeIII towards high column densities. This is likely due to the absence of a cosmic ray ionization term for helium in my chemical network, which would set a floor on these mass fractions at higher column densities. The temperature profile in RadT1d also exhibits a similar shape to that

of CLOUDY, but the RadT1d simulated cloud appears to be too warm at the leading edge: the CLOUDY run suggests a temperature of $T \sim 7000$ K, while RadT1d produces a temperature closer to $T \sim 10000$ K. Similarly, in the photodissociation region of the cloud (which starts around $N_{H_2} \sim 10^{15}$ cm^{-2}), CLOUDY finds a temperature of $T \sim 30$ K, whereas RadT1d suggests $T \sim 60$ K.

The other key feature that I want to highlight in this comparison is the depth where the transition from HI to H$_2$ occurs. Looking at Figure 3.12, we see that in CLOUDY the H$_2$ fraction exceeds the HI fraction starting at $N_{H_2} \sim 4 \times 10^{18}$ cm^{-2}, but in RadT1d this transition does not occur until $N_{H_2} \sim 2 \times 10^{19}$ cm^{-2}, when the column of H$_2$ is almost a factor of 10 larger. This behaviour can be understood by comparing the H$_2$ photodissociation rate as a function of depth between CLOUDY and RadT1d, shown in Figure 3.13. As discussed previously, the H$_2$ photodissociation rate in RadT1d is fit using the Draine and Bertoldi (1996) approximation (Equation 3.2), which is constrained to follow the behaviour of the shielding function (Equation 2.17). Meanwhile, CLOUDY reproduces a behaviour similar to the shielding function from first principles physics. Comparing these two profiles indicates that, for the conditions we are simulating in this test, the shielding function suppresses H$_2$ photodissociation a little too strongly at low column (10^{14} cm^{-2} $< N_{H_2} < 10^{16}$ cm^{-2}), but then overestimates the amount of H$_2$ photodissociation occurring deeper into the cloud (10^{17} cm^{-2} $< N_{H_2} < 10^{21}$ cm^{-2}). The discrepancy in H$_2$ photodissociation at these moderate depths means that a larger column density of N_{H_2} is required before H$_2$ dissociation is suppressed enough that the cloud can transition from being atomic (HI) to molecular (H$_2$). Indeed, the photodissociation rate that CLOUDY finds at the point of HI to H$_2$ transition (at $N_{H_2} \sim 4 \times 10^{18}$ cm^{-2}) is the same photodissociation rate that RadT1d finds at its point of HI to H$_2$ transition (at $N_{H_2} \sim 2 \times 10^{19}$ cm^{-2}).

3.9   Two-Sided Model

During the development of this model, a decision had to be made regarding how to calculate the H_2 dissociation rate when radiation is received from multiple directions. Radiation along each incoming ray can have different intensities, and may have traveled through different intervening columns of H_2, thereby being shielded by different amounts. This situation is encountered every time radiation is computed in the full TREVR2 scheme, so properly modeling this behaviour is crucial for adopting this model in actual galaxy simulations. In other radiation bands, such as for HI ionizing radiation, the solution is relatively simple; the code takes the sum of all incoming fluxes along each ray, and use the total flux to calculate the photoionization rate at that point. For H_2 however, this solution is not effective, as the flux from different directions will have been shielded by different amounts, so it is not possible to apply one function that captures the full behaviour of shielding from all directions.

Normally, ionization rate is calculated by integrating the product of the flux (or intensity, I_ν) and the cross section (σ_ν), as in Equation 3.20:

$$\xi_i = \int_{\nu_1}^{\nu_2} I_\nu \sigma_\nu d\nu \tag{3.20}$$

In this scenario, integrating the sum of each intensity I_ν from each incoming ray is equivalent to taking the sum of all photoionization rates ξ_i from each ray. For H_2, the shielding approximation (Equation 3.2) is used to obtain $\zeta_{H_2}(N_{H_2})$. We can use Equation 3.20 to compute the photodissociation rate at the source, $\zeta_{H_2}(0)$, but photodissociation at a depth N_{H_2} is based on the shielding function, so the sum of all $\zeta_{H_2}(N_{H_2})$ is not equivalent to the integral over all incoming LW intensity, I_{LW}.

Our solution is to track all the incoming photodissociation rates, rather than all the incoming LW intensities. This way, each ray is shielded separately based on the column of material it travels through. This means that one of the Lyman-Werner bands in the radiation code now tracks the H_2 dissociation rate, while the other Lyman-Werner band tracks the physical flux at that depth.

In order to test that this method correctly calculates the photodissociation rate when two rays intersect, I illuminate my PDR model in RadT1d from both sides, and compare with simulations from the MEUDON PDR code (Le Petit et al. 2006). This code was chosen primarily for its ability to illuminate a PDR from two sides with different intensities (Goicoechea and Le Bourlot 2007). We model four clouds of varying thickness

from $A_V = 0.01$ to $A_V = 1$ so that when the LW intensities overlap at the centers of the clouds, they will have experienced increased amounts of shielding with each subsequent simulation. The flux from the far side of the cloud has an intensity that is 50% that of the flux at the near side of the cloud. This way, the photodissociation rate from each direction is not symmetrical. In order to perform a direct comparison between MEUDON and RadT1d, both models use a constant coefficient for H_2 formation on dust grains of 3.5×10^{-17} cm^{3}s^{-1} (see Section 2.2.1 or Equation 2.7) rather than the more complex formation mechanisms implemented in the MEUDON code (Le Bourlot et al. 2012).

This comparison is shown in Figure 3.14. The general agreement between two-sided RadT1d model and the qualitative shape of MEUDON profile suggests that our method for computing net photodissociation based on the independent contribution from different rays is acceptable. Adding prescriptions for dust shielding, cosmic ray ionization, and photoelectric heating into RadT1d generally improves fit to the MEUDON model. Specifically, the cosmic ray ionization of H_2 leads to a much better agreement in the H I fraction at high depths. There is however a factor of 10 discrepancy in the abundance of H II across all depths, which should be set by the cosmic ray ionization rate of H I. Possible sources for this discrepancy may be shielding of cosmic rays in the MEUDON code. The overabundance of H_2 seen in the thin cloud at $A_V = 0.01$ is due to a tendency for the shielding function to overestimate shielding at low columns. We show this behaviour in Figure 3.15. Notably, this discrepancy is not due to the independent treatment of photodissociation from each direction, but simply due to limitations of the shielding function.
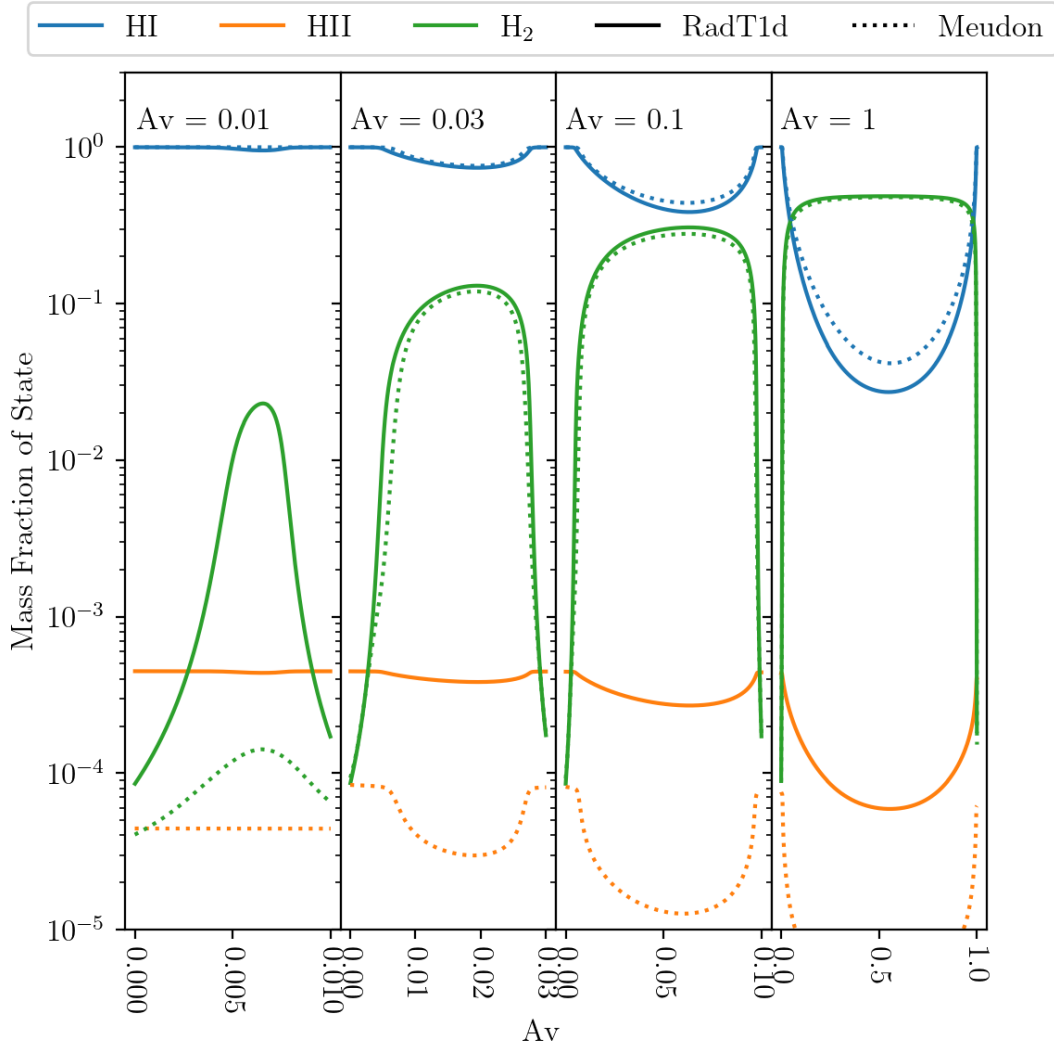
FIGURE 3.14: Comparison of RadT1d to MEUDON PDR code. Solid lines indicate abundances from RadT1d while dotted lines indicate values from MEUDON. Clouds were illuminated from both sides. The thickness of the simulated cloud increases in each panel from left to right, as indicated by the label in the top left corner. Despite the cosmic ray ionization rate being set to the same value between RadT1d and MEUDON, the HII fraction differs by a factor of ~ 10. H_2 fractions agree at high depths, but RadT1d code overestimates the amount of H_2 formed in the thin cloud ($A_V = 0.01$).
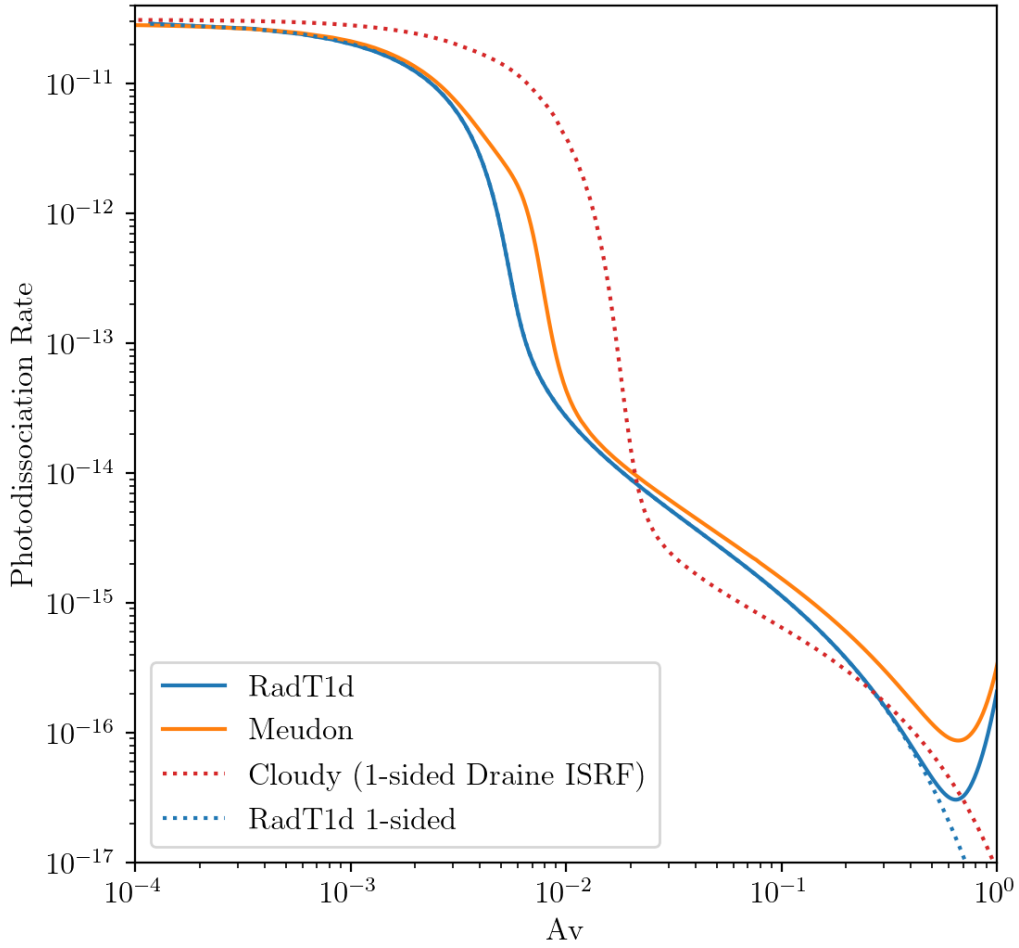
FIGURE 3.15: Comparison of photodissociation rates as a function of depth for the $A_V = 1.0$ cloud of the RadT1d vs. MEUDON comparison from Figure 3.14. RadT1d underestimates the photodissociation rate relative to MEUDON near $A_V < 10^{-2}$ and again near $A_V < 10^0$. This causes RadT1d to overestimate the abundance of H_2 in the thin cloud case ($A_V = 0.01$) and underestimate the abundance of HI in the thick cloud case ($A_V = 1.0$) seen in Figure 3.14. The dotted blue line shows the RadT1d photodissociation rate as a function of depth when only one side of the cloud is illuminated. Additionally, the dotted red line shows the photodissociation rate as a function of depth from CLOUDY for the same input field, with one-sided illumination.

3.10 Thermal History of the Universe

To simulate the evolution of the universe, we need to specify an initial condition. The starting point we use as our initial condition depends on what we are interested in learning. In galaxy scale simulations, we can often get away with constructing initial conditions that will give us a galaxy in isolation; we do not simulate the rest of the universe. Sometimes, however, we are interested in simulating the formation of many galaxies. We do not start as early as the Big Bang, nor even as early as the decoupling of the CMB at $z \approx 1100$, but we use the information encoded in the CMB to set our initial conditions. In practice, such simulations instead start around $z \approx 500$ where gas has begun to flow into dark matter overdensities, but well before the formation of the first stars.

In the early universe ($500 > z > 100$), gas temperature is strongly coupled to CMB temperature. Both gas and the CMB photons cool through adiabatic expansion of the universe (PdV work), but gas experiences additional cooling processes. The dominant cooling process in this regime is Compton cooling (Seager et al. 2000); no metals are available and no H_2 has formed yet to provide cooling, but there are free electrons left over from incomplete recombination during the CMB era that will enable H_2 formation via the gas-phase pathways. As the universe continues to expand, the gas temperature eventually decouples from the temperature of the CMB photons. We illustrate this behaviour in Figure 3.16. In the high-redshift regime ($z > 30$, before the onset of star formation), the behaviour of $T_g(z)$ is fairly well constrained.

3.10.1 Chemical evolution during the cosmic dark ages

Prior to the formation of the first stars, there are no metals in the universe that can contribute to cooling. Molecular hydrogen provides an important cooling pathway in the primordial universe, with consequences for the fragmentation and collapse of galaxies during the galactic dark ages and the formation of the first stellar populations (Bovino and Galli 2019), and may even have implications for the seeding of supermassive black holes (Dunn et al. 2018). Therefore, correctly reproducing the abundance of H_2 throughout the galactic dark ages is crucial for modeling the early universe. To that end, we want to test that the chemical network developed throughout this thesis can correctly reproduce the chemical evolution of H_2 between the surface of last scattering and the onset of star formation. We know that the thermal evolution of the universe in this epoch is determined by the CMB temperature and gas cooling (Seager et al. 2000; Galli and Palla 2013), so we can use this behaviour to constrain our chemical network.
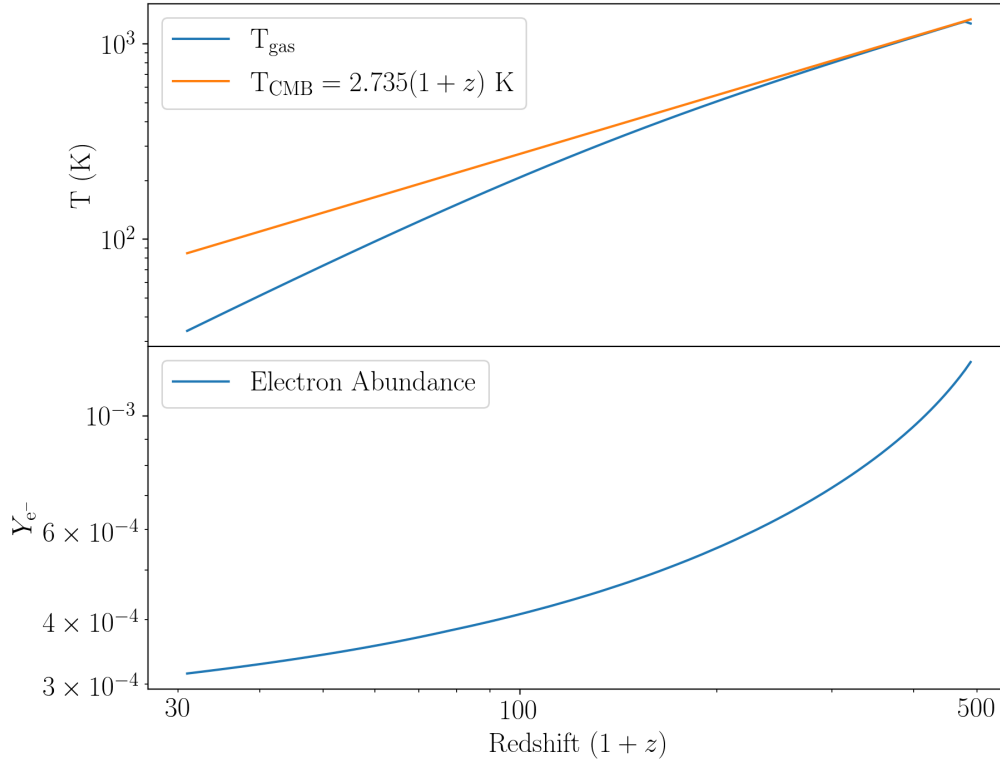
FIGURE 3.16: Plot of gas temperature and ionization fraction as a function of redshift from $z = 500$ down to $z = 30$. The CMB can only cool through the expansion of the universe (PdV work), so T_{CMB} is inversely proportional to the inverse of the scale factor $a = \frac{1}{1+z}$. The gas can cool more effectively through Compton cooling, so T_{gas} decouples from T_{CMB} during this epoch. Recombination can be seen through decreasing electron fraction in the lower plot.

To simulate this evolution, we use the cosmo16 model. The cosmo16 setup involves running the full GASOLINE code on a 16^3 volume of gas particles with gravity disabled. Such a volume does not collapse or form stars as the universe evolves, but the chemical and thermal state of the gas is modeled while being exposed to the CMB and undergoing adiabatic expansion due to the expansion of the universe. The closest physical analogue would be simulating a patch of the intergalactic medium throughout cosmic time. This model is ideal for our test, because chemistry, heating, and cooling are the only major processes at play, so we can isolate the effects of our H_2 model on the chemical and thermal state of the gas. At the redshifts we want to simulate ($z \sim 500$ down to $z \sim 30$),

74

radiation from the CMB is much more energetic than in the local universe, and therefore dominates much of the gas-phase H_2 formation physics, specifically constraining the ionization states H^- and H_2^+. This particular test enables us to examine the gas-phase formation pathways for H_2.

For this test, we run cosmo16 from redshift $z = 500$, a typical starting point for cosmological simulations, to $z = 30$, which is around the redshift where the first stars should begin to form. We then compare this data to Seager et al. (2000), who simulate cosmic recombination from $z = 2000$ to $z = 30$. Our goal is to try and capture the formation of H_2 throughout this epoch, and see if we can produce a final H_2 fraction that agrees with Seager et al. (2000). The final abundance of H_2 in the universe freezes out at a value of 6×10^{-7} molecules per baryon (Galli and Palla 2013).

Figure 3.17 shows an overabundance of H^- at all redshifts, which leads to a surplus of H_2 formation at redshift $100 < z < 500$. This increased formation is frozen out, so that by $z = 30$ there is an overabundance of H_2 by 3 orders of magnitude. In this early universe, the only way to form H_2 is through the gas-phase formation processes with H^- or H_2^+ (see Section 2.2.2). H^- only forms from the trace electron fraction that persists due to incomplete recombination in the early universe. Our cosmic UV background tables do not extend above $z > 16$, so in our first simulation there was no ionization of any species.

This comparison revealed that our treatment of H^- and H_2^+ was incomplete. Our model initially did not account for photodetachment of H^-, the reverse of the radiative association (H^-) reaction in Table 2.2. The cross section for photodetachment of H^- peaks around 0.7 eV (Hirata and Padmanabhan 2006; Galli and Palla 2013), which is at a low enough energy that photons in the CMB tail at redshifts $100 \leq z \leq 500$ can suppress the formation of H^- (see Figure 3.18). We should be able to capture these processes using our model for the thermal evolution of the universe shown in Figure 3.16.

Hirata and Padmanabhan (2006) provide a fit for the photodetachment cross section of H^-:

$$\sigma_{H^-} = 3.486 \times 10^{-16} \frac{(x-1)^{1.5}}{x^{3.11}} \text{ cm}^2 \tag{3.21}$$

where $x = h\nu/0.754$ eV. We use this cross-section to tabulate the photodetachment of H^- as a function of redshift based on the intensity of the CMB. The CMB is a near-perfect blackbody (Ryden 2016), and therefore the intensity of the CMB can be obtained
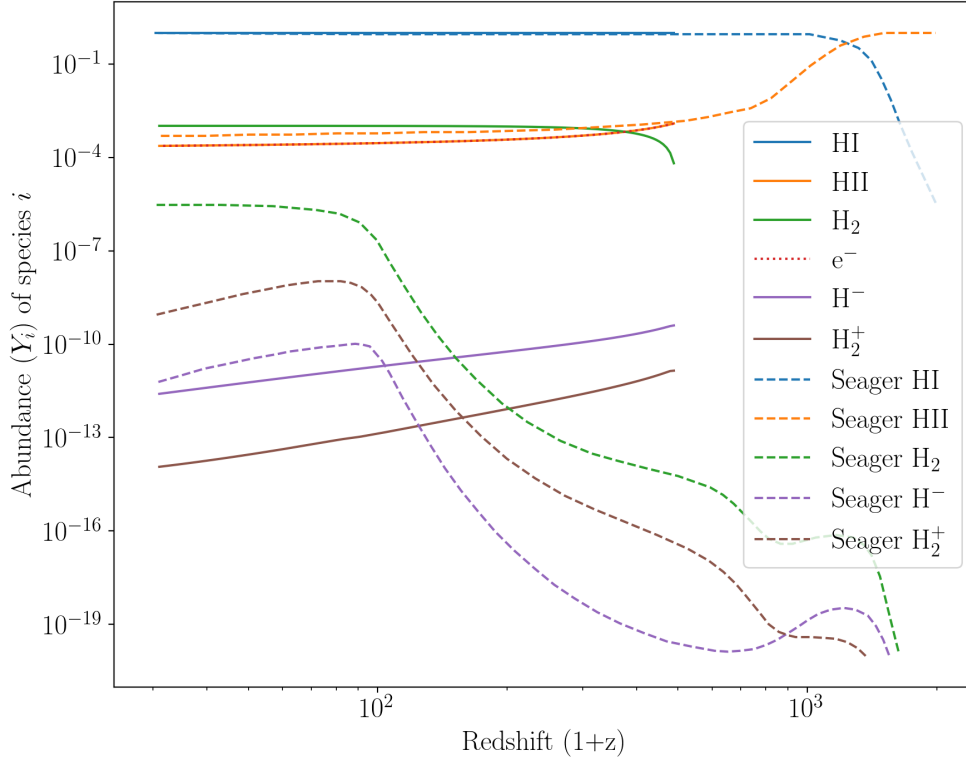
FIGURE 3.17: This figure shows the cosmic evolution of hydrogen species from the recombination era $z > 1100$ to just before the reionization era $z \sim 30$. The x-axis shows increasing redshift; larger redshifts indicate an earlier universe, so the evolution of the universe is traced *from right to left*. Solid lines show data from my cosmo16 simulation, and dashed lines show data from Seager et al. (2000). This cosmo16 run has no ionizing background at these redshifts. An overabundance of H$^-$ at high redshift (purple line) leads to increased H$_2$ formation (green line). This excess H$_2$ is frozen out, so our simulation produces about 300 times more H$_2$ at $z = 30$ than Seager et al. (2000).

using the Planck function:

$$I_\nu = \frac{2h\nu^3}{c^2} \frac{1}{e^{\frac{h\nu}{kT}} - 1} \text{ erg/s/cm}^2/\text{Hz/sr} \tag{3.22}$$

where h is the Planck constant, k is the Boltzmann constant, and c is the speed of light. This intensity depends on the temperature of the CMB, which evolves with redshift as shown in Figure 3.16, $T(z) \approx 2.735(1 + z)$ K.
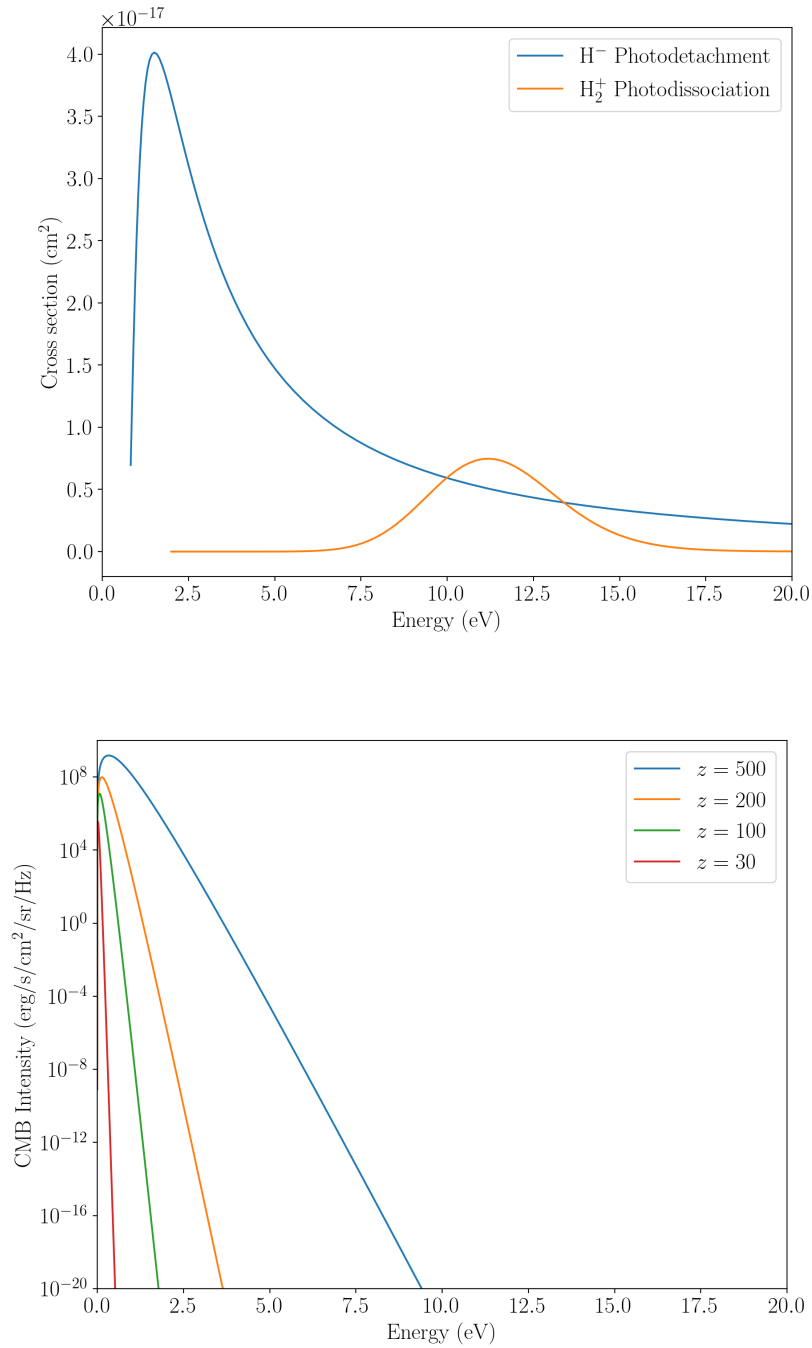
FIGURE 3.18: Above, cross sections for H^- photodetachment and H_2^+ photodissociation. Below, CMB intensity as a function of photon energy ($h\nu$) at various redshifts. The tail of CMB photons is capable of triggering H^- photodetachment, but not H_2^+ photodissociation.

The CMB intensity can also be used to compute the photodissociation rate of H_2^+ as a function of redshift. The cross-section for photodissociation of H_2^+ is given by Shapiro and Kang (1987):

$$\sigma_{H_2^+} = \begin{cases} 10^{(-40.97+6.03(h\nu)-0.504(h\nu)^2+1.387\times10^2(h\nu)^3)}, & 2.65 < h\nu < 11.27 \text{ eV} \\ 10^{(-30.26+2.79(h\nu)-0.184(h\nu)^2+3.535\times10^{-3}(h\nu)^3)}, & 11.27 < h\nu < 21.0 \text{ eV} \end{cases} \quad (3.23)$$

The cross sections for photodetachment of H^- and photodissociation of H_2^+ are shown in Figure 3.18 alongside the CMB intensity at some characteristic redshifts. At high redshifts, the photons in the tail of the CMB are capable of triggering H^- photodetachment, but are not energetic enough to cause much H_2^+ to dissociate. The result of implementing these processes in cosmo16 can be seen in Figure 3.19.

Accounting for the photodetachment of H^- improves our fit to Seager et al. (2000), as seen in Figure 3.19, however there is still an overabundance of H_2 caused by the remaining fraction of H_2^+ at early redshifts. H_2^+ proved more difficult to suppress. Photodissociation of H_2^+ has a threshold energy of 2.65 eV (Bovino and Galli 2019), and the cross section for this photodissociation peaks at 11.7 eV (see Equation 3.23). A naive approach therefore suggests that the CMB background cannot suppress H_2^+, also seen in Figure 3.19. The small turndown we see in the H_2^+ fraction around $z = 500$ is the only contribution that the CMB photons made to suppressing the formation of H_2^+ in this simulation.

At high redshift, the non-LTE population of H_2^+ is important for determining the total abundance (Coppola et al. 2011; Galli and Palla 2013). Higher vibrational states of H_2^+ can be dissociated by less energetic photons (Dunn 1968; Argyros 1974), so that at higher temperatures, the cross section to dissociate H_2^+ broadens towards the lower energy regime (Stancil 1994). The rate of H_2^+ photodissociation therefore strongly depends on the population of these excited states (Coppola et al. 2011; Bovino and Galli 2019), so CMB photons may be able to efficiently dissociate H_2^+, suppressing H_2 formation between $100 < z < 1000$.

It is also worth noting that Seager et al. (2000) have *more* H_2^+ than the cosmo16 simulation suggests at $z < 100$ despite using a similar chemical network. This suggests that Seager et al. (2000) use some different behaviour that we do not capture, as simply suppressing the amount of H_2^+ at high redshifts would not be enough to obtain an agreement with the H_2^+ fraction at low redshifts found in Seager et al. (2000). However, simply adopting the abundance of H_2^+ that Seager et al. (2000) suggest will overestimate the H_2 fraction. The reaction coefficient which governs the charge exchange process to
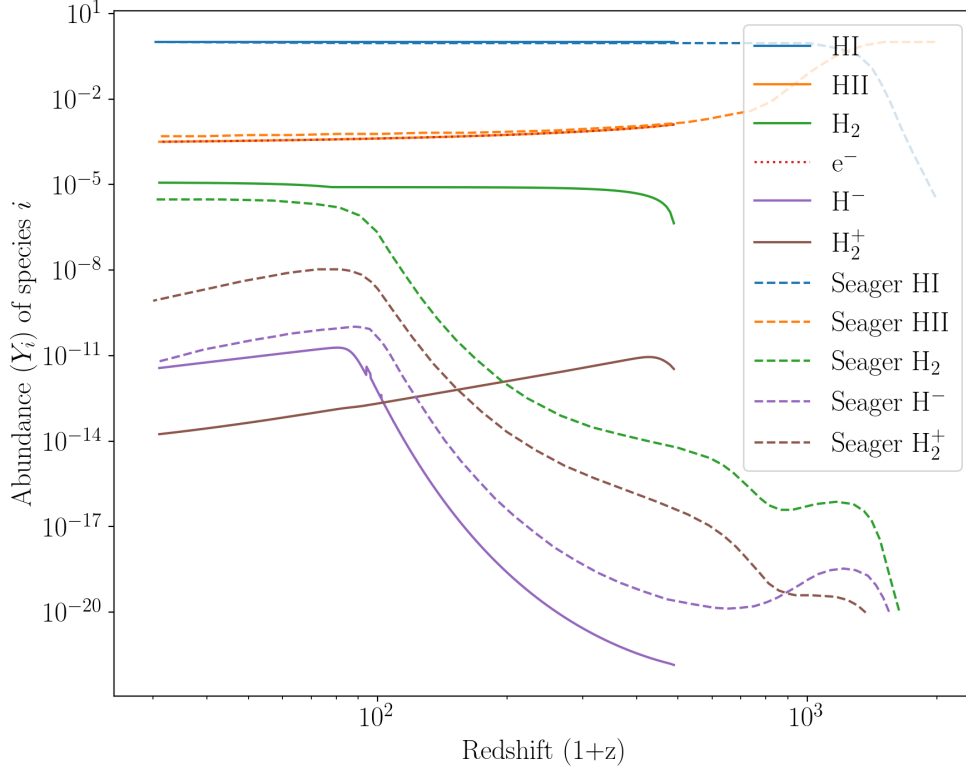
FIGURE 3.19: Same as Figure 3.17, with H^- photodetachment due to the CMB and H_2^+ photodissociation due to CMB photons. Although the H_2 fraction is lower than in Figure 3.17, the presence of H_2^+ at higher redshifts prevents us from obtaining a final H_2 fraction that agrees with Seager et al. (2000).

form H_2 via. H_2^+ is constant with temperature (reaction k_4 from Glover and Abel 2008), and since the H I fraction is also roughly constant in this regime, the only parameter manipulating how much H_2 will form is the fraction of H_2^+ itself. Therefore, simply fixing the H_2^+ fraction to follow the behaviour of Seager et al. (2000) will not fix this problem, as the gas-phase formation rate via H_2^+ will still be too large.

One solution is to disable H_2^+ for redshifts $z > 100$. This produces a final H_2 fraction that agrees with Seager et al. (2000), as shown in Figure 3.20. Our justification for this solution is that underestimating the H_2 fraction at $z > 100$ will not have much of an effect on our simulations; our chemistry network floors at $Y_i \sim 10^{-13}$, so we cannot even track the actual H_2 fraction above $z > 200$.

79
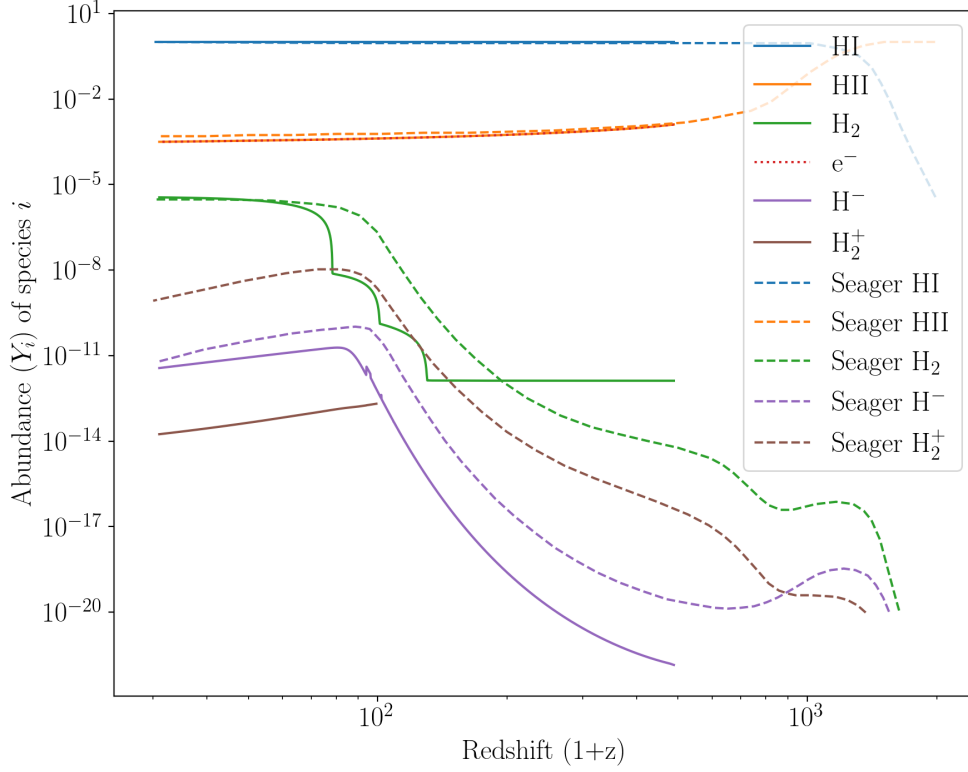
FIGURE 3.20: Same as Figure 3.19, with H_2^+ disabled for redshifts $z > 100$. This simulation under-produces H_2 at $80 < z < 200$, but obtains an H_2 fraction at $z = 30$ that agrees with the literature value. The curve for H_2 is flat between $150 < z < 500$ because the GASOLINE chemistry network floors abundances below the 10^{-13} level.

However, we can also compare our cosmo16 simulation to Galli and Palla (2013), shown in Figure 3.21. In this simulation, we once again disable H_2^+ for redshifts $z > 100$, but show the full curve of H_2^+ for comparison. In the Galli and Palla (2013) model, the H_2^+ fraction is consistently lower than the value we simulate with cosmo16, suggesting that we may only need to capture the photodissociation rate of H_2^+, rather than model some additional process to suppress the radiative association pathway at $z < 100$. This model also suggests some uncertainty in the evolution of these chemical species as a function of redshift, as our H^- and H_2^+ fractions now exceed the Galli and Palla (2013) values by a factor of 10. Therefore, we may still need to adjust the exact behaviour of H^- photodetachment in order to complete this model of early universe chemistry.
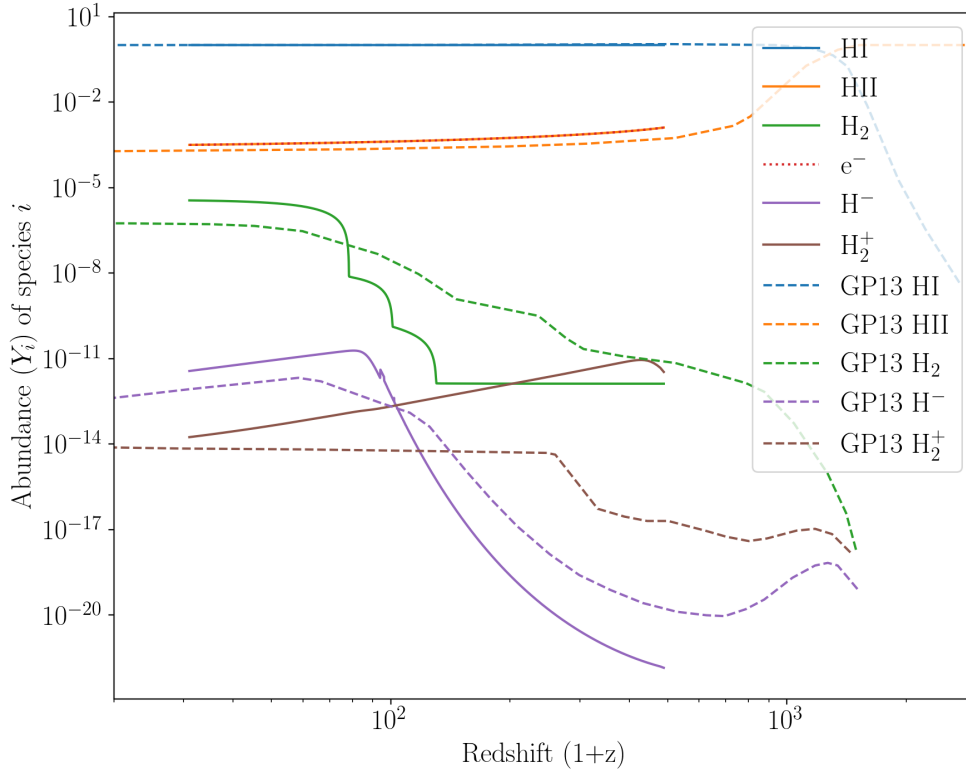
FIGURE 3.21: Same as Figure 3.20, but comparing to data from the review by Galli and Palla (2013). The H_2^+ fraction is displayed for comparison despite disabling H_2^+ for $z > 100$ in this simulation. Our final H_2, H^-, and H_2^+ fractions overestimate the Galli and Palla (2013) values. The H^- fraction is suppressed at $z < 100$ compared to Seager et al. (2000) and the cosmo16 simulation, which restricts the total amount of H_2 that can form. The H_2^+ abundance simulated in cosmo16 remains in excess of the Galli and Palla (2013) values throughout the entire simulation, suggesting that a correct H_2^+ fraction may be obtainable simply through correctly modeling the dissociation of H_2^+; no additional processes are required to reach an agreement.

Chapter 4

Summary and Future Work

4.1 Summary of Key Results

In this thesis, I have explored the physics of molecular hydrogen and how it interacts with radiation fields. The end result is a robust model, consistent with theoretical expectations and the behaviour of established work, including many with much more complex models. The model was implemented in the GASOLINE code so that it can now handle molecular hydrogen, complementing its upgraded radiative transfer capability. I also developed a one-dimensional code, RadT1d, to model H$_{II}$ regions and photodissociation regions. Development of this code required rethinking the treatment of Lyman-Werner radiation and implementing a new ionizing radiation band in order to make a self consistent coupling of radiation and chemistry that did not exist previously. This was tested against a PDR benchmark by Röllig et al. (2007), an H$_{II}$ region generated with CLOUDY (Ferland et al. 2017), a two-sided PDR model with the MEUDON code (Le Petit et al. 2006), and models of chemical evolution during the cosmic dark ages (Seager et al. 2000; Galli and Palla 2013). These tests have shown that my model for molecular hydrogen works correctly for conditions characteristic of the interstellar medium of galaxies in the nearby universe. Some additional work is required to couple the gas-phase formation pathways to the radiation field, namely capturing the photo-destruction processes for H$^-$ and H$_2^+$. This will enable my model of H$_2$ to be applied in all regions of the universe.

4.2 Future work

A natural target for this H$_2$ model is to study galaxies. The first goal we wish to pursue is to implement my molecular hydrogen model in a full galaxy simulation. We can explore how my implementation of H$_2$ improves the simulated ISM. The H$_2$ model also

provides a new capacity to compare observables, such as the Kennicutt-Schmidt relation and molecular cloud properties (Benincasa et al. 2020).

One specific behaviour we would like to examine is the threshold for the atomic to molecular transition in galaxies, which typically occurs at $\Sigma_{\rm H} \sim 10 M_\odot \; {\rm pc}^{-2}$. We should be able to reproduce this behaviour using Lyman-Werner radiation from the extragalactic background. This process can be investigated quickly with a relatively low computational overhead by performing post-processing radiative transfer on isolated disk galaxies. With a correct H_2 formation model, we may be able to reproduce the downwards trend in $\Sigma_{\rm HI}$ seen at smaller galactic radii as the gas transitions to being predominantly molecular (e.g. Figures 3 and 4 of Ostriker et al. 2010).

We would also like to explore the the connection between H_2 and star formation. An H_2-based star formation model that enforces a causal link between $\Sigma_{\rm H_2}$ and $\Sigma_{\rm SFR}$ may be incorrect. The relation is more likely correlation rather than causation, and chiefly applicable for late time, metal enriched galaxies (Krumholz et al. 2011; Krumholz 2012; Glover and Clark 2012; Glover 2023), but we can still use this H_2 model to investigate new sub-grid models for star formation. Our model is applicable over a wide range of circumstances, from present day star formation all the way to the formation of the first stars. We may therefore be able to investigate the formation of Population III stars. Pop III stars form in relatively small galaxies ($M \sim 10^8 M_\odot$), so it should be possible to simulate their formation with a high resolution volume (Greif et al. 2010).

Finally we plan to examine more complex chemistry models and their interaction with radiation (Grassi et al. 2014; Richings et al. 2014a). My experience coupling H_2 with radiation give us confidence that we can correctly couple our radiation method to these chemistry codes. Simulating a galaxy with these networks and radiation could provide us a baseline for what is possible with a full radiative transfer routine and a detailed chemistry model. The full range of applications will require metal cooling that can correctly adapt to varying radiation fields. One possibility that is currently being investigated is to use physically-informed neural networks that encode the relationship between the ionization state of metals and the input radiation field (Holdship et al. 2021; Branca and Pallottini 2023).

Bibliography

Abel, T., Anninos, P., Zhang, Y., and Norman, M. L. (Aug. 1997). Modeling primordial gas in numerical cosmology. *New Astronomy* 2(3), 181–207.

Ackermann, M. et al. (Feb. 2013). Detection of the Characteristic Pion-Decay Signature in Supernova Remnants. *Science* 339(6121), 807–811.

Allison, A. C. and Dalgarno, A. (Jan. 1969). Transition probabilities for the $B^1SIGMA_u^+$-$X^1SIGMA_g^+$ band system of H_2. *Journal of Quantitative Spectroscopy and Radiative Transfer* 9(11), 1543–1551.

Argyros, J. D. (Oct. 1974). Photodissociation of H_2^+: variation with temperature. *Journal of Physics B Atomic Molecular Physics* 7(15), 2025–2035.

Baczynski, C., Glover, S. C. O., and Klessen, R. S. (Nov. 2015). Fervent: chemistry-coupled, ionizing and non-ionizing radiative feedback in hydrodynamical simulations. *MNRAS* 454(1), 380–411.

Barnes, J. and Hut, P. (Dec. 1986). A hierarchical O(N log N) force-calculation algorithm. *Nature* 324(6096), 446–449.

Bates, D. R. and Herbst, E. (Jan. 1988). Radiative Association. In: *Rate Coefficients in Astrochemistry*. Ed. by T. J. Millar and D. A. Williams. Vol. 146. Astrophysics and Space Science Library, 17.

Baumschlager, B., Shen, S., and Wadsley, J. W. (Oct. 2023). Spectral reconstruction for radiation hydrodynamic simulations of galaxy evolution. *arXiv e-prints* arXiv:2310.16902, arXiv:2310.16902.

Benincasa, S. M., Wadsley, J., Couchman, H. M. P., and Keller, B. W. (Nov. 2016). The anatomy of a star-forming galaxy: pressure-driven regulation of star formation in simulated galaxies. *MNRAS* 462(3), 3053–3068.

Benincasa, S. M., Wadsley, J. W., Couchman, H. M. P., Pettitt, A. R., Keller, B. W., Woods, R. M., and Grond, J. J. (Dec. 2020). The anatomy of a star-forming galaxy II: FUV heating via dust. *MNRAS* 499(2), 2028–2041.

Benincasa, S. (Oct. 2014). On the Relationship Between Star Formation and the ISM. MA thesis. Hamilton, Ontario: McMaster University.

Bertschinger, E. (Jan. 1998). Simulations of Structure Formation in the Universe. *ARAA* 36, 599–654.

Bigiel, F., Leroy, A., Walter, F., Brinks, E., de Blok, W. J. G., Madore, B., and Thornley, M. D. (Dec. 2008). The Star Formation Law in Nearby Galaxies on Sub-Kpc Scales. *AJ* 136(6), 2846–2871.

Black, J. H. (Jan. 1987). Heating and Cooling of the Interstellar Gas. In: *Interstellar Processes.* Ed. by D. J. Hollenbach and J. Thronson Harley A. Vol. 134, 731.

Black, J. H. and van Dishoeck, E. F. (Nov. 1987). Fluorescent Excitation of Interstellar H 2. *ApJ* 322, 412.

Bovino, S. and Galli, D. (2019). Thermodynamics and chemistry of the early universe. In: *Formation of the First Black Holes.* Ed. by M. Latif and D. Schleicher, 45–66.

Branca, L. and Pallottini, A. (Jan. 2023). Neural networks: solving the chemistry of the interstellar medium. *MNRAS* 518(4), 5718–5733.

Bransden, B. H. (Sept. 1972). REVIEW ARTICLE: The theory of charge exchange. *Reports on Progress in Physics* 35(3), 949–1005.

Bryans, P., Badnell, N. R., Gorczyca, T. W., Laming, J. M., Mitthumsiri, W., and Savin, D. W. (Dec. 2006). Collisional Ionization Equilibrium for Optically Thin Plasmas. I. Updated Recombination Rate Coefficients for Bare through Sodium-like Ions. *ApJs* 167(2), 343–356.

Chabrier, G. (July 2003). Galactic Stellar and Substellar Initial Mass Function. *PASP* 115(809), 763–795.

Chevance, M., Krumholz, M. R., McLeod, A. F., Ostriker, E. C., Rosolowsky, E. W., and Sternberg, A. (July 2023). The Life and Times of Giant Molecular Clouds. In: *Protostars and Planets VII.* Ed. by S. Inutsuka, Y. Aikawa, T. Muto, K. Tomida, and M. Tamura. Vol. 534. Astronomical Society of the Pacific Conference Series, 1.

Christensen, C., Quinn, T., Governato, F., Stilp, A., Shen, S., and Wadsley, J. (Oct. 2012). Implementing molecular hydrogen in hydrodynamic simulations of galaxy formation. *MNRAS* 425(4), 3058–3076.

Coppola, C. M., Longo, S., Capitelli, M., Palla, F., and Galli, D. (Mar. 2011). Vibrational Level Population of H_2 and H_2^+ in the Early Universe. *ApJs* 193(1) 7, 7.

Di Matteo, T., Springel, V., and Hernquist, L. (Feb. 2005). Energy input from quasars regulates the growth and activity of black holes and their host galaxies. *Nature* 433(7026), 604–607.

Draine, B. T. (Apr. 1978). Photoelectric heating of interstellar gas. *ApJs* 36, 595–619.

Draine, B. T. and Bertoldi, F. (Sept. 1996). Structure of Stationary Photodissociation Fronts. *ApJ* 468, 269.

Dunn, G., Bellovary, J., Holley-Bockelmann, K., Christensen, C., and Quinn, T. (July 2018). Sowing Black Hole Seeds: Direct Collapse Black Hole Formation with Realistic Lyman-Werner Radiation in Cosmological Simulations. *ApJ* 861(1) 39, 39.

Dunn, G. H. (Aug. 1968). Photodissociation of H_2^+ and D_2^+: Theory. *Physical Review* 172(1), 1–7.

Eddington, A. S. (Apr. 1937). Interstellar matter. *The Observatory* 60, 99–103.

Faucher-Giguère, C.-A. (Apr. 2018). Recent progress in simulating galaxy formation from the largest to the smallest scales. *Nature Astronomy* 2, 368–373.

Federrath, C. (Dec. 2013). On the universality of supersonic turbulence. *MNRAS* 436(2), 1245–1257.

Federrath, C. and Klessen, R. S. (Dec. 2012). The Star Formation Rate of Turbulent Magnetized Clouds: Comparing Theory, Simulations, and Observations. *ApJ* 761(2) 156, 156.

Ferland, G. J., Chatzikos, M., Guzmán, F., Lykins, M. L., van Hoof, P. A. M., Williams, R. J. R., Abel, N. P., Badnell, N. R., Keenan, F. P., Porter, R. L., and Stancil, P. C. (Oct. 2017). The 2017 Release Cloudy. *RMxAA* 53, 385–438.

Field, G. B., Somerville, W. B., and Dressler, K. (Jan. 1966). Hydrogen Molecules in Astronomy. *ARAA* 4, 207.

Galli, D. and Palla, F. (Aug. 2013). The Dawn of Chemistry. *ARAA* 51(1), 163–206.

Glover, S. C., Savin, D. W., and Jappsen, A. .-. (Apr. 2006). Cosmological Implications of the Uncertainty in H^- Destruction Rate Coefficients. *ApJ* 640(2), 553–568.

Glover, S. C. O. (Feb. 2023). Molecular cloud formation in metal-poor gas. In: *Physics and Chemistry of Star Formation: The Dynamical ISM Across Time and Spatial Scales*, 242.

Glover, S. C. O. and Abel, T. (Aug. 2008). Uncertainties in H_2 and HD chemistry and cooling and their role in early structure formation. *MNRAS* 388(4), 1627–1651.

Glover, S. (Jan. 2013). The First Stars. In: *The First Galaxies*. Ed. by T. Wiklind, B. Mobasher, and V. Bromm. Vol. 396. Astrophysics and Space Science Library, 103.

Glover, S. C. O. and Clark, P. C. (Mar. 2012). Is molecular gas necessary for star formation? *MNRAS* 421(1), 9–19.

Glover, S. C. O. and Mac Low, M.-M. (Apr. 2007). Simulating the Formation of Molecular Clouds. I. Slow Formation by Gravitational Collapse from Static Initial Conditions. *ApJs* 169(2), 239–268.

Gnedin, N. Y. and Draine, B. T. (Nov. 2014). Line Overlap and Self-Shielding of Molecular Hydrogen in Galaxies. *ApJ* 795(1) 37, 37.

Gnedin, N. Y. and Hollon, N. (Oct. 2012). Cooling and Heating Functions of Photoionized Gas. *ApJs* 202(2) 13, 13.

Gnedin, N. Y. and Kravtsov, A. V. (Feb. 2011). Environmental Dependence of the Kennicutt-Schmidt Relation in Galaxies. *ApJ* 728(2) 88, 88.

Gnedin, N. Y., Tassis, K., and Kravtsov, A. V. (May 2009). Modeling Molecular Hydrogen and Star Formation in Cosmological Simulations. *ApJ* 697(1), 55–67.

Goicoechea, J. R. and Le Bourlot, J. (May 2007). The penetration of Far-UV radiation into molecular clouds. *AAP* 467(1), 1–14.

Grassi, T., Bovino, S., Schleicher, D. R. G., Prieto, J., Seifried, D., Simoncini, E., and Gianturco, F. A. (Apr. 2014). KROME - a package to embed chemistry in astrophysical simulations. *MNRAS* 439(3), 2386–2419.

Greif, T. H., Glover, S. C. O., Bromm, V., and Klessen, R. S. (June 2010). The First Galaxies: Chemical Enrichment, Mixing, and Star Formation. *ApJ* 716(1), 510–520.

Grond, J. J., Woods, R. M., Wadsley, J. W., and Couchman, H. M. P. (May 2019). TREVR: A general N $\log^2$N radiative transfer algorithm. *MNRAS* 485(3), 3681–3695.

Haardt, F. and Madau, P. (Apr. 1996). Radiative Transfer in a Clumpy Universe. II. The Ultraviolet Extragalactic Background. *ApJ* 461, 20.

Haardt, F. and Madau, P. (Feb. 2012). Radiative Transfer in a Clumpy Universe. IV. New Synthesis Models of the Cosmic UV/X-Ray Background. *ApJ* 746(2) 125, 125.

Habing, H. J. (Jan. 1968). The interstellar radiation density between 912 A and 2400 A. *Bulletin of the Astronomical Institutes of the Netherlands* 19, 421.

Hassan, S. Z., Tauch, J., Kas, M., Nötzold, M., Carrera, H. L., Endres, E. S., Wester, R., and Weidemüller, M. (Feb. 2022). Associative detachment in anion-atom reactions involving a dipole-bound electron. *Nature Communications* 13 818, 818.

Heays, A. N., Bosman, A. D., and van Dishoeck, E. F. (June 2017). Photodissociation and photoionisation of atoms and molecules of astrophysical interest. *AAP* 602 A105, A105.

Hirata, C. M. and Padmanabhan, N. (Nov. 2006). Cosmological production of H_2 before the formation of the first galaxies. *MNRAS* 372(3), 1175–1186.

Holdship, J., Viti, S., Haworth, T. J., and Ilee, J. D. (Sept. 2021). Chemulator: Fast, accurate thermochemistry for dynamical models through emulation. *AAP* 653 A76, A76.

Hollenbach, D. and McKee, C. F. (Nov. 1979). Molecule formation and infrared emission in fast interstellar shocks. I. Physical processes. *ApJs* 41, 555–592.

Hollenbach, D. J. and Tielens, A. G. G. M. (Jan. 1999). Photodissociation regions in the interstellar medium of galaxies. *Reviews of Modern Physics* 71(1), 173–230.

Hu, C.-Y., Naab, T., Glover, S. C. O., Walch, S., and Clark, P. C. (Oct. 2017). Variable interstellar radiation fields in simulated dwarf galaxies: supernovae versus photoelectric heating. *MNRAS* 471(2), 2151–2173.

Hu, C.-Y., Naab, T., Walch, S., Glover, S. C. O., and Clark, P. C. (June 2016). Star formation and molecular hydrogen in dwarf galaxies: a non-equilibrium view. *MNRAS* 458(4), 3528–3553.

Hu, C.-Y., Sternberg, A., and van Dishoeck, E. F. (Oct. 2021). Metallicity Dependence of the H/H_2 and $C^+/C/CO$ Distributions in a Resolved Self-regulating Interstellar Medium. *ApJ* 920(1) 44, 44.

Jeffreson, S. M. R., Krumholz, M. R., Fujimoto, Y., Armillotta, L., Keller, B. W., Chevance, M., and Kruijssen, J. M. D. (Aug. 2021). Momentum feedback from marginally resolved H II regions in isolated disc galaxies. *MNRAS* 505(3), 3470–3491.

Kannan, R., Marinacci, F., Vogelsberger, M., Sales, L. V., Torrey, P., Springel, V., and Hernquist, L. (Dec. 2020). Simulating the interstellar medium of galaxies with radiative transfer, non-equilibrium thermochemistry, and dust. *MNRAS* 499(4), 5732–5748.

Kennicutt Robert C., J. (Sept. 1989). The Star Formation Law in Galactic Disks. *ApJ* 344, 685.

Kennicutt, R. C. and Evans, N. J. (Sept. 2012). Star Formation in the Milky Way and Nearby Galaxies. *ARAA* 50, 531–608.

Kim, C.-G. and Ostriker, E. C. (Sept. 2017). Three-phase Interstellar Medium in Galaxies Resolving Evolution with Star Formation and Supernova Feedback (TIGRESS): Algorithms, Fiducial Model, and Convergence. *ApJ* 846(2) 133, 133.

Kim, J.-G., Gong, M., Kim, C.-G., and Ostriker, E. C. (Jan. 2023). Photochemistry and Heating/Cooling of the Multiphase Interstellar Medium with UV Radiative Transfer for Magnetohydrodynamic Simulations. *ApJs* 264(1) 10, 10.

Kim, J.-G., Kim, W.-T., and Ostriker, E. C. (Mar. 2016). Disruption of Molecular Clouds by Expansion of Dusty H II Regions. *ApJ* 819(2) 137, 137.

Klessen, R. S. and Glover, S. C. O. (Jan. 2016). Physical Processes in the Interstellar Medium. In: *Saas-Fee Advanced Course.* Ed. by Y. Revaz, P. Jablonka, R. Teyssier, and L. Mayer. Vol. 43. Saas-Fee Advanced Course, 85.

Klessen, R. S. and Glover, S. C. O. (Aug. 2023). The First Stars: Formation, Properties, and Impact. *ARAA* 61, 65–130.

Krumholz, M. R. (Nov. 2012). Star Formation in Atomic Gas. *ApJ* 759(1) 9, 9.

Krumholz, M. R., Klein, R. I., and McKee, C. F. (July 2012). Radiation-hydrodynamic Simulations of the Formation of Orion-like Star Clusters. II. The Initial Mass Function from Winds, Turbulence, and Radiation. *ApJ* 754(1) 71, 71.

Krumholz, M. R., Leroy, A. K., and McKee, C. F. (Apr. 2011). Which Phase of the Interstellar Medium Correlates with the Star Formation Rate? *ApJ* 731(1) 25, 25.

Larson, R. B. (Nov. 1974). Effects of supernovae on the early evolution of galaxies. *MNRAS* 169, 229–246.

Le Bourlot, J., Le Petit, F., Pinto, C., Roueff, E., and Roy, F. (May 2012). Surface chemistry in the interstellar medium. I. H_2 formation by Langmuir-Hinshelwood and Eley-Rideal mechanisms. *AAP* 541 A76, A76.

Le Petit, F., Nehmé, C., Le Bourlot, J., and Roueff, E. (June 2006). A Model for Atomic and Molecular Interstellar Gas: The Meudon PDR Code. *ApJs* 164(2), 506–529.

Liu, X. and Shemansky, D. E. (May 2012). Nondissociative electron and photon ionization cross sections of molecular hydrogen and deuterium. *Journal of Physics B Atomic Molecular Physics* 45(9) 095203, 095203.

Ménard, B., Scranton, R., Fukugita, M., and Richards, G. (June 2010). Measuring the galaxy-mass and galaxy-dust correlations through magnification and reddening. *MNRAS* 405(2), 1025–1039.

Naab, T. and Ostriker, J. P. (Aug. 2017). Theoretical Challenges in Galaxy Formation. *ARAA* 55(1), 59–109.

Nickerson, S., Teyssier, R., and Rosdahl, J. (Sept. 2018). A simple model for molecular hydrogen chemistry coupled to radiation hydrodynamics. *MNRAS* 479(3), 3206–3226.

Osterbrock, D. E. (1989). *Astrophysics of Gaseous Nebulae and Active Galactic Nuclei.* 20 Edgehill Road, Mill Valley, CA, 94941: University Science Books. ISBN: 0-935702-22-9.

Ostriker, E. C. and Kim, C.-G. (Sept. 2022). Pressure-regulated, Feedback-modulated Star Formation in Disk Galaxies. *ApJ* 936(2) 137, 137.

Ostriker, E. C., McKee, C. F., and Leroy, A. K. (Oct. 2010). Regulation of Star Formation Rates in Multiphase Galactic Disks: A Thermal/Dynamical Equilibrium Model. *ApJ* 721(2), 975–994.

Planck Collaboration et al. (Sept. 2016). Planck 2015 results. XIII. Cosmological parameters. *AAP* 594 A13, A13.

Richings, A. J., Schaye, J., and Oppenheimer, B. D. (June 2014a). Non-equilibrium chemistry and cooling in the diffuse interstellar medium - I. Optically thin regime. *MNRAS* 440(4), 3349–3369.

Richings, A. J., Schaye, J., and Oppenheimer, B. D. (Aug. 2014b). Non-equilibrium chemistry and cooling in the diffuse interstellar medium - II. Shielded gas. *MNRAS* 442(3), 2780–2796.

Richings, A. J., Faucher-Giguère, C.-A., Gurvich, A. B., Schaye, J., and Hayward, C. C. (Dec. 2022). The effects of local stellar radiation and dust depletion on non-equilibrium interstellar chemistry. *MNRAS* 517(2), 1557–1583.

Ricotti, M., Gnedin, N. Y., and Shull, J. M. (Aug. 2002). The Fate of the First Galaxies. I. Self-consistent Cosmological Simulations with Radiative Transfer. *ApJ* 575(1), 33–48.

Robinson, D., Avestruz, C., and Gnedin, N. Y. (Sept. 2022). Can Cooling and Heating Functions Be Modeled with Homogeneous Radiation Fields? *ApJ* 936(1) 50, 50.

Röllig, M., Abel, N. P., Bell, T., Bensch, F., Black, J., Ferland, G. J., Jonkheid, B., Kamp, I., Kaufman, M. J., Le Bourlot, J., Le Petit, F., Meijerink, R., Morata, O., Ossenkopf, V., Roueff, E., Shaw, G., Spaans, M., Sternberg, A., Stutzki, J., Thi, W. .-., van Dishoeck, E. F., van Hoof, P. A. M., Viti, S., and Wolfire, M. G. (May 2007). A photon dominated region code comparison study. *AAP* 467(1), 187–206.

Ryden, B. (2016). *Introduction to Cosmology.*

Schmidt, M. (Mar. 1959). The Rate of Star Formation. *ApJ* 129, 243.

Seager, S., Sasselov, D. D., and Scott, D. (June 2000). How Exactly Did the Universe Become Neutral? *ApJs* 128(2), 407–430.

Shapiro, P. R. and Kang, H. (July 1987). Hydrogen Molecules and the Radiative Cooling of Pregalactic Shocks. *ApJ* 318, 32.

Shaw, G., Ferland, G. J., Abel, N. P., Stancil, P. C., and van Hoof, P. A. M. (May 2005). Molecular Hydrogen in Star-forming Regions: Implementation of its Microphysics in CLOUDY. *ApJ* 624(2), 794–807.

Shen, S. (Jan. 2010). Enrichment of the intergalactic medium. PhD thesis. McMaster University, Canada.

Sillero, E., Tissera, P. B., Lambas, D. G., Bovino, S., Schleicher, D. R., Grassi, T., Bruzual, G., and Charlot, S. (June 2021). Modelling H_2 and its effects on star formation using a joint implementation of GADGET-3 and KROME. *MNRAS* 504(2), 2325–2345.

Smith, B. D., Bryan, G. L., Glover, S. C. O., Goldbaum, N. J., Turk, M. J., Regan, J., Wise, J. H., Schive, H.-Y., Abel, T., Emerick, A., O'Shea, B. W., Anninos, P.,

Hummels, C. B., and Khochfar, S. (Apr. 2017). GRACKLE: a chemistry and cooling library for astrophysics. *MNRAS* 466(2), 2217–2234.

Stancil, P. C. (July 1994). Continuous Absorption by He_2^+ and H_2^+ in Cool White Dwarfs. *ApJ* 430, 360.

Stecher, T. P. and Williams, D. A. (July 1967). Photodestruction of Hydrogen Molecules in H I Regions. *ApJL* 149, L29.

Sternberg, A. and Dalgarno, A. (Aug. 1995). Chemistry in Dense Photon-dominated Regions. *ApJs* 99, 565.

Sutherland, R. S. and Dopita, M. A. (Sept. 1993). Cooling Functions for Low-Density Astrophysical Plasmas. *ApJs* 88, 253.

Tielens, A. G. G. M. (2005). *The Physics and Chemistry of the Interstellar Medium.*

Tumlinson, J., Peeples, M. S., and Werk, J. K. (Aug. 2017). The Circumgalactic Medium. *ARAA* 55(1), 389–432.

Wadsley, J. W., Baumschlager, B., and Shen, S. (Oct. 2023). TREVR2: Illuminating fast $N \log_2 N$ radiative transfer. *arXiv e-prints* arXiv:2310.15235, arXiv:2310.15235.

Wadsley, J. W., Keller, B. W., and Quinn, T. R. (Oct. 2017). Gasoline2: a modern smoothed particle hydrodynamics code. *MNRAS* 471(2), 2357–2369.

Whitworth, D. J., Smith, R. J., Tress, R., Kay, S. T., Glover, S. C. O., Sormani, M. C., and Klessen, R. S. (Mar. 2022). Is the molecular KS relationship universal down to low metallicities? *MNRAS* 510(3), 4146–4165.

Wilson, T. L. and Rood, R. (Jan. 1994). Abundances in the Interstellar Medium. *ARAA* 32, 191–226.

Wolfire, M. G., Hollenbach, D., McKee, C. F., Tielens, A. G. G. M., and Bakes, E. L. O. (Apr. 1995). The Neutral Atomic Phases of the Interstellar Medium. *ApJ* 443, 152.

Wolfire, M. G., McKee, C. F., Hollenbach, D., and Tielens, A. G. G. M. (Apr. 2003). Neutral Atomic Phases of the Interstellar Medium in the Galaxy. *ApJ* 587(1), 278–311.

Wolfire, M. G., Tielens, A. G. G. M., Hollenbach, D., and Kaufman, M. J. (June 2008). Chemical Rates on Small Grains and PAHs: C^+ Recombination and H_2 Formation. *ApJ* 680(1), 384–397.